Dissertation

submitted to the
Combined Faculties for the Natural Sciences and for Mathematics
of the Ruperto-Carola University of Heidelberg, Germany
for the degree of
Doctor of Natural Sciences

Presented by
Dipl.-Phys. Marvin Weyland
born in
Magdeburg

Oral examination: 16.11.2016

Atomic excitation and molecular dissociation by low energy electron collisions

Referees: **Priv.-Doz. Dr. Alexander Dorn**
Prof. Dr. Andreas Wolf

Zusammenfassung

In dieser Arbeit wurden Impulsabbildungsverfahren genutzt um die elektronische Anregung metastabiler Zustände in Edelgasen sowie die dissoziative Elektronenanlagerung (DEA) in polyatomaren Molekülen zu untersuchen. Für die Beobachtung der Elektronenstoßanregung von Atomen wurde eine neuartige experimentelle Methode entwickelt, bei welcher die Streuwinkel der Elektronen nach dem inelastischen Stoß durch den Impulsübertrag auf das Atom gemessen werden. Impulsübertragsbilder für Helium und Neon wurden bei Elektronenenergien nahe der Anregungsschwelle aufgenommen und der Vergleich mit aktuellen theoretischen Rechnungen, welche auf der R-Matrix Methode beruhen, zeigt hervorragende Übereinstimmungen.

Für die Durchführung der DEA-Experimente wurde eine neue Apparatur zur Impulsmessung von negativen Ionen aufgebaut um biologisch relevante Moleküle zu untersuchen. In dieser Arbeit wurde DEA in den Molekülen Ammoniak, Wasser, Ameisensäure, Furan, Pyridin sowie in zwei Fluorchlorkohlenwasserstoffen untersucht. Weiterhin wurde die Änderung der DEA Resonanzenergien beim Übergang von einzelnen Molekülen zu Molekülclustern in Ammoniak und Ameisensäure untersucht. Die experimentellen Beobachtungen in den meisten Molekülen konnten mit aktuellen Rechnungen verglichen werden und unterstützen die Weiterentwicklung theoretischer Beschreibungen von DEA. Die neu gebaute Apparatur war in den durchgeführten Messungen in der Lage eine bessere Impulsauflösung zu liefern als vergleichbare existierende Geräte. Dies ermöglicht die impulsaufgelöste Untersuchung von schwereren Fragmenten sowie Fragmenten mit niedrigerer kinetischer Energie als bisher.

Abstract

In this work, momentum imaging experiments have been conducted for the electron impact excitation of metastable states in noble gases and for dissociative electron attachment (DEA) in polyatomic molecules. For the electron impact excitation study a new experimental technique has been developed which is able to measure the scattering angle distribution of the electrons by detection of the momentum transfer to the atoms. Momentum transfer images have been recorded for helium and neon at fixed electron impact energy close to the excitation threshold and good agreement with current R-matrix theory calculations was found.

A new momentum imaging apparatus for negative ions has been built for the purpose of studying DEA in biologically relevant molecules. During this work, DEA was investigated in the molecules ammonia, water, formic acid, furan, pyridine and in two chlorofluorocarbons. Furthermore, the change of DEA resonance energies when molecules form clusters compared to monomers was investigated in ammonia and formic acid. The experimental results of most studied molecules could be compared to recent theoretical calculations and they support further development in the theoretical description of DEA. The new apparatus built in this work also delivered a superior momentum resolution compared to existing setups. This allows the momentum imaging of heavier fragments and fragments with lower kinetic energy.

Contents

1. Introduction

The interaction of electrons with atoms and molecules is a subject which has driven scientific development for over a hundred years, starting with the ground breaking experiment by James Franck and Gustav Hertz in 1914 [40]. The ability of their experiment to measure atomic properties which had been predicted by theory led to a growth of the field of electron scattering. Since then, new processes were discovered, experiments and theories developed, and the field became more and more diverse. While in the beginning the investigations both in experiment and in theory were focused on electron impact ionization and excitation of simple atoms, over time targets became more complex, moving from light atoms to heavier atoms and to molecules. On the other hand, even nowadays, ionization and excitation of atoms is being investigated since new experiments are able to investigate more details of the processes, continuously driving development of new theoretical treatments of these reaction. While the very first experiments were only able to measure the total yield of different reaction products, newer methods are sensitive to the energy and scattering angles of all products [122]. This work will focus on two of those processes: electron impact excitation of atoms and dissociative electron attachment (DEA) of polyatomic molecules.

History of electron impact excitation

In general there are two ways to investigate electron impact excitation of atoms, either by detecting the electrons or by detecting the atoms. Both approaches have been used in experimental investigations in the past. The first experiment to measure electron impact excitation cross sections was performed in 1935 by Maier-Leibnitz [71]. By measuring the electron flux through a gas at variable electron energy he was able to identify the excitation of several states in noble gases. In 1957 Schulz and Fox performed the first experiment in which the atoms in metastable states were detected directly instead of the electrons [107] which led to an enormous improvement of the accuracy.

High precision measurements have been made possible with the next iteration of experiments which were performed by Brunt *et al.* [17, 19] in 1977. The energy spread of the projectile electron beam could be decreased to below 20 meV by using

a hemispherical electrostatic energy selector. With these experiments it was possible to obtain the total cross section for excitation of metastable states in noble gases with the highest energy resolution to date.

All the experiments mentioned so far were however only able to measure the total cross section of metastable production. To gain a more detailed insight into the scattering process, interest arose in studying the angular distributions of scattered electrons. Using energy and momentum conservation it is possible to obtain this information from either the momentum of the electron or the atom.

Measuring the small deflections of excited atoms in metastable states in a gas jet proved very challenging - especially for heavy targets [110]. Therefore, small movable electron detectors were a big step forward in electron atom collision experiments and enabled the investigation of angular distributions of the scattered electron. In most cases movable detectors therefore were used to detect the scattered electron instead of the target atoms. The setup is similar to the one of Brunt *et al.* in that an energy-selected electron beam intersects an atomic gas jet but in this case the electron detector consists of a hemispherical electrostatic energy analyzer as well and this detector moves around the interaction region. The electron energy analyzer which is combined with the detector allows the distinction of different excited states from knowledge of the energy of the scattered electron with high resolution. E.g. Hall *et al.* measured angular distributions of electronic excitation in helium using such a setup [49, 94]. However, the measurement of angular distributions is restricted to intermediate angles as the detector would interfere with the electron beam at angles close to 0° and 180°. This method is also time-consuming because only a small fraction of the scattered electrons - those with the correct scattering angle and the correct energy - can reach the detector. The restrictions of the limited angular range have been overcome by using a magnetic angle changer, i.e. a localized magnetic field in the interaction region which separates the trajectories of inelastically scattered electrons from the primary beam at all scattering angles from 0° to 180° [100, 28].

With the improvement of experimental methods to measure electron-atom interactions, theoretical descriptions of the processes were developed as well. For scattering at high electron energies, the Born approximation can be used to solve the scattering problem. The inelastic scattering of electrons however is efficient already at low impact energies where the Born approximation breaks down and the interaction of the projectile with different states of the atom has a high influence on the scattering cross section. Modern theories employ close-coupling calculations to take into account the coupling of the projectile to many electronic states of the target and are able to reproduce the scattering cross sections at low energies. R-matrix theory [8, 131] and convergent close-coupling [16, 41] are some of the methods which are currently used.

In the past, the development of new experiments allowed a more detailed view of the investigated process and led to a better understanding of it. The goal of the newly built setup in this work is to present an alternative experiment which is able to detect all events simultaneously, irrespective of energy loss and scattering angle. Thereby the efficiency of the detection can be increased, while still being able to measure angular distributions and distinguish different excited states. We achieve this by preparing a cold target gas jet and measuring the recoil momentum of the excited atom in a metastable state. Additionally, the use of a photo-cathode to

create the electron beam improves the projectile energy resolution.

History of dissociative electron attachment investigations

First observations of dissociative electron attachment began around 1930 as a side product of ionization threshold measurements. In these experiments, total ion yields at a variable electron energy were measured for positive as well as for negative ions. This was sufficient to observe the characteristic resonant structures in the negative ion formation as a function of impact energy. Measurements of the kinetic energy of the negative ions lead to the correct assumption that the investigated molecule must have dissociated [68, 113, 117, 118, 51].

The combination of negative ion current measurement with mass spectrometers allowed the identification of the negatively charged fragment and confirmed that molecules were dissociating in the interaction with low energy electrons. Until the end of the 1960s, formation of negative ions had been observed in many different molecules [24]. In 1970, the first experiments which could resolve the angular distribution of the fragments were conducted [123]. For many years angular distributions were measured using either a movable electron gun or a movable detector setup, similar to the experiments used for electron impact excitation. It took until 2005 for a new experimental design to qualitatively improve the measurement of angular distributions when the group of E. Krishnakumar adapted the velocity slice imaging technique for studying dissociative electron attachment [81]. This imaging technique allows the detection of ions of all scattering angles as well as their kinetic energies and has a higher efficiency than the previously used movable detector setups. Variations of this setup are now used in several institutes studying dissociative electron attachment around the world [2, 79, 130]. The dissociative electron attachment setup constructed during this work is a variation of this type of apparatus aimed at high mass resolution and a good angular resolution even for heavy or low energetic fragments.

Theoretical descriptions of dissociative electron attachment are in general more challenging than calculations of electron-atom scattering mentioned above because it is a resonant process. The interaction of the projectile with different states of the molecule is inherently relevant in this case. Additionally, the dependence of molecular orbital energies on the shape of the molecule needs to be known. A first theoretical treatment of the resonant electron capture and subsequent dissociation was given by O'Malley in 1966 [86]. The prediction of angular distributions of a fragment was restricted to basic symmetry considerations in this theory. Modern calculations use different methods. E.g., the R-matrix theory is used to describe electron scattering from complex molecules at low energies [119] and the complex Kohn variational method was recently used to calculate angular distributions of DEA fragments in small polyatomic molecules [53, 101].

The topic of dissociative electron attachment has gained a lot of attention in recent years. While this process has been observed as mentioned since the 1930s [51, 68, 113, 117, 118], one study in 2000 by the group of L. Sanche [13] sparked the interest of the scientific community. When investigating single-strand break (SSB) and double-strand break (DSB) in DNA by low energetic electrons, they observed a high destructive power of electrons below the ionization threshold (cf. figure 1.1(a)). They compared the energy dependence of their DNA damage measurements with

reactions taking place in prototype molecules like the DNA-base thymine and in water (cf. figure 1.1(b)). In the investigated molecules, they found H^- production which arises from dissociation of the molecules with a similar energy dependence as the single- and double-strand break yield in DNA. Their explanation for this observation was that dissociative electron attachment (DEA) must play a crucial role in the breaking of DNA strands. This discovery has huge implications for the understanding of radiation damage in DNA and biological matter in general. The reason is that a large number of slow secondary electrons within the energy range relevant to DEA are produced by energetic α-, β- or γ-rays penetrating biological tissue.

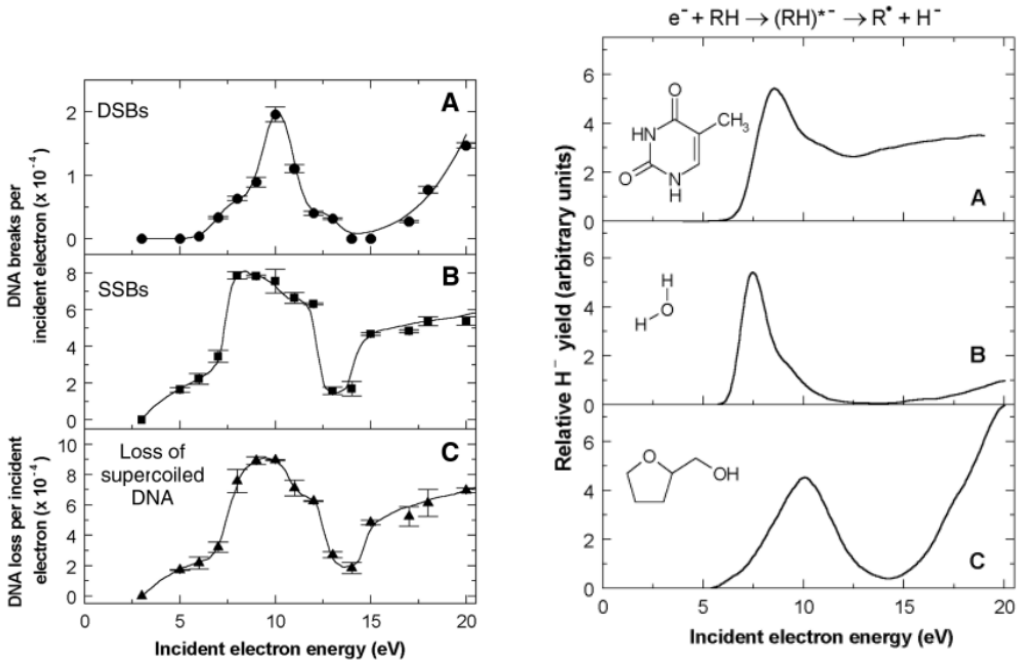

(a) (b)

Figure 1.1: Comparison of (a) DNA damage by irradiation with low energy electrons with (b) dissociation of prototype molecules which are similar to DNA constituents as well as water. The pictures were taken from [13].

To understand radiation damage induced by DEA in biological matter in detail, the focus of DEA investigations shifted from small basic molecules to larger molecules. These biologically relevant molecules are DNA-acids and sugars, but also prototypical heterocyclic organic compounds which form the basis of biological molecules, and many more. This shift in the focus of experimental investigations meant that dissociation of the molecules of interest is much more complicated to understand, e.g. they may exhibit many different DEA channels leading to different fragments. On the experimental side the development of efficient ion imaging techniques enabled more detailed and comprehensive studies of DEA by measuring angular distributions and kinetic energies of the produced fragments. The velocity slice imaging technique developed by Nandi *et al.* in 2005 reconstructs these properties by recording 2-dimensional momentum distributions of the ions [81]. As a next step the momentum imaging method developed by Adaniya *et al.* in 2012 provided 3-dimensional momentum distributions of the negative ions [2]. Although other important prop-

erties - like electronic, vibrational and rotational states of the fragments - are still hidden to current experiments, the advances in experimental design and also in theoretical studies since the beginning of the century have substantially increased our understanding of dissociative electron attachment.

The commonly used implementation of velocity slice imaging and momentum imaging experiments are however not optimized for investigation of the heavy fragments often found in biological molecules. Some optimizations, like the ones implemented and discussed in this work, can enable current experiments to improve their sensitivity in the required region of heavy and slow fragments. The investigation of single molecules can however only give a partial understanding of the processes in nature. Different, specialized experiments can be used to investigate DNA damage in a top-down approach by irradiating whole specially prepared DNA structures [85]. While those experiments represent the situation in nature quite well, the complexity of the structures makes an understanding on the physical level even more difficult. Following the bottom-up approach instead, investigations of molecules in different environments can give more insight into the influence of the environment. The most simple kind of change in environment is the transition from lone molecules to clusters, representing a precursor of a liquid. The influence of clustering on DEA is one of the topics investigated in this work and was studied in the molecules ammonia and formic acid. In addition, the present thesis aims to adopt existing imaging techniques to a well resolved detection of heavy and slow ions. Our experiments are performed in a momentum imaging apparatus built especially for this purpose. We obtain the high momentum resolution necessary to measure heavy and slow fragments by delivering the target at a very low temperature of only a few Kelvin using a supersonic gas jet. This is critical to obtain a high momentum resolution Our experiment is also designed to be able to retain a high mass resolution, allowing the observation of different dissociation channels with fragments of similar mass. Additionally, the use of a photoemission electron gun increases the impact energy resolution compared to similar existing setups.

Among other, we investigated DEA in biologically relevant molecules like water and the heterocyclic organic compound furan and pyridine - which serve as prototype molecules for DNA-bases and sugar - using this machine. The experiments performed on furan and pyridine were the first of momentum imaging experiments in these molecules, while in other molecules like water, ammonia and formic acid the experiments improved and expanded past observations. In all cases, the work presented in this thesis helps to further the understanding of DEA in biological matter.

2. Theory

In this chapter, basic physical processes like electronic transitions and dissociative electron attachment, which are important to this work, are reviewed. Afterward, the mathematical description of possible angular distributions of fragments measured in the DEA experiment is derived. In the end our own extension to this method, which incorporates changes in the molecular geometry before dissociation, is explained.

2.1 Electronic excitation and metastable states

Electronic excitation of atoms and molecules by electron impact is an important process which can be found in many different areas of daily life and scientific research. In natural phenomena such as aurora, electronic excitation of molecules plays an important role and it is important for many practical applications as well.

In a collision with the atomic or molecular target, the projectile electron can transfer energy to the target and excite a bound electron to a state of higher energy which was previously unoccupied. These unoccupied orbitals are also called virtual orbitals. In light atoms like the ones investigated in this work, the coupling of angular momentum L and spin S is weak and the total spin of the atom stays unchanged during a direct scattering process. One way in which the total spin of the atom can be changed is when the projectile electron is resonantly captured. This process involves an electronic excitation of the target as well. If the excitation energy of the target electron is the same as the energy difference between the projectile electron and a virtual orbital, the projectile can be quasi-bound in this orbital. In this process, a transient negative ion is formed, which is doubly excited. The energy of the doubly excited negative ion is above its ionization limit, i.e. it has enough energy for auto-detachment of one electron. The captured projectile electron or the excited target electron can relax to a lower state while ejecting the other electron from its bound state. In some cases the captured electron will relax first and a formerly bound target electron is ejected. In this electron exchange, the total spin of the atom can be changed: $\Delta s = -1, 0, +1$. That way, triplet states can be created from singlet states and vice versa.

Atoms in excited states can decay by emission of photons, following selection rules. Because a photon carries no spin and an angular momentum of $l = 1$, electrons can relax via a one photon decay only into states meeting the conditions $\Delta l = \pm 1, \Delta s = 0$. E.g., in a helium atom with the singlet ground state configuration $1^1\mathrm{S}$ ($1s^2$), an electron can be excited to the $2p$ shell without spin exchange, leaving the system in a $2^1\mathrm{P}$ ($1s2p$) configuration. The electron can decay back into the ground state, because it has the same spin and the angular momentum differs by $l = 1$. Therefore this state will decay very quickly by emission of one photon. These transitions are called electric dipole allowed transitions. Another photonic relaxation mechanism is two photon emission. If helium is excited into a $2^1\mathrm{S}$ ($1s2s$) configuration for example, it can decay into the ground state by emission of two photons, sharing the excitation energy. In this case, the two photons allow a transition without a change in the angular momentum quantum number. If the helium atom is excited to $2^3\mathrm{S}$ ($1s2s$) by electron exchange however, it cannot decay via a dipole transition because for its spin configuration ($\sum s = 1$) it is in the electronic ground state. It can only decay after electron exchange in a collision with another atom or after a spontaneous spin flip in the atom. Consequently the lifetimes of those different decay mechanisms vary by several orders of magnitude, from nanoseconds for states that decay via one photon dipole transitions over microseconds for states that decay via two photon emission and many minutes for the spin-forbidden transition from the $2^3\mathrm{S}$ state.

Many theoretical models were developed to describe electronic excitation processes in atoms as well as other electron-atom interactions like elastic scattering or electron impact ionization. The most accurate theories for electron-atom interactions at low electron energies take into account the coupling of the projectile to many target states. This coupling influences the process and nowadays close-coupling calculations are used to describe many states of the combined projectile-target system. There are several methods based on this kind of description of the system, results of which are used in this work and compared to our experimental observations. All of those methods solve the Schrödinger equation for the many-body system numerically but use different approaches. Some methods will shortly be named, if results of those calculations were used in this work. Detailed information about them can be found in the cited papers. The R-matrix method is a widely used approach to describe scattering of electrons and other projectiles at atoms and molecules. It treats the scattering process in two regions: a sphere of a certain radius in which the wave-functions for all particles of the target and the projectile are treated properly and exchange processes are taken into account, and the region outside of this sphere, in which only the projectile wave-function in the long range potential of the molecule is considered while exchange interactions are neglected. Results of two implementations of the R-matrix method are used in this work, namely the R-matrix with pseudo-states (RMPS) and the B-spline R-matrix (BSR) method. In both implementations, additional pseudo states above the ionization threshold are added to the target states to model ionization. Both implementations vary in the choice of the basis functions to represent the scattering problem [8, 9, 65, 119, 131]. The third method with which results of this work are compared is convergent close-coupling (CCC). In contrast to the R-matrix method, interactions are not separated into two different regions and the results of the scattering calculations are performed not with a fixed number of states but by adding states until the results converge, i.e. addition

of further states does essentially not change the results anymore [16, 41].

2.2 Molecular orbitals

When atoms form molecules, the atomic orbitals of all members of the molecule will combine and form molecular orbitals. In this section, a short introduction to different kinds of molecular orbitals will be given with a focus on the symmetry of the resulting molecular orbitals.

The most simple model to describe molecular orbitals is the linear combination of atomic orbitals (LCAO) as described by Lennard-Jones [67]. The molecular orbitals are described using the solution of the Schrödinger equation of the electrons in the potential of each of the nuclei separately, yielding wave-functions based on the known solutions for the atomic wave functions and developing the molecular orbital as an expansion of the atomic orbitals. This treatment neglects the electron-electron interaction and does not yield correct energies of the orbitals. Therefore the energies of the states must be adjusted approximately. This simple model does however give a useful shape of the resulting orbitals and the correct symmetries. In a very simple example, when calculating the lowest states of H_2 and only adding the 1s state wave-functions of the two hydrogen atoms $\Psi_{1s}(i)$ (where $i = 1, 2$ denotes atoms 1 or atom 2), there are two possible solutions, namely $\Psi_{\sigma_g} = 1/\sqrt{2}\,\Psi_{1s}(1) + 1/\sqrt{2}\,\Psi_{1s}(2)$ and $\Psi_{\sigma_u} = 1/\sqrt{2}\,\Psi_{1s}(1) - 1/\sqrt{2}\,\Psi_{1s}(2)$. The first combination gives the bonding orbital Ψ_{σ_g}, which has a *gerade* symmetry. In this case the wave-functions of the electrons in both atoms have the same sign which leads to a high probability of finding the electron in the region between the nuclei where the orbitals overlap. The second solution is the anti-bonding orbital Ψ_{σ_u}, which has a *ungerade* symmetry. Here, both electron wave-functions have opposite signs. This leads to the electrons being located mostly outside the nuclei and a nodal plane between the nuclei where the two wave-functions cancel out.

In this work it is not necessary to calculate the shapes and energies of orbitals. It is however necessary to know the symmetry of a molecule and the irreducible representations of the point group to which the molecule belongs. These irreducible representations describe all possible symmetries of the molecular orbitals in the molecule. We first use the Schönflies notation to describe the symmetry of a molecule. Here, ammonia will be used as an example since it is one of the investigated molecules. It belongs to the C_{3v} group, meaning that it has one rotation axis along which a 3-fold rotation leaves the molecule unchanged as well as 3 mirror planes which contain the rotation axis. Each of these symmetry operations can be expressed as a matrix operation, transforming the coordinates of the molecule. While the concrete form of those transformation matrices depends on the choice of the basis functions, the trace of a matrix is invariant under a change of the basis. This trace of the transformation matrix is called the character of the transformation [4]. Any molecular orbital in a given molecule possesses the same symmetry operations as one of the irreducible representations of the point group of the molecule. This means that the character of a symmetry operation in an irreducible representation gives information about the structure of the corresponding molecular orbital. For the 1-dimensional representations A_i and B_i ($i = 1, 2$) this character is either +1 or -1 and represents a change in the sign of the wave-function after the symmetry operation. In the 2-dimensional

Table 2.1: Character table for the C_{3v} point group and combinations of spherical harmonics with the same transformation properties as its irreducible representations, up to $l = 3$.

	E	$2C_3$	$3\sigma_v$	Basis functions
A_1	1	1	1	Y_l^0 or $Y_3^3 - Y_3^{-3}$
A_2	1	1	-1	$Y_3^3 + Y_3^{-3}$
E	2	-1	0	$(Y^-1_l, -Y_l^1)$; $\left(Y_l^2, Y_l^{-2}\right)$

representation E, other characters (0, 2) are possible. The full character table of the C_{3v} symmetry is shown in table 2.1. As an example, in the case of a C_{3v} symmetry of a molecule this means that a_2 orbitals[1], which have a character of -1 for the reflection operation σ_v, change the sign of their wave-function in the reflection. Therefore, they must have a node along all mirror planes. Their character for the 3-fold rotation C_3 is +1. Thus, the wave function stays unchanged after the rotation. The resulting probability density distributions of electrons in those orbitals consists of six separated volumes and those orbitals will be anti-bonding. Orbitals which have an A_1 or E symmetry on the other hand can be bonding.

The angular part of the wave-function for any molecular orbital can be described by an expansion into a series of linear combinations of spherical harmonics. The symmetry of the orbital restricts the choice of spherical harmonics because they are required to obey the same transformation properties under all the symmetry operations as the corresponding orbital. An example for the different possible orbital symmetries, their symmetry operations and the corresponding combinations of spherical harmonics which form a basis for each orbital are shown for the C_{3v} molecular symmetry in table 2.1. This very general description does not depend on any properties of the molecule except its symmetry, i.e. the angular part of molecular orbitals of any molecule possessing this symmetry can be described in the basis of those combinations of spherical harmonics.

2.3 Fundamentals of DEA

Dissociative electron attachment is a resonant process which occurs in several successive steps. In the first step an electron with an energy of typically less than 10 eV collides with a molecule and is resonantly captured into a virtual orbital of the molecule. This can happen in several different forms of resonances, namely shape resonances and Feshbach resonances [25].

In a shape resonance the electron is temporarily trapped by the potential of the molecule. A combination of an attractive part due to polarization of the molecule and a repulsive part due to the angular momentum of the trapped electron in the frame of the molecule create a barrier, which the electron has to overcome to leave the molecule. The potential energy surface, that is the energy of an electronic state as a function of the geometry of the molecule, of a shape resonance lies above the energy of the ground state. This allows auto-detachment and yields short lifetimes in the order of 10^{-15} s to 10^{-10} s. If the electron undergoes auto-detachment, it will

[1] Molecular orbitals are named after their irreducible representations except that they are labeled using lowercase letters.

leave the molecule in its ground state. In the core-excited shape resonance, the situation is very similar to the former case, except that the incident electron has a higher energy which allows inelastic scattering first and leaves the molecule in an electronically excited state. The electron is then trapped in the potential of the electronically excited molecule. While a shape resonance usually occurs at projectile electron energies between 0 eV and 4 eV, the core excited shape resonance can occur at higher energies around 10 eV.

Alternatively, electrons can be captured in Feshbach resonances. There are two different kinds of Feshbach resonances we consider in the context of electron attachment to molecules. In a nuclear-excited Feshbach resonance, the kinetic energy of the incoming electron is coupled to molecular vibration in the target. The potential energy surface of the created negative ion resonance state is below the ground state potential energy surface of the neutral. This stabilizes the negative ion, but the ion is created in a higher vibrational state than the parent molecule. Due to this stabilization the created negative ion has a longer lifetime than a shape resonance, around 10^{-6} s. This resonance occurs at very low electron energies around 25 meV or even lower. Like in the shape resonances, a Feshbach resonance also can take place in an electronically excited molecule, which gives the second kind, the so-called electron-excited Feshbach resonance. The incoming electron loses the main part of its energy in the electronic excitation and is captured in the field of the excited target molecule. In this resonance, the remaining kinetic energy of the electron is still coupled to molecular vibration but in this case the vibrational levels of the excited state of the negative ion can lie energetically below the vibrational ground state of the molecule in the electronically excited state. If this is the case, the state is further stabilized, leading to even longer lifetimes.

The negative ion is created in a non-equilibrium geometry because equilibrium bond lengths and bond angles in the negative ion differ from the ones in the neutral molecule. Therefore, the shape of the ion will develop in time. Electrons will tend to relax into lower electronic states which can lead to auto-detachment of the captured electron, leaving the molecule intact. If auto-detachment does not happen or takes too long, relaxation of the molecular configuration towards the new equilibrium geometry becomes important. This can mean a change in the form of the molecule towards new bond angles and bond lengths in the form of vibrational motion of the molecule. The electron attachment usually leaves the molecule in an unstable state as the bond between different atoms of the molecule is weakened. Breaking of one or more bonds in the molecule may be the energetically favorable option, leading to the dissociation of the molecule into two or more fragments, one of them being negatively charged.

An illustration of the involved energies is given in figure 2.1, which shows the binding energy with varying bond length for the parent molecule AB as well as the negative ion AB^-. While this is a very rough sketch that only considers atomic motion along the bond axis between part A and part B as it is the case for diatomic molecules, it illustrates the process easily. The energy curve for the parent molecule AB has a minimum at the equilibrium bond length of the parent molecule and the energy for the negative ion AB^- decreases with increasing bond length which will lead to the two parts of the molecule moving apart to lower their energy. As long as the bond length is smaller than the critical length r_c, the bond energy of the negative ion

is higher than that of the neutral molecule at the same geometry. Therefore, auto-detachment of the electron is possible until the dissociation process has increased the bond length beyond this critical value. Since electronic processes are much faster than nuclear motion, the position of the nuclei during an electronic transition is essentially constant. They are represented by a vertical arrow in figure 2.1. This kind of transition is also called a Franck-Condon transition. Even in the vibrational ground state of the molecule, the bond length varies within a certain range. This allows transitions at different bond lengths, which requires different impact energies, as shown by the dashed gray arrows in the figure.

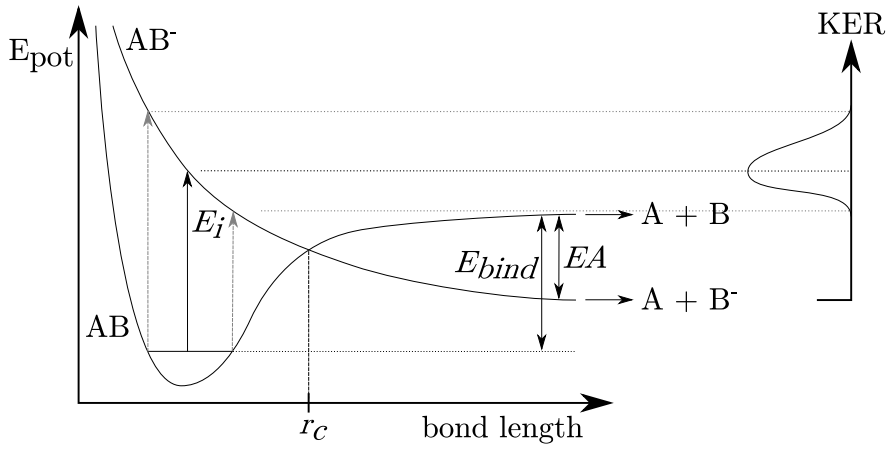

Figure 2.1: Scheme of DEA in a diatomic molecule AB. E_i - incident electron energy, E_{bind} - energy needed to dissociate the bond, EA - electron affinity of fragment B, KER - kinetic energy release

This simple picture shows some important properties of DEA. DEA always has to compete against auto-detachment and the ratio between the two processes depends on the time it takes until the bond length reaches the critical value r_c. This favors the faster loss of light fragments, first of all hydrogen. In many molecules the hydrogen loss, creating either a hydrogen anion H^- or the negatively charged parent ion after losing a neutral hydrogen $(M - H)^-$ therefore is an important and prominent dissociation channel. The competition against auto-detachment also leads to an isotope effect. When replacing e.g. a hydrogen atom in a molecule by a deuterium atom, the DEA cross section can change drastically, usually lowering the cross section for the heavier species.

The complete energy balance of DEA in diatomic molecules is

$$E_i = E_{bind} - EA + KER\,, \tag{2.1}$$

while in polyatomic molecules it is

$$E_i = E_{bind} - EA + KER + E_{int}\,. \tag{2.2}$$

E_i is the energy of the incident electron, E_{bind} is the binding energy of the neutral molecule or - in polyatomic molecules - of the bond which is broken. EA is the electron affinity of the fragment that retains the electron after the reaction and KER is the kinetic energy release, i.e. the sum of the kinetic energies of all fragments. In the polyatomic case, the additional term E_{int} contains the energy that is stored in

internal degrees of freedom of the fragments in the form of rotational and vibrational excitation. Those formulas are applicable to a 2-body-dissociation in which only one bond is broken. In the case of 3-body-dissociation or when a ring structure is broken, E_{bind} is the sum of the binding energies of all bonds which were broken.

2.4 Angular distributions

In addition to the kinetic energy release, the angular distributions of fragments which are produced in DEA give more insight into the reaction. In the experiments performed in this work, the target molecules are always delivered in a gas jet and have no preferred orientation. Any anisotropy in the fragment distributions can therefore be ascribed to a dependence of the electron attachment on the orientation of the molecule. This is also called the electron entrance amplitude.

Anisotropic angular distributions have been predicted by Dunn as early as 1962 [34] and first calculations of the expected distributions have been performed by O'Malley and Taylor in 1968 [87]. The underlying idea for understanding the angular distributions of dissociation fragments is that the symmetry of the electronic wave function of the electron-molecule system has to be preserved after the reaction. Following the argumentation of Dunn we first consider DEA in a homo-nuclear diatomic molecule and represent the incoming electron as a plane wave $e^{i\mathbf{k}\cdot\mathbf{r}}$. The electron wave-function is symmetric with respect to rotations around the wave vector of the electron beam $\mathbf{k}$. When the internuclear axis of the target is aligned parallel to $\mathbf{k}$, then the electronic wave-function symmetry of the whole system depends on the symmetry of the occupied molecular orbitals. The symmetry must be conserved in the collision, i.e. the electronic configuration of the negative ion after electron attachment must have the same symmetry as the combined system of parent molecule and incoming electron. E.g. the rotational symmetry around the internuclear axis has to be preserved, and only capture into a σ-orbital is allowed.

If the internuclear axis is perpendicular to $\mathbf{k}$, then the possible symmetry operations of the system are reflection in a plane containing $\mathbf{k}$ and the internuclear axis, reflection through a plane normal to the internuclear axis, and rotation of 180° about $\mathbf{k}$. These symmetry operations also allow the capture into a π-orbital. In the case when the molecular axis is oriented perpendicular to the incoming electron beam, the symmetry is lower for hetero-nuclear diatomic molecules than it is for homo-nuclear diatomic molecules. For the former, the only possible symmetry operation is reflection through a plane containing $\mathbf{k}$ and the internuclear axis.

In the case of parallel alignment of $\mathbf{k}$ and internuclear axis, the main restriction in accessible states for the transient negative ion comes from the fact that it has to have the same symmetry as the molecular state of the parent molecule. Therefore the projection of the orbital angular momentum along the internuclear axis must stay constant and the reflection symmetry along a plane containing the internuclear axis must be preserved, e.g. a $\Sigma_g^+ \rightarrow \Sigma_u^+$ transition would be allowed while transitions from any Σ state to any Π state are forbidden.

For perpendicular alignment of internuclear axis and incoming electron wave vector there are other restrictions on the symmetry that allow more transitions like e.g. $\Sigma_g^+ \rightarrow \Pi_u$. A complete table of possible transitions for diatomic homo-nuclear and hetero-nuclear molecules is given by Dunn [34].

A more detailed investigation of the angular distributions of negative ions undergoing DEA has been carried out by O'Malley and Taylor in 1968 [87] and their calculations remain an important tool for the interpretation of these distributions until today. They separate the problem for the potential scattering wave-function into an electronic part and a nuclear part, assuming that the nuclear part is exactly that of the target molecule. This assumption means that the formulas obtained below are only valid if the molecule does not undergo any change in its geometry before it dissociates. Furthermore assuming that the dissociation happens much faster than the rotation of the molecule, they arrive at the following formula:

$$\sigma(\Omega) = \frac{4\pi^3}{k^2} e^{\rho_{J_r}} \sum_{\Lambda_r} \left| \sum_{L=|\mu|}^{\infty} \left\langle \chi_{J_r} V_{L|\mu|} \chi_v \right\rangle Y^*_{L\mu}(\Omega) \right|^2 \tag{2.3}$$

where k is the wave vector of the incoming electron, $e^{\rho_{J_r}}$ is the survival probability of the negative ion resonance state, μ is the change in axial angular momentum $\Lambda_r - \Lambda_T$ from the target state Λ_T before the electron attachment to the resonance state Λ_r after the electron attachment and $Y_{L\mu}(\Omega)$ are spherical harmonics, representing the partial wave expansion of the incoming plane wave. Furthermore, $V_{L|\mu|}$ is an electronic matrix element, χ_{J_r} is a vibrational wave-function of the average rotational state J_r in the negative ion resonance state and χ_v is the vibrational wave function of the target state.

For our purposes we can replace $\left\langle \chi_{J_r} V_{L|\mu|} \chi_v \right\rangle$ with $i^L e^{i\delta_L} a_{L|\mu|}$ with the potential scattering phase shift δ_L and the real coefficient $a_{L|\mu|}$ [5]. Furthermore we will assume that only one resonant state participates in the DEA process at a time which means that Λ_r is fixed and the respective sum vanishes. The equation then reads

$$\sigma(\theta, \varphi) \propto \left| \sum_{L=|\mu|}^{L_{max}} i^L e^{i\delta_L} a_{L|\mu|} Y^*_{L\mu}(\theta, \varphi) \right|^2 \tag{2.4}$$

where the particular summation indices depend on the symmetry of the system, since only partial waves with the correct symmetry are allowed to contribute to the capture in a specific orbital. E.g., in homo-nuclear diatomic molecules equation (2.4) can be further restricted to only even or odd values of L, depending on the parity of the final state. L_{max} is the maximum value of change in the angular momentum during the electron attachment. While this value theoretically is infinity, a small value can be chosen instead because the transfer of angular momentum in low energy collisions is usually low so that the influence of high L can be neglected. In the analysis of experimental angular distributions only angular momenta of $L \leq 3$ are used. Furthermore, the assumption that only one resonance will create an investigated angular distribution can be experimentally justified. Resonances can be investigated separately when dissociation fragments are observed differentially not only in angle but also in impact energy and kinetic energy release. In our experiments, different resonance states can almost always be distinguished by those properties.

The above equations are only applicable for diatomic molecules. However, it was shown by Azria *et al.* that under certain conditions they can be adapted to be used

for polyatomic molecules [5]. To meet the symmetry requirements in polyatomic molecules, the plane wave of the incoming electron is not simply obtained by an expansion of spherical harmonics but it must form a basis for the irreducible representations of the point group of the molecule and is therefore represented by linear combinations of spherical harmonics which form this basis. An example for the spherical harmonics forming a basis of different irreducible representations in the C_{3v} symmetry were already shown in table 2.1. Azria *et al.* denote those functions Φ^{ϵ}_{lm} with $m > 0$ and $\epsilon = \pm 1$ and chose the functions to be real. This yields

$$\frac{d\sigma}{d\Omega}(\hat{k}_i) \propto \left| \sum_{l,m,\epsilon} i^l e^{i\delta_l} a^{\epsilon}_{lm} \Phi^{\epsilon *}_{l,m}(\hat{k}_i) \right|^2 \tag{2.5}$$

for the orientation dependence of the cross section in the molecular frame. For polyatomic molecules however, the dissociation will in general not take place along the axis of of rotational symmetry as it is the case in diatomic molecules. The functions $\Phi^{\epsilon}_{lm}(\hat{k}_i)$ are therefore transformed from the molecular frame to the functions $X^{\epsilon}_{lm}(\theta, \varphi)$ in the laboratory frame which yields

$$\sigma(\theta, \varphi) \propto \left| \sum_{l,m,\epsilon=\pm 1} i^l e^{i\delta_l} a^{\epsilon}_{l,m} X^{\epsilon *}_{l,m}(\theta, \varphi) \right|^2 \tag{2.6}$$

where the summation limits of l, m depend on the symmetry of the system, as does $X^{\epsilon *}_{lm}(\theta, \varphi)$.

Angular distributions of the unknown $X^{\epsilon *}_{lm}(\theta, \varphi)$ functions are described by the transition probability from the initial to the final state in the electron attachment: $\langle final\ state | partial\ wave | initial\ state \rangle$. The *final state* is represented by the basis function corresponding to the symmetry of the resonant state. They must be rotated by the Euler angle $(0, \beta, 0)$ where β is the angle between the axis of dissociation and the symmetry axis to relate the experimentally measured angle to an orientation of the molecular frame. The *partial wave* and the *initial state* on the other hand are transformed from the molecular frame into the lab frame by rotating them along the Euler angle $(\varphi, \theta, 0)$. Both rotations are performed by applying the Wigner rotation matrix $\mathbf{D}^l(\alpha, \beta, \gamma)$:

$$\begin{aligned} D^l(\alpha, \beta, \gamma)_{m',m} = & \sum_x (-1)^x \frac{\sqrt{(l+m)!(l-m)!(l+m')!(l-m')!}}{(l-m'-x)!(l+m-x)!x!(x+m'-m)!} \\ & \cdot e^{im'\alpha} \cos^{2l+m-m'-2x}\left(\frac{\beta}{2}\right) \cdot \sin^{2x+m'-m}\left(\frac{\beta}{2}\right) \cdot e^{im\gamma} \end{aligned} \tag{2.7}$$

to the spherical harmonics in the molecular frame [31, 128]. For the complete distribution, the states are created from contributions of all partial waves. In the analysis, only waves up to $l = 3$ (i.e. s-, p-, d- and f-waves) are considered.

When the target is e.g. water, the symmetry of the target is C_{2v} with the irreducible representations A_1, A_2, B_1 and B_2. All states of the molecule (as well as all molecular orbitals) must belong to one of these representations and follow their transformation rules that are shown in table 2.2.

Table 2.2: Transformations of the irreducible representations of the C_{2v} symmetry

	E	C_2	σ_v	$\sigma_v^{'}$	Basis functions
A_1	1	1	1	1	Y_l^0 or $Y_l^m + Y_l^{-m}$; m even
A_2	1	1	-1	-1	$Y_l^m - Y_l^{-m}$; m even
B_1	1	-1	-1	1	$Y_l^m + Y_l^{-m}$; m odd
B_2	1	-1	1	-1	$Y_l^m - Y_l^{-m}$; m odd

As an example, the calculation of the angular distribution arising from a p-wave (Y_1^0) capture for a transition from an A_1 ground state (Y_0^0) to an B_2 state ($Y_1^1 - Y_1^{-1}$) in a molecule of symmetry C_{2v} will be shown. Since the ground state is represented by an isotropic Y_0^0 harmonic, it has no influence on the distributions and will be neglected in the following calculation. The resulting amplitude is

$$\begin{aligned} f(\varphi,\theta) &\propto \left\langle \mathbf{D}^1(0,\beta,0)\left[Y_1^1 - Y_1^{-1}\right] | \mathbf{D}^1(\varphi,\theta,0)\, Y_1^0 \right\rangle \\ &\propto -\sqrt{2}\cos\beta\sin\theta\cos\varphi - \sqrt{2}\sin\beta\cos\theta\,. \end{aligned} \tag{2.8}$$

In the experiment, the molecules are randomly aligned. This means that there is no preferred direction in the plane normal to the electron impact direction. The distribution in the lab frame can therefore be calculated from the amplitude by integrating the square of its modulus over the angle φ:

$$\begin{aligned} I_{l=1}(\theta) &= \int_0^{2\pi} |f(\varphi,\theta)|^2 \mathrm{d}\varphi \\ &= \frac{\pi}{2}\left(\cos(2\theta) + 3 - \cos(2\beta)\left(3\cos(2\theta)+1\right)\right)\,. \end{aligned} \tag{2.9}$$

The whole distribution is obtained by using the sum of all allowed partial waves as the amplitude function and multiplying each partial wave with their phase shift δ and their contribution strength a before calculating the intensity. When comparing the parameters a and δ to those in equation (2.6), the number of independent parameters is lowered due to the restrictions on the spherical harmonics contributions set by the symmetry. For the example of an A_1 to B_2 transition, the restrictions are $a_{l,m} = -a_{l,-m}$ and $|a_{l,m}| = const\ \forall\ m$. In practical applications, we restrict the distribution to contributions from s-, p-, d- and f-waves since attachment with a high change in angular momentum is unlikely. This yields the complete amplitude

$$f(\varphi,\theta) = a_s f_s(\varphi,\theta) + a_p\, e^{i\delta_p} f_p(\varphi,\theta) + a_d\, e^{i\delta_d} f_d(\varphi,\theta) + a_f\, e^{i\delta_f} f_f(\varphi,\theta) \tag{2.10}$$

where every function $f_i(\varphi,\theta)$ (for $i = s,p,d,f$) represents a partial wave contribution that depends on the symmetry group and the irreducible representation of the target state. The introduction of the phase shifts describes interference of the different partial waves.

2.5 Corrections to the angular distributions

A limiting factor in the application of the partial wave expansion is the requirement that the molecular shape and orientation must stay unchanged between electron attachment and dissociation. In polyatomic molecules however it is very unlikely to find a negative ion with the same equilibrium geometry as the neutral molecule. As a result, the prerequisite - namely that the dissociation must happen fast compared to the rotational period of the molecule - is replaced by a more restrictive one. When the equilibrium geometry changes, dissociation must instead happen fast compared to the molecular rearrangement. To circumvent this restriction, we take into account the change in the angular distribution due to a change in the geometry in our partial wave analysis of the ammonia molecule.

In ammonia, the equilibrium angle β_i between the dissociating NH-bond and the symmetry axis of the molecule is 68°. A current *ab initio* theoretical study indicated that in the anion this angle changes by about 25° towards higher angles before dissociation takes place [101]. This however has no influence on the electron attachment, which is the first step of the reaction. Therefore, we perform the partial wave expansion in two steps. In the first step we calculate the angular distribution $I(\theta_i)$ of the fragment assuming the molecular equilibrium geometry. In the second step, the yield at every single angle θ_i is assigned to a distribution of measured angles θ_f due to the change of the molecular geometry. This step can be separated from the actual partial wave calculations and a table for reassigning the angular distributions provides the necessary data.

To illustrate how the angular distribution map is created, the angles shown in figure 2.2 are used. The angle θ at which the dissociation product is found is calculated for every orientation ψ (from 0° to 180°) of the molecular symmetry axis with respect to the electron impact direction and every rotation ϕ (from 0° to 360°) of the molecule around the symmetry axis. The rotation around the electron impact direction does not need to be taken into account except as a solid angle correction because the whole problem is rotational symmetric around this axis. For every combination of ψ and ϕ the resulting fragment angles θ_i and θ_f are calculated for two bond angles: the initial equilibrium bond angle β_i and the new final bond angle β_f, respectively.

$$\theta_{i,f}(\psi, \phi; \beta_{i,f}) = \arccos\left(\cos(\psi)\cos(\beta_{i,f}) + \sin(\psi)\sin(\beta_{i,f})\sin(\phi)\right) \tag{2.11}$$

Each obtained combination (θ_i, θ_f) is added to an angular reassignment map as shown exemplary in figure 2.3 for $\beta_f - \beta_i = 25°$. For every fragment angle θ_i - assuming the bond angle β_i during attachment - the resulting map contains a distribution of angles θ_f for the new bond angle β_f during dissociation. The reason is that each particular angle θ_i can result from a range of combinations (ψ, ϕ), which in turn leads to a range of angles θ_f. The solid angle correction for the ignored rotation of the molecular symmetry axis around the electron impact direction is performed for every pair (θ_i, θ_f) when it is added to the table. Every calculated event is weighted according to the angle of the molecular axis by $\sin\psi$. The correction must be done at this point because a combination (θ_i, θ_f) has a certain weighting factor when created from a particular angle ψ. The redistribution map is independent of the

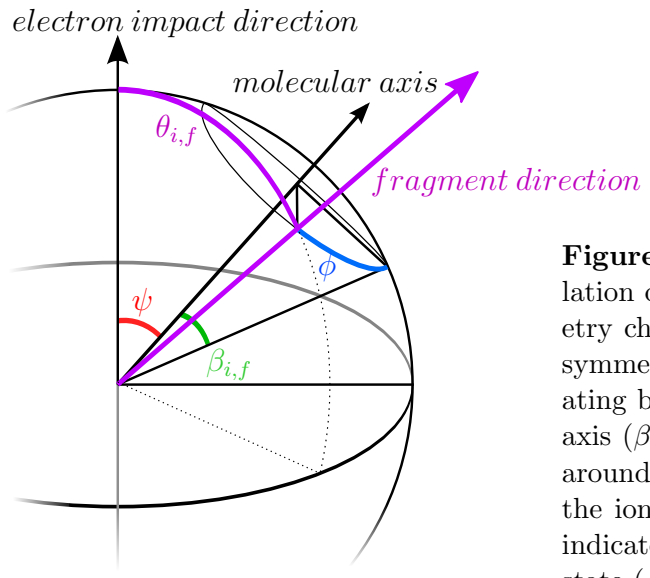

Figure 2.2: Relevant angles for the calculation of the influence of molecular geometry change: orientation of the molecular symmetry axis (ψ), angle of the dissociating bond with respect to the symmetry axis ($\beta_{i,f}$), rotation angle of the molecule around its symmetry axis (ϕ) and angle of the ionic fragment ($\theta_{i,f}$). The subscripts indicate the initial shape (i) and the final state (f).

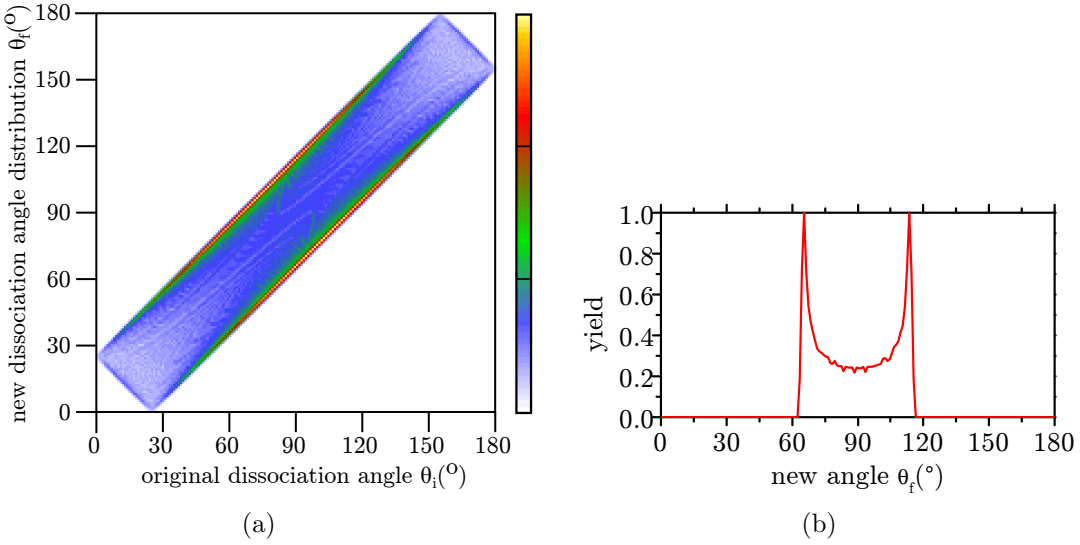

Figure 2.3: (a) Angular reassignment map for a bond angle change of 25° and (b) the resulting distribution for events which were formerly found at θ_i=90°.

original bond angle β_i and of the direction of change. Instead it is solely determined by the amplitude $|\beta_f - \beta_i|$ of the change.

The remapping results in new angular distributions which are shown exemplarily in figure 2.4. In the chosen original $\cos^2\theta_i$ distribution, the changes due to a rotation after attachment are seen most easily. For large rotations the angular distribution can change its shape completely. More importantly however, for small rotations the effect is essentially an averaging over nearby angles. This leads to a decrease in the contrast between highest and lowest yield. The effect is most important for resonances with a forbidden s-wave contribution, e.g. an $A_1 \rightarrow A_2$ transition, where it removes the requirement for the angular distribution to be equal to zero at 0° and 180°.

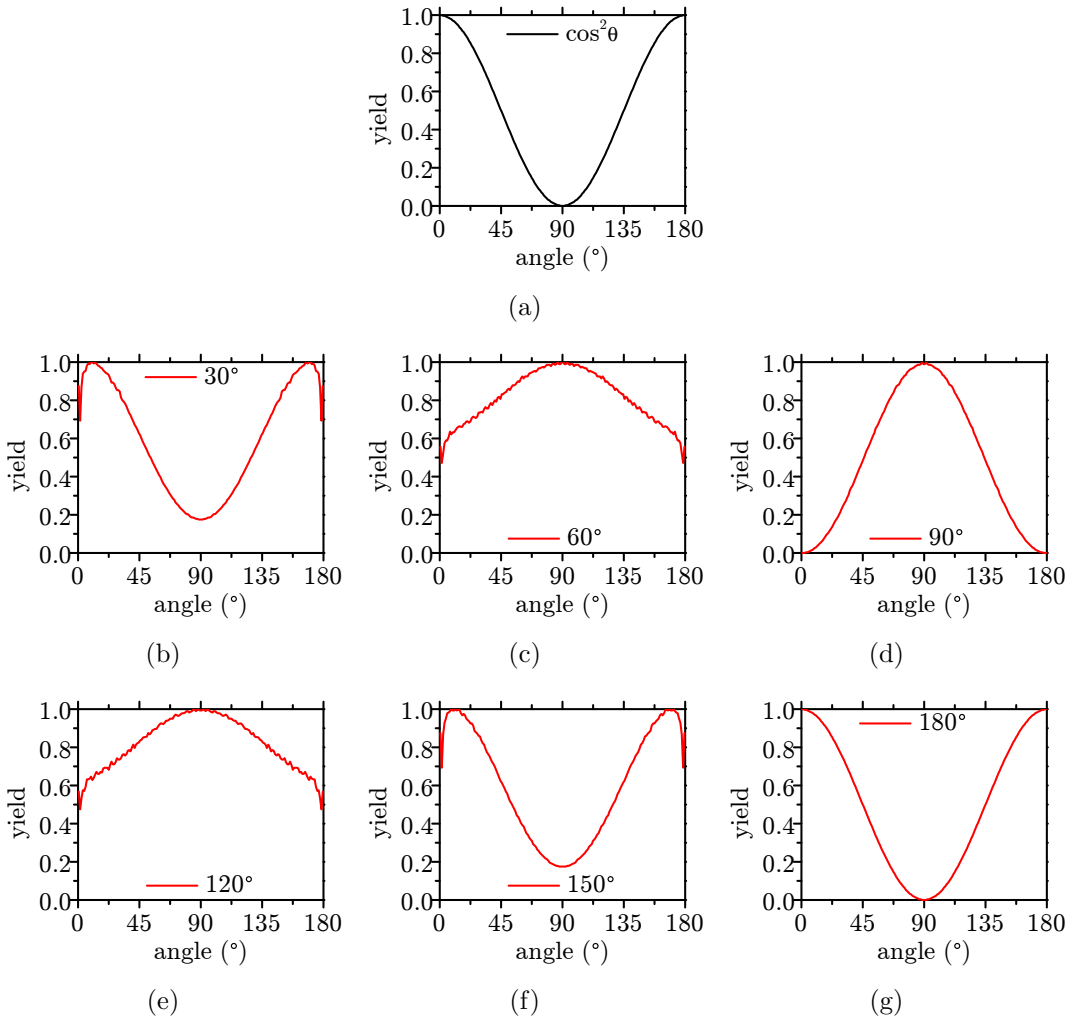

Figure 2.4: Changes in the observed angular distributions when changing the dissociation angle relative to the molecular symmetry axis, shown at the example of a $\cos^2\theta$ function. The original function is shown in (a). The angle given in each diagram (b)-(g) is the angular change $|\beta_f - \beta_i|$.

3. Metastable states detection experiment

The experiments on electron impact excitation have been carried out in the Heidelberg metastable state detection setup. This chapter gives a description of the experimental apparatus used in the present work. In the first part of this chapter, the experiment is described in general. Then its main components - electron source, target preparation system, and detection system - are described. Those components have also been used in the dissociative electron attachment experiment, which will be described in chapter 4. Finally, this chapter explains the analysis of the recorded data and its comparison to theoretical calculations.

3.1 General description

In general, our setup uses the crossed beam technique. The target atoms are prepared in a supersonic gas jet which is crossed with a pulsed electron beam [127], as shown in figure 3.1. The atoms which have been excited to a metastable state are deflected from their original path due to the momentum transfer from the projectile electron to the atom in the scattering process. The deflection is measured by a time- and position-sensitive microchannel plate detector in the path of the jet. From this deflection, the momentum transfer and thus the projectile scattering angle and energy loss are reconstructed.

The target gas is introduced into the vacuum chamber using a supersonic jet. The gas is expanded into a first vacuum stage through a 30 µm nozzle with a backing pressure of 5 bar. The gas jet is cropped using a skimmer with a diameter of 250 µm, which is located 5 mm behind the nozzle and by a second skimmer, 400 µm in diameter after another 20 mm. The regions between nozzle and first skimmer (first jet stage), as well as between the two skimmers (second jet stage) are both pumped separately, keeping a pressure of 2×10^{-3} mbar in the first jet stage and 5×10^{-6} mbar in the second stage. This procedure yields a very cold target jet with temperatures of only a few Kelvin. The jet then enters the measurement chamber which is kept at a pressure around 3×10^{-8} mbar. There it is cropped a third time to restrict the

diameter of the jet. For this final cropping, a 500 µm aperture is entered into the path of the jet just above the intersection with the electron beam.

The electron beam is created in a separate vacuum chamber by illuminating a photo-cathode with a pulsed IR-laser. The photo-cathode is a GaAs crystal which has been coated with between one and two monolayers of cesium and oxygen to create a negative electron affinity. The energy of the electron beam is set by applying a negative bias voltage to the crystal. This creates a well defined potential difference between the point at which the free electrons are produced and the interaction region in which they are scattered at the target. The pulsed electron beam is guided from the electron gun chamber in which it is created to the experimental chamber in which the actual projectile-target interaction takes place. Both chambers are connected by a 1 mm aperture, keeping the electron gun chamber with a pressure below 10^{-11} mbar isolated from the higher pressure in the measurement chamber. In the electron gun chamber, a set of four electrostatic lenses and one xy-deflection system are used to focus the electron beam onto the aperture. Additionally, a magnetic field along the direction of the electron beam guides and focuses the electrons into the gas jet in the interaction region.

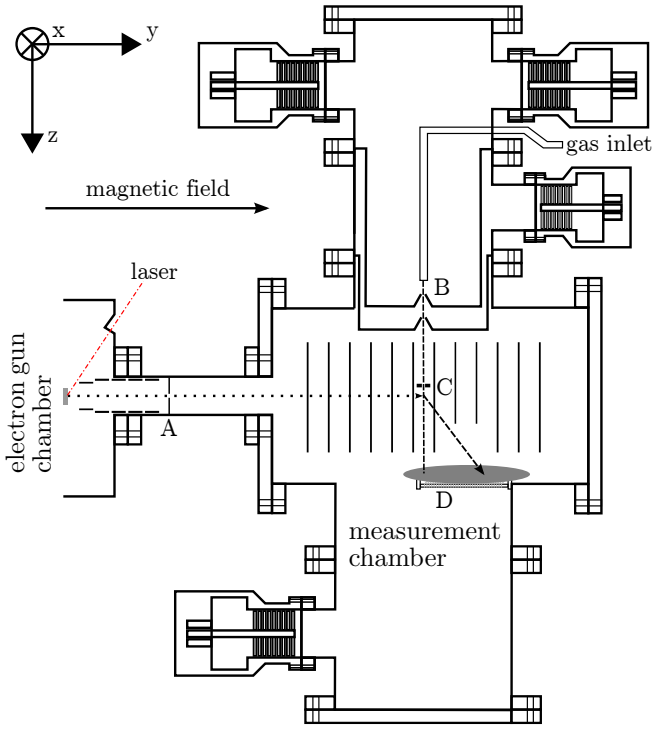

Figure 3.1: Electrons (dotted lines) are created in the photoemission electron source in a separate vacuum chamber (left), focused on the aperture (A) and guided to the interaction region by an axial magnetic field. The supersonic helium jet (dashed line) is created by two skimmers after a nozzle (B) and crosses the electron beam inside the variable potential interaction region (C), where it is additionally collimated by a third aperture. Excited target atoms are detected by an MCP with delay line anode at the bottom (D), allowing precise measurement of the deflection after the electron impact.

The interaction region is enclosed by 18 concentric rings made from stainless steel, each set 10 mm apart from the next one. These rings create a region which is completely shielded from outside electric fields but is accessible for the gas jet as well as for the electron beam. The rings as well as the aperture for cropping the gas jet are set to the same variable voltage to float the interaction region and therefore allow projectile energy scans without the necessity to apply any changes to the voltage settings of the electron gun. Electrons collide with the target in an interaction region with a size of 0.5 mm x 0.5 mm x 2 mm (in directions x-y-z, cf. figure 3.1). In inelastic collisions metastable electronic states can be populated and the target atoms flight path is changed due to the momentum transfer to the atom. The initial

momentum in the supersonic gas jet is about 5 a.u.[1] for helium and the typical momentum transfer in the collision is 1.2 a.u. In this case the atoms are deflected by about 15° from their original path. The lower part of the rings which enclose the interaction region is cut in order to allow the deflected atoms to reach the detector.

The excited atoms are detected using a microchannel plate (MCP) detector with delay-line anodes, allowing measurement of time-of-flight and impact position of the atom. After the electron-atom collision, the flight path of the excited atom is changed towards the direction of the primary electron beam velocity. Since the path can not be influenced as it would be the case when measuring charged particles, the MCP is positioned 110 mm below the interaction point and is also offset by 32 mm in the electron beam direction to allow detection of all excited atoms over the widest possible range of energies.

The accuracy which can be reached in the reconstruction of the momentum transfer depends on the position spread on the detector due to initial thermal spread in the jet as well as on the size of the interaction region. Therefore, a low temperature in the target gas jet as well as a narrow jet are crucial in this experimental scheme.

3.2 GaAs photoemission electron gun

The cathode of a traditional electron gun is heated to create thermionic emission of electrons, resulting in a broad thermal energy spread of around 0.8 eV [2]. Photoemission allows the production of electrons from a cathode at room temperature or even below, which strongly reduces the thermal spread.

Photoemission can occur when a semiconductor like a gallium-arsenide (GaAs) crystal is illuminated with light from a laser. When the photon energy is slightly higher than the band gap, electrons are excited from the valence band to the conduction band in a typical depth of 1 µm (for red/NIR laser light) below the surface. Through extremely fast interactions of the excited electron with phonons in the crystal, it thermalizes to the conduction band minimum and can subsequently be transported to the crystal surface via diffusion. In a bare GaAs crystal the energy of the conduction band minimum is well below the vacuum energy, i.e. the crystal has a positive electron affinity and electrons require additional energy to leave the material. The electron is therefore trapped in the crystal. The electron affinity can be lowered when the crystal is coated with half an atomic layer (monolayer) of cesium. An additional coating with one monolayer of oxygen decreases the electron affinity even further. In p-doped GaAs crystals the vacuum energy can even fall below the energy of the conduction band minimum. This situation is called negative electron affinity (NEA). At this point electrons can be emitted from the conduction band minimum of the crystal into the vacuum. If the crystal has a vanishing negative electron affinity, i.e. energy is neither spent nor gained when an electron is emitted from the crystal, the energy spread of the electron is determined solely by the thermal distribution. Otherwise electron energy spread is increased by surface effects, especially band-bending in p-doped crystals.

Gallium-arsenide crystals have been used as photoemission electron sources in the past [88, 89, 91, 125]. Electron currents in the range of several mA could be reached

[1] The atomic unit of momentum a.u. - with $1\,\text{a.u.} = 1.9929 \times 10^{-24}\,\text{kg m s}^{-1}$ - is used throughout this work when referring to momenta of particles.

at energy spreads of only 7 meV in some studies [89]. However, this performance can only be obtained when the electron gun is cooled using liquid nitrogen, which was not done in our setup.

In the present work, a p-doped GaAs/AlGaAs heterostructure crystal which has a hole concentration of $6 \times 10^{18}\,\mathrm{cm}^{-3}$ due to Zn atoms in the crystal structure is used[2] [106]. Negative electron affinity of the crystal is reached by a coating with cesium and oxygen. The p-doping of the crystal also causes a band-bending, i.e. the energy of the valence band and the conduction band is lowered at the surface of the crystal. Therefore, electrons in the conduction band move towards the edge of the crystal where they can tunnel through the thin potential barrier which is created by the coating and escape into the vacuum. A diode-laser with a wavelength of 786 nm (photon energy: 1.58 eV) provides just enough energy to bridge the band gap in GaAs, which at room temperature is 1.42 eV [102]. This is used to excite electrons close to the valence band maximum to the conduction band of the crystal.

Crystal preparation

The photoemission process relies on a atomically clean crystal surface which is free of any contamination. This is achieved by a preparation of the crystal surface in several steps. Firstly, the crystal is cleaned in boiling toluene and isopropyl alcohol to remove any dirt from the surface. Secondly, the crystal is etched in a 1:5 solution of hydrochloric acid:isopropyl alcohol and in a 20:1:1 solution of sulfuric acid:hydrogen peroxide:water to remove the top layer of the crystal and create a clean surface without any contamination. The next step of the surface preparation is performed in the oxygen-free environment of an Argon-filled glove box. There, a final etching process with a 1:60 solution of hydrochloric acid:isopropyl alcohol removes the upper layer of gallium atoms, thereby creating a protective arsenic capping layer on the surface.

The crystals are then stored in a crystal holder inside the glove box. The crystal holder is a closed system, which can be sealed and mounted to the load-lock-chamber of the high vacuum system without contact to the atmosphere.

The last part of the crystal preparation is the surface activation, which is done in the ultra high vacuum system. A crystal carrier can be picked up using a manipulator and placed in the preparation chamber which operates at a pressure of 10^{-12} mbar. There, the crystal is heated to a temperature of 450 °C. At this temperature the arsenic capping layer at the surface of the crystal is evaporated, resulting in an atomically clean surface.

Surface coating

In the preparation chamber, the crystal is coated with cesium and oxygen. The substances are evaporated in front of the crystal in a controlled manner and allowed to be deposited on the surface. During coating, the crystal is illuminated with red

[2] The heterostructure crystal has a very thin (0.9 µm) active GaAs layer, followed by an AlGaAs buffer layer. The band gap of the buffer layer is 1.96 eV which limits electronic excitation to the active layer. This setup reduces the diffusion time of the electrons in the conduction band and allows the production of short electron pulses below 1 ns. However, the ability to produce short pulses is not used in this work.

laser light. The crystal is set to a voltage of −9 V which accelerates emitted electrons towards the camber walls and the resulting photoemission current is monitored using a pico-amperemeter. In a first step, the surface is coated with cesium for up to 20 minutes, until a first maximum in the photo-current is reached. After that, cesium and oxygen coating is performed alternatingly, always switching between both materials when the photoemission reaches a maximum and starts decreasing again.

The coating is complete when the photoemission current measured at the end of an oxygen coating cycle does not increase compared to the last cycle. An example of the photoemission current in a coating process is shown in figure 3.2. The highest photoemission current is typically reached after 7-10 cycles. The crystal carrier is then transferred into the electron gun chamber and mounted in a dedicated cathode mount where it produces the electron beam for the experiments.

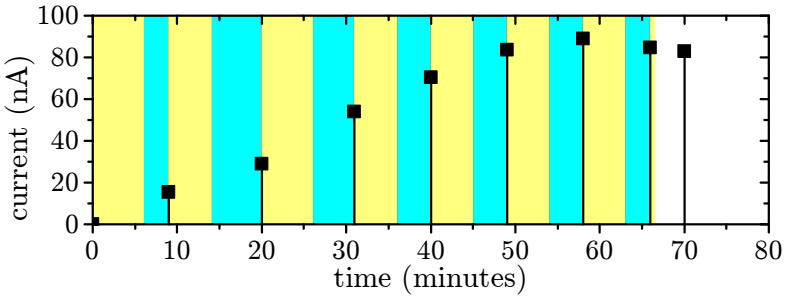

Figure 3.2: Development of the photoemission current during the application of the cesium and oxygen layers onto the GaAs crystal. The yellow background indicates times of cesium deposition and blue background indicates oxygen deposition.

The performance of the photo-cathode can be described by the quantum efficiency, i.e. the ratio of the number of emitted electrons to the number of incident photons. The quantum efficiency η can be calculated as

$$\eta = \frac{hc}{e\lambda}\frac{I}{P} \tag{3.1}$$

with h being Planck's constant, c the speed of light, e the electron charge, λ the laser wavelength, I the photoemission current and P the laser power. Our cathode reaches a maximum current of 67 µA from 100 mW laser power at 786 nm. This corresponds to a quantum efficiency of 0.1%. While this value is lower than reported in previous studies of GaAs photocathodes [57, 90], the achieved current is sufficient for our purposes.

Laser system

The illumination of the crystal in the electron gun is performed by a Toptica DL100 diode laser system, supplying a continuous single-mode laser beam of 786 nm wavelength with an output power of 200 mW. The laser setup is shown in figure 3.3. The beam is guided to and focused on a 400 MHz acousto-optic modulator. The incidence angle is tuned so as to transfer 70% of the laser power to the first diffraction maximum, which is guided to further optics and focused to a beam diameter of around 1 mm^2 onto the GaAs crystal. The acousto-optic modulator can then be used

to switch the illumination of the crystal on and off with a rise and fall time of 25 ns. This way, electron pulses with lengths ranging from 50 ns to 1 µs and with repetition rates from 50 kHz to 80 kHz are commonly created for use in the experiments.

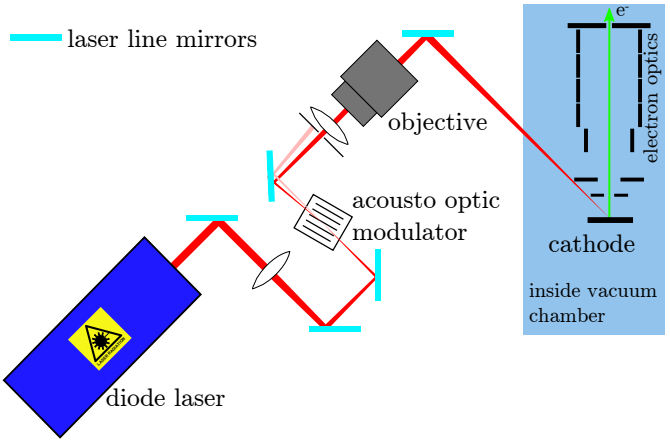

Figure 3.3: Sketch of the laser setup for illuminating the cathode of the NEA electron gun. The laser beam is chopped by guiding it through an acousto-optic modulator and selecting the first diffraction maximum for illumination of the cathode.

Electron gun vacuum system

The photo-cathode requires ultra high vacuum conditions to function properly. Any residual gas in the vacuum chamber can be deposited on the crystal surface over time, thereby destroying the negative electron affinity. Additionally, if electrons ionize residual gas in the chamber, the ions will be accelerated towards the crystal and can destroy the surface layer on impact. As a result, the lifetime of the photo-cathode depends strongly on the pressure inside the vacuum chamber.

The GaAs crystal which serves as an electron source is placed in a separate vacuum chamber which is pumped by a Pfeiffer TMU 521 P turbo-molecular pump. The chamber is heated to 250 °C for one week before use to reach a base pressure of 6×10^{-12} mbar. The electron gun chamber is connected to the experimental chamber only via a 1 mm aperture. This reduces contamination of the vacuum from the higher pressure in the experimental chamber which is around 3×10^{-8} mbar in electron impact excitation experiments and around 5×10^{-9} mbar in dissociative electron attachment experiments. The electron gun itself consists of the cathode, followed by two apertures, four einzel lenses and one xy-deflection unit to focus the electron beam onto the aperture to the experimental chamber. Further guidance of the electron beam is provided by a magnetic field of 1.7 mT to 2.5 mT. In the experiments, a photo-cathode lifetime of one week can be reached.

3.3 Supersonic gas jet

The goal of our experiments is to measure the momentum of atoms and molecular fragments. The best momentum resolution can be obtained only if the target gas has a well defined momentum before the interaction. This condition is met by the use of a supersonic gas expansion [47, 120]. The target gas is expanded through a nozzle with a diameter of 30 µm at a stagnation pressure between 1 bar and 5 bar. When gas jets are produced from heated liquids, a 100 µm nozzle is used instead to prevent blocking due to contamination or condensed droplets and a lower stagnation pressure of around 1 bar is used. The experimental layout of the supersonic jet production

line is shown in figure 3.4. During the isentropic expansion through the nozzle a part of the stagnation enthalpy H_0 is converted to kinetic energy $\frac{1}{2}mu^2$ in the directed movement of the gas:

$$H_0 = H + \frac{1}{2}mu^2 \tag{3.2}$$

$$c_pT_0 = c_pT + \frac{1}{2}mu^2. \tag{3.3}$$

Here, c_p is the specific heat of the gas at constant pressure, T_0 is the reservoir temperature, T is the temperature in the gas stream along the jet direction and u is the stream velocity of the jet. This process leads to a cooling in the translational degrees of freedom of the gas. When the gas expands through the nozzle, it reaches its speed of sound inside the nozzle. If the pressure ratio between the pressure inside the nozzle (P_0) and the background pressure inside the vacuum chamber (P_b) is larger than $P_0/P_b = 2.1$, the gas will leave the nozzle with higher pressure than its surrounding and will be further accelerated when expanding into the vacuum, thereby surpassing its speed of sound and creating a supersonic flow [76]. Inside this supersonic zone (the *zone of silence*, B in figure 3.4), the flow cannot be influenced by any upstream disturbances because any disturbance can only propagate at the speed of sound [104]. This leads to the creation of shock waves which limit the size of the supersonic region and create a boundary region with high temperature, pressure and change in velocity (the *barrel shock*, C in figure 3.4). To keep the supersonic jet stable, a skimmer is inserted inside the zone of silence, cutting off the barrel shock from the supersonic region and leaving a narrow supersonic jet. A second skimmer is inserted behind the first one to further constrain the divergence of the jet and to allow for differential pumping. Thereby, the high pressure of 10^{-3} mbar in the first jet stage is further separated from the experimental chamber. The supersonic jet created by this system reaches a gas density of $1.5 \times 10^{11}\,\mathrm{cm}^{-3}$ in our electron impact excitation experiments.

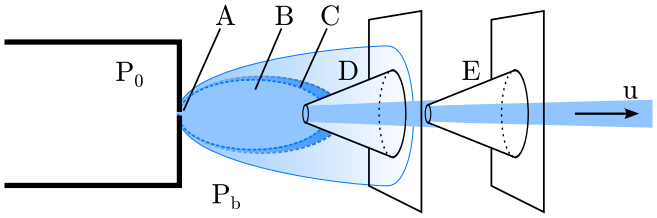

Figure 3.4: Path of the target gas: A) supersonic expansion through a nozzle, B) zone of silence, C) barrel shock, D) first skimmer inside the zone of silence creates a stable supersonic jet, E) second skimmer further constrains the radial dimensions of the jet.

The complete gas inlet system can be heated using a resistive heating wire inside the vacuum chamber and heating tapes outside the chamber. When using a liquid as a target, it is heated in an external reservoir (the bubbler) to a temperature at which the vapor pressure is at least 500 mbar. This bubbler is connected to the heated gas inlet system and additionally to a gas supply through which an inert seeding gas is added to the reservoir, increasing the overall pressure and thereby ensuring a stable supersonic expansion. When using a heated bubbler as a gas source, care has to

be taken to have an increasing temperature along the path of the gas, to prevent condensation of the target and subsequent blocking of the gas inlet.

3.4 Detection system

The atoms in excited states after inelastic electron scattering are detected using a microchannel plate (MCP) detector with a diameter of 80 mm combined with delay line anodes, which is shown in figure 3.5. For the dissociative electron attachment experiments performed in the Heidelberg DEA setup (cf. section 4.1), negative ions which were created in the DEA process are recorded with the same system.

Microchannel plates

The microchannel plates consist of an array of secondary electron multiplier (SEM) tubes with a diameter of 25 µm. The SEM tubes are tilted by 8° from the normal of the detector surface. A sketch of a stack of two MCPs can be seen in figure 3.5. Secondary electrons can be produced by an impact of any energetic particle (e.g. electrons, ions, atoms in excited states, photons) and those secondary electrons are accelerated towards the backside of the the MCP by a voltage of 1 kV. After the multiplication of the secondary electrons due to several hits of the SEM tube's walls, 10^4 electrons leave the microchannel plate. A second microchannel plate is placed behind the first one. By turning it so that the tilt of its SEM tubes points in the opposite direction than that of the first plate, no incoming particles can pass through the detector without hitting it and an overall amplification of 10^8 is reached when applying a voltage of 2 kV over the stack of the two microchannel plates. When a particle hits the detector and creates an electron cascade, the voltage applied over the MCPs drops slightly. This short voltage drop has a length on the order of 10 ns and is coupled out to be used as the time-of-flight information.

Delay-line anodes

Behind the MCP, delay-line anodes are wound to measure the position at which the particle hits the MCP. There are a total of four delay lines wires, one pair for measuring the x-position and another pair for measuring the y-position on the detector. The two wires of each pair are a signal wire and a reference wire. The wires of one pair are wound so as to cross the area behind the MCP from top to bottom while the other pair crosses the area from left to right. This arrangement is shown in figure 3.5, except that each pair of wires is represented as only a single colored wire for simplicity. One wire in each pair (the signal wire) is set to a potential of 400 V above the backside of the MCP to collect the electron cloud created by the MCP. The other wire is set to only 350 V above the backside of the MCP and is used as a reference signal. Since the reference wire is very close to the signal wire over its whole range it will be subjected to the same noise but at the lower voltage it will receive only a small amount of the electron cloud. The electrical signals from both ends of the wires are also coupled out to obtain the signal at ground potential rather than at the potential of the delay-lines. The two output signals from the same side of both wires in a signal- and reference-wire pair are amplified using a difference amplifier to effectively suppress the noise.

Due to its size, the charge cloud will be deposited only on a few windings of the wires, according to its position. From there the electric signals induced in the wire by the

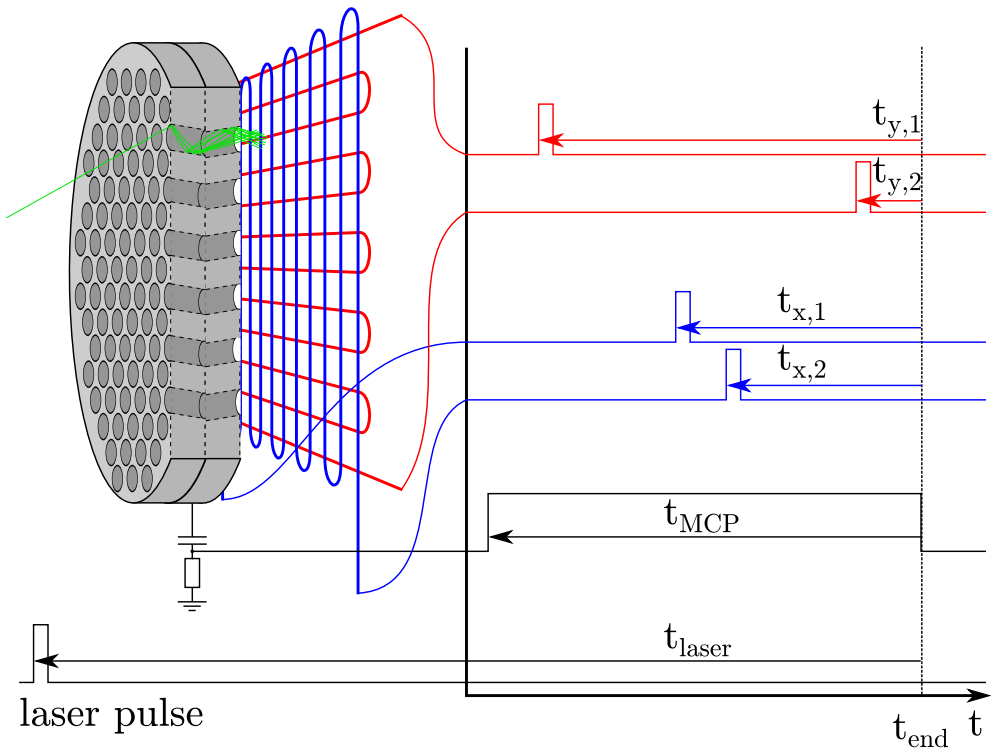

Figure 3.5: Sketch of an MCP and delay line detection system. Electrons (green) are multiplied in the SEM tubes, then the electron cloud is deposited onto the delay line wires which independently measure horizontal (blue) and vertical (red) position.

charge travel in both directions to the ends of the wire. Depending on the position of the hit, the signals arrive at the two ends of the wire at different times which is used to calculate the position of the hit in the direction perpendicular to the winding direction of the delay line. A second, identical delay line anode perpendicular to the first one is used to measure the position in the remaining direction.

The delay lines therefore give four signals. For both delay line directions these are the two times at which the signals from the charge cloud, deposited on the wires, reach the ends of the wires.

Electronics

The electronics process the five signals coming from the detector (MCP hit time and four delay line times). An additional timing signal t_{laser} is provided by the trigger of the laser which produces the electron beam and it serves as a reference for the starting time of the time-of-flight (cf. figure 3.5). These signals are amplified by an ORTEC FTA 820 A Fast Timing Amplifier and converted into NIM signals by ORTEC 935 Quad 200-MHz Constant-Fraction Discriminators (CFD). The CFD for the microchannel plate signal is set to produce a pulse which is 200 ns long while the CFDs for the delay line signals produce signals with a length of 40 ns as shown exaggeratedly in figure 3.5. This method ensures that the falling edge of the MCP signal occurs later than the rising edges of the delay line signals which are read by the time-to-digital converter (TDC). The TDC is operated in a common stop mode, therefore the rising edge of the signals described above (including the MCP signal) are used as a start of time measurements while the stop for all channels is provided

by the falling edge of the MCP time signal.

To allow for automated energy scans of the electron beam, the projectile energy can be changed during the experiments. When the GaAs photoemission electron gun is used, the projectile energy is changed by floating the interaction region to a specific potential. The change in the potential is achieved by applying a sawtooth voltage in the range from $-10\,\mathrm{V}\ldots10\,\mathrm{V}$ to the interaction region. This variable offset voltage is read by a hytec 521 12bit analog to digital converter (ADC). A time delayed copy of the MCP signal is used to trigger the data readout into the PC. This time delay is necessary to ensure that all signals have been processed by the electronics before starting the read out.

Signal processing

All data is read out by the CoboldPC 2002 analysis program. The time information is recorded with a resolution of 0.5 ns. This constant step size between the data of all recorded events would lead to the creation of Moiré patterns when it is not displayed with the correct bin size. To avoid this problem, a random value between $-0.25\,\mathrm{ns}$ and $+0.25\,\mathrm{ns}$ is added to every time information, thereby filling the whole range of possible times while not reducing the resolution. For every recorded event, the correct time-of-flight t_f is calculated by

$$t_f = t_{laser} - t_{MCP} \tag{3.4}$$

where t_{laser} is the time between the laser pulse and the end of the MCP signal and t_{MCP} is the length of the MCP signal (cf. figure 3.5). The position of the particle is calculated using the time signals $t_{wire,1}$ and $t_{wire,2}$ of the two ends of the same delay line in the following way:

$$\mathrm{position}_{wire} = (t_{wire,1} - t_{wire,2})v_{signal} \tag{3.5}$$

where $wire$ is either x or y and v_{signal} is the speed with which the signal travels in the direction perpendicular to the wiring. Because the total distance traveled by the two signals is always the length of the wire and therefore constant, the time sum of the two ends of one wire has to be constant as well. The time sum t_{sum} is calculated by

$$t_{sum} = 2t_{MCP} - t_{wire,1} - t_{wire,2}. \tag{3.6}$$

The resulting time sum is constant for all real events within 10 ns and is ideally suited to distinguish false events - where at least one recorded time values does not belong to the correct particle or is missing completely - from correct ones.

3.5 Analysis of recorded data

When an atom is excited by an inelastic collision with an electron, momentum is transferred to it. To understand the momentum transfer, it is advantageous to consider a two step process in which the electron is first captured and then ejected again with a lower energy. A capture into a transient negative ion only takes place in resonant scattering but since the final state does not depend on this, the picture is useful to understand the momentum transfer in all cases.

When the electron is captured, the whole momentum of the electron is transferred to the atom-electron system. When the electron is ejected again, it has a lower momentum due to the energy loss in the electronic excitation of the atom. It can be ejected in any direction, again transferring the opposite momentum to the atom to conserve momentum. The kinetic energy of the target is negligible due to its high mass compared to the electron. In the end, the momentum of the atom in the excited state can lie on any point of a sphere for which the radius depends on the excited state and the center is the initial momentum of the projectile.

The initial momentum of an atom is not precisely known due to its thermal motion. At room temperature the average kinetic energy of an atom is around 25 meV, while the change in the kinetic energy of the atom due to the inelastic scattering is only 0.3 meV. The initial distribution of the atom thus has to be restricted by the cooling and collimation in the supersonic gas jet. The supersonic gas jet can reach a kinetic energy spread along the flow direction of around 0.12 meV, corresponding to a temperature of 3 K in this direction.

The momentum spread perpendicular to the flight direction (x-y-plane) usually is an order of magnitude lower than in the flight direction (z-direction). Therefore, the momentum resolution differs strongly between the detector plane and the z-direction and a complete measurement of the 3D-momentum is not possible. While the resolution in the detector plane is sufficient to measure momentum transfer to the atom in this plane, the momentum resolution in the jet direction is too low for meaningful measurements.

To reduce the influence of the momentum spread in the z-direction on the observed momentum distributions, two different methods are used. The first method consists of the use of a very narrow (±50 ns) time-of-flight window that cuts out most of the events where scattering did not take place in the x-y-plane. Because the collision process has a rotation symmetry around the electron impact direction (y-axis), all the information is contained in a cut which includes the y-axis. This method increases the structure which is visible in a momentum image but it uses only a small portion of all the available data. In the second method, all momenta are projected on the x-y-plane and an inverse Abel transformation is used to reconstruct the original distribution, rendering knowledge of the momentum in z-direction irrelevant. The inverse Abel transform will be described in section 4.3. In both cases the results are compared to a simulation of the experiment using calculated differential cross sections from different theoretical methods [8, 41].

Energy considerations

Due to the fact that the target atoms move undisturbed by any external forces after the collision, the calculation of the momentum transfer **q** to the target is straightforward:

$$q_x = m\frac{x - x_0}{t_f} \tag{3.7a}$$

$$q_y = m\frac{y - y_0}{t_f} \tag{3.7b}$$

$$q_z = m\frac{d_z\,(t_{f,0} - t_f)}{t_{f,0}t_f}. \tag{3.7c}$$

Here, m is the mass of the target atom and d_z is the distance between interaction region and detector along the z-direction. x, y and x_0, y_0 are the coordinates at which an atom with and without momentum transfer would hit the detector, respectively. Analogously, t_f and $t_{f,0}$ are the times-of-flight from the collision point to the detector with and without momentum transfer. The complete set of momenta is shown in figure 3.6. The momentum calculated in equations (3.7) is the target momentum transfer $\mathbf{q}$ and it is equal to the change in electron momentum $\mathbf{p}_{e,0} - \mathbf{p}_{e,1}$. It can be used to calculate the final electron momentum

$$\mathbf{p}_{e,1} = \mathbf{p}_{e,0} - \mathbf{q} \tag{3.8}$$

where the initial electron momentum $\mathbf{p}_{e,0}$ is known from its energy and impact direction. The momentum transfer to the target $\mathbf{q}$ differs from the final target momentum $\mathbf{p}_{t,1}$ by the initial downwards momentum of the target atom in the jet (cf. figure 3.6). This initial momentum is already corrected for by using the time-of-flight difference from the undisturbed jet in equation 3.7c.

The calculated momenta q_x and q_y are used to create 2D-momentum transfer images, which show the likelihood of producing an atom with those momentum components in the inelastic collision with an electron. When momenta with all z-values are used, we obtain a projection onto the x-y plane from which the original distribution in this plane is reconstructed using the Abel inversion, which will be described in section 4.3. If only momenta with low z-values are used, we obtain the cut through the momentum sphere. The momenta of the atoms after the collision can then be used to create momentum images of the electrons. While a momentum transfer image of the target atom is centered around the incident electron energy, the momentum image of the projectile electron is the inversion of the target momentum image and is centered at zero. In this work, momentum images of the scattered electrons will be used to represent the experimental results.

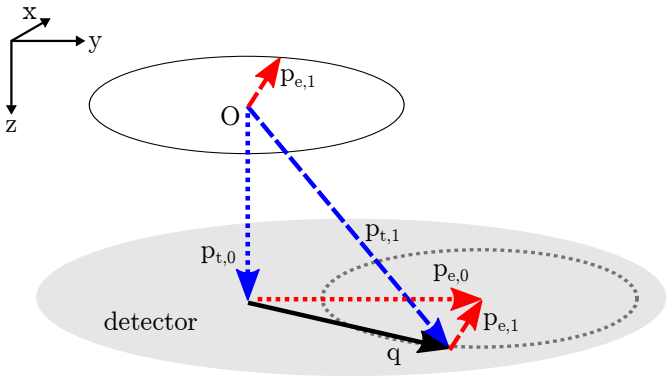

Figure 3.6: Overview of the momenta of electron and target atom before and after the collision. Collision center is at O. For simplicity, only momentum transfer in the x-y plane is shown. Initial momenta are shown in dotted lines, final momenta in dashed lines, and the momentum transfer is shown in a solid line. Target momenta are shown in blue, projectile momenta in red.

Due to the high mass of the target compared to the mass of the projectile electron, the kinetic energy of the atom obtained in the collision is negligible. The momentum of the atom can be used to calculate the energy loss of the projectile electron. This energy loss corresponds to the excitation energy E_{exc} and can be used to identify the electronic state which has been populated in the target:

$$E_{exc} = E_i - \frac{\left(|\mathbf{p}_{e,0} - \mathbf{q}|\right)^2}{2m_e}. \tag{3.9}$$

Here, m_e is the electron mass. Every accessible excitation energy corresponds to an electronic transition in the target atom.

Simulation of the experiment

We compare the scattered electron momentum images with theoretical calculations. Usually, angular distributions of electrons are investigated separately for every excited state. However, the angular distributions of energetically close lying excited state can not be completely separated. E.g. the contributions from $2\,^1$S state and the $2\,^3$P state in electron impact excitation of helium (cf. table 5.1) are overlapping in the acquired momentum images. The comparison with theory is therefore done by simulating the experiment as precisely as possible using the differential cross sections provided from different *ab initio* theoretical calculations and creating expected electron momentum images, which are then compared to the experimentally obtained images. The simulation is creating a certain number of scattering events and calculates the measured momentum from the resulting hit position on the detector considering statistical distributions in the following quantities: target velocity in jet direction, collision position within the projectile-target overlap volume, and projectile energy. The uncertainties from a target velocity spread perpendicular to the jet direction are much lower than those due to the size of the interaction region and are therefore neglected in the simulation. For every excitation channel, a uniform angular distribution of events is created sampling the whole range of starting conditions. Next, detection positions and the resulting observed scattering angles are calculated from the momentum transfer for these events. Every event is then weighted according to the differential cross section which depends on the excitation process and the scattering angle. This approach ensures the same statistical uncertainties independent of the cross section.

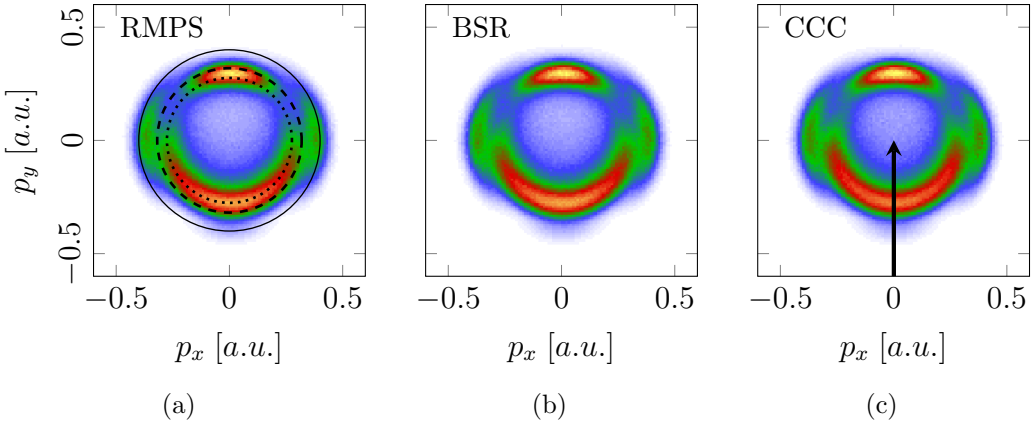

Figure 3.7: Momentum distributions of inelastically scattered electrons from helium at an impact energy of 22.2 eV, obtained by the numerical simulation of the experiment using differential cross section data from (a) R-matrix with pseudo-states (RMPS), (b) B-spline R-matrix (BSR) and (c) convergent close-coupling (CCC) calculations. The black circles in the first picture indicate the expected momentum for the $2\,^3$S-state (solid line), $2\,^1$S-state (dashed line) and $2\,^3$P-state (dotted line). Due to the projection of some out-of-plane scattering, the measured momentum is shifted to slightly lower values. Electron impact is along the positive p_y-direction as indicated by the black arrow in (c).

Figure 3.7 shows the simulated electron momentum distributions from electron impact excitation of helium at an electron energy of 22.2 eV using differential cross sections of three different theoretical methods as an input. As can already be seen here, all theoretical models predict very similar momentum images. For these calculations, the velocity along the jet axis (i.e. the direction normal to the detector plane) has been restricted to $\pm 50\,\mathrm{m\,s^{-1}}$ around the mean jet velocity, as it is also done in the experiment and the incident electron momentum is set along the positive p_y-direction. Figure 3.7(a) also shows the actual momenta of atoms in three different excited states under ideal conditions as black circles. It can be seen in the figure that the simulated momenta are smaller than the actual momenta due to the projection of out-of-plane momenta on the detector plane. Also, the outer $2\,^3$S-state contribution with its main cross section maximum around 90° and a small contribution at backward scattering (i.e. high negative p_y-values) can clearly be separated from the contributions of the other excitation channels. Momentum distributions of $2\,^1$S- and $2\,^3$P-excitation are overlapping though. Only by comparing the momentum distributions of forward and backward scattering it is possible to recognize the contribution of the $2\,^3$P-state at lower absolute values of negative momenta corresponding to backwards scattering.

To counteract the projection effects from scattering out of the detector plane and simultaneously increase statistics by using all events, the momentum distribution in the detector plane can also be reconstructed from the projection of all events onto the detector plane using an Abel inversion as described in section 4.3. The same results can be obtained in the simulation when scattering is restricted to the detector plane which allows a comparison of experimental results and theory for this type of data analysis as well.

4. Dissociative electron attachment experiments

In this chapter, the two experimental setups are described which were used to study dissociative electron attachment (DEA) in this work. The first setup is the Heidelberg DEA apparatus which has been built at the Max Planck Institute for Nuclear Physics during this work, and second one is the existing GASIC apparatus at the Open University in Milton Keynes, United Kingdom.

4.1 The Heidelberg DEA apparatus

The Heidelberg dissociative electron attachment setup employs the same crossed-beam technique as used in the production of excited atoms but it omits the extra aperture for the gas jet, which is not necessary in this experiment. A drawing of the setup is shown in figure 4.1. The target gas is inserted into the experimental chamber as a supersonic gas jet. Inside the interaction region, the jet is crossed with a pulsed electron beam from a photoemission electron gun, producing the anionic fragments of the target molecule.[1] After the reaction, the ions are guided to the MCP-detector by an electric field which is created by ring electrodes between the interaction region and the detector, called the spectrometer. The extraction direction of the spectrometer is perpendicular to both the electron beam and the gas jet. Since the electric field of the spectrometer would deflect the projectile electrons and prevent them from reaching the gas jet, the spectrometer is operated in pulsed-mode. The field in the interaction region is only switched on 1 µs after the electron pulse has passed the spectrometer and is collected by a Faraday cup. This prevents electrons from being deflected from their intended path and from colliding with other parts of the apparatus. The experiment is based on the working principle of similar setups [2, 79, 81]. Several parts like the supersonic gas inlet and the photoemission electron gun are the main improvements over previously existing machines.

[1] A detailed description of electron source, gas target preparation, and detection system has already been given in chapter 3.

In the DEA experiments, the GaAs-photoemission gun can also be replaced by a tantalum photoemission gun of a much simpler design, which is placed just outside of the spectrometer but inside the experimental chamber. In contrast to the GaAs gun which has a short operating life-time and demands maintenance after three to five days of operation, the tantalum gun allows long term operation of the experiment.When the GaAs electron gun is used, electron impact energy scans have to be performed by floating potential of the interaction region. The tantalum electron gun on the other hand can be floated itself while the interaction region stays unchanged, making experiments with variable electron impact energy much easier.

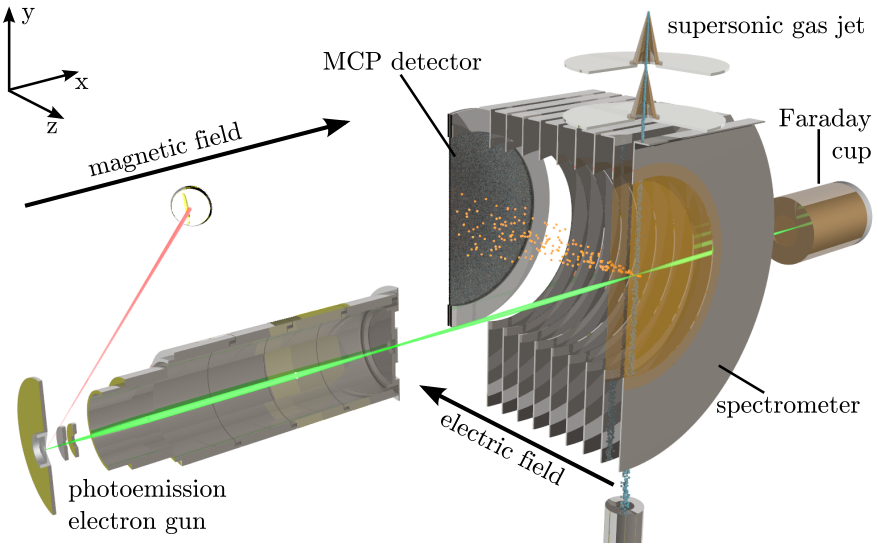

Figure 4.1: Illustration of the DEA setup. The laser (red) creates a pulsed electron beam (green) which is crossed with a supersonic gas jet (blue dots). Created ions (orange dots) are guided onto the MCP-detector by the electric field of the spectrometer.

The spectrometer in this setup consists of nine steel rings, each set 10 mm apart from the next one and is divided into three sections (cf. figure 4.2). The first section consisting of the volume between ring one and two - where the reaction takes place - is called the pusher plate region. These two rings are covered with a conducting grid to screen the electric field from other parts of the setup and to enable the production of a large potential gradient. The first ring is pulsed to a negative voltage between 20 V and 60 V. Ions in the interaction region are pushed into the acceleration section between rings two and five. These rings are connected in series by 100 kΩ resistors to produce a constant voltage gradient. The electric field in the first stage, which is produced by the pulsing of the first plate, should be identical to the field in the acceleration section. Finally, the third section between ring five and nine creates the drift section. In this section the voltage of the rings is kept constant and the ions move towards the MCP-detector in a field free region. When the acceleration region is half as long as the drift region which follows it, the spectrometer geometry is called the Wiley-McLaren geometry [129] and it compensates the spread of flight times of particles with different starting points. This so called time focusing is needed due to the size of the interaction region of about 2 mm x 2 mm x 2 mm. In our setup the acceleration region has a length of 35 mm and the drift region has a length of 50 mm, thereby coming close to the optimum geometry.

The fast pulsed first plate in the spectrometer acts as an antenna and the MCP as

a receiver creating false signals in the MCP channel. To circumvent this problem, a hardware veto is set on the MCP channel of the electronics processing hardware, allowing only signals that are produced after the pulsing of the spectrometer to trigger the data acquisition.

The acceleration and drift sections in the spectrometer are not separated by a conducting grid and therefore field-penetration leads to an electric potential as sketched in figure 4.2 in the red line. This field geometry is accepted because it increases the mass resolution of the system as compared to a sharp edge between acceleration and drift section while the time focusing is only slightly altered.

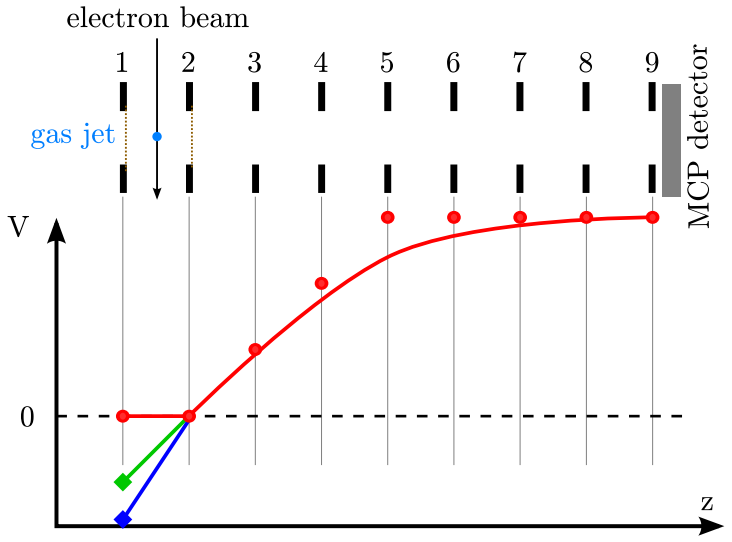

Figure 4.2: Sketch of the voltages applied to the spectrometer. The red circles show the voltages when the electron gun is firing, while the green and blue diamonds show the change after the first spectrometer plate (pusher plate) is pulsed to different negative voltages. The lines represents the resulting electric field on the spectrometer axis. Between spectrometer plate 1 and 2 the red line shows the field when the electron gun is firing, the green line shows the spectrometer working in the 3D-momentum measurement mode with low mass resolution an the blue line shows the 2D-momentum measurement mode with high mass resolution. The sketch of the experiment above the graph illustrates the location of the electric field.

The spectrometer can be operated in two different modes, which are shown in figure 4.2. The two modes differ in the height of the voltage pulse on the first spectrometer plate, which pushes the ions towards the detector. The first mode is a 3D-momentum measurement mode with low mass resolution and it is shown by the green line. In this mode the ions are accelerated by the same electric field in the pusher plate region and in the acceleration region. The second mode is a 2D-momentum measurement mode with high mass resolution, shown by the blue line in figure 4.2. In this case the electric field in the pusher plate region is higher than in the acceleration region, resulting in two different acceleration stages inside the spectrometer. In general, ions with initial momenta away from the detector start at a higher potential because the electric field is activated only after they moved freely for 1 µs. From their new starting position they are accelerated stronger while ions which move towards the detector after the reaction start at a lower potential and are accelerated less. This effect reduces the spread of the time-of-flight distri-

bution caused by the momentum of the ions. When the electric field in the pusher plate region is higher than in the acceleration region, this time focusing is enhanced which results in sharper peaks in the time-of-flight spectrum. Since increased mass resolution decreases the momentum resolution in the time-of-flight direction, only the momentum in the detector plane is measured and the complete momentum distributions is reconstructed using the Abel inversion, as described in section 4.3.

Tantalum gun

For some experiments the GaAs electron gun has been replaced by a tantalum-cathode electron gun. The modified setup is shown in figure 4.3.

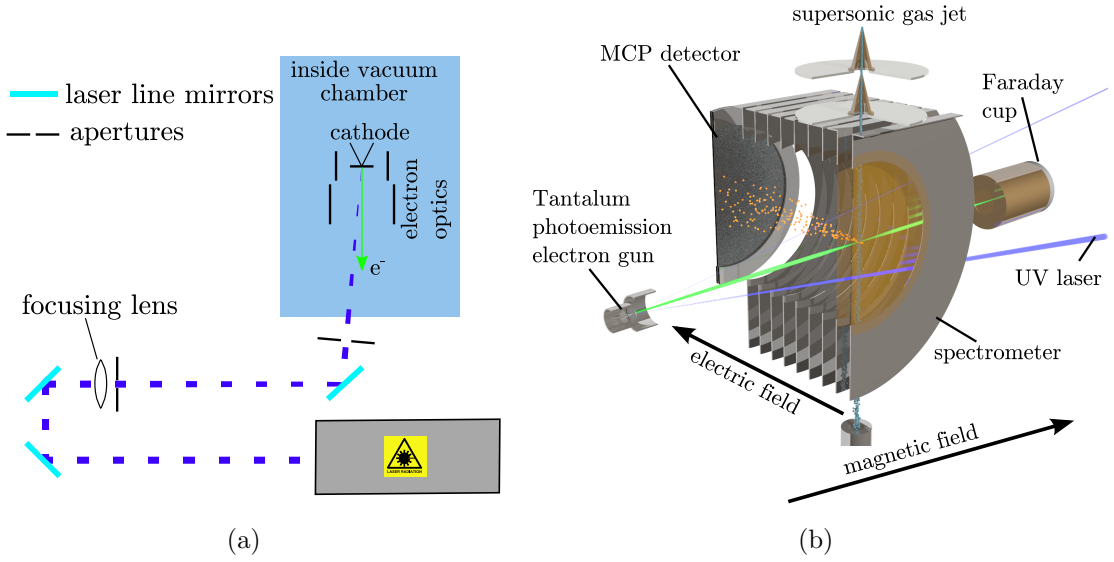

Figure 4.3: (a) Sketch of the laser setup for illuminating the cathode of the tantalum electron gun. The lens focuses the laser beam on the cathode and the apertures are used as guides when adjusting the laser position as well as for varying the laser power. (b) The setup and all relevant parts when the tantalum electron source is used, similar to figure 4.1.

We illuminate a tantalum disc which has a work function of 4.35 eV [109] with a pulsed 266 nm laser (photon energy 4.66 eV, producer: teem photonics, model SNU-20F-100), thereby creating low energetic electrons through photoemission. The laser is focused onto the cathode through a vacuum viewport (transmission: 93% at 266 nm). The reflected light leaves the vacuum chamber through another viewport and is either dumped or imaged by a camera for adjustments. The tantalum electron gun is a very stable electron source and can be used for an almost unlimited amount of time after the surface has been cleaned inside the vacuum chamber by heating the cathode to about 700 °C. It does not require ultra high vacuum, allowing a placement of the gun inside the experimental chamber. Except for the cathode, the only other active components for guiding and focusing the electron beam are two einzel lenses which are sketched in figure 4.3. This minimalistic approach keeps the length of the gun below 4 cm and allows us to place it very close to the spectrometer. It also means that the electron gun relies on the magnetic field for the actual guidance of the electrons towards the target. The energy spread of the electron beam for this gun depends on the difference of the work function and the photon energy as well

as the homogeneity of the work function in the illuminated area. For this reason the area is chosen as small as possible by optimizing the focus of the laser. In the used setup an additional strong dependence of the electron beam resolution on the settings of the two einzel lenses of the electron gun has been observed. A good energy resolution of around 280 meV FWHM has been achieved when using the first lens as a Wehnelt cylinder by setting it to a slightly higher negative voltage than the cathode and blocking electrons with low energy.

When the tantalum electron gun is used in an experiment, the electron impact energy can be scanned by floating the voltage of the photocathode and the two einzel lenses of the gun. This method of changing the projectile energy is simpler to implement than changing the potential of the interaction region which is necessary when the GaAs electron source is used.

Momentum calculations in the Heidelberg apparatus

In the momentum calculation of the particles we have to differentiate between momentum in the detector plane (x-y-plane) and normal to the detector plane (z-direction). In an ideal field geometry, i.e. the electric extraction field is normal to the detector plane (cf. figure 4.1), the velocity of the anions in the plane perpendicular to the extraction field is unchanged. Assuming these perfect conditions, the momentum in this plane is simply

$$\begin{aligned} p_x &= m_{ion}(x - x_0) \cdot t_f \\ p_y &= m_{ion}(y - y_0) \cdot t_f \end{aligned} \tag{4.1}$$

where x, y is the detection position and x_0, y_0 is the point where ions with no initial momentum would arrive. The direction x is the electron impact direction, y is perpendicular to electron impact direction (along the jet direction), and t_f is the time-of-flight, starting from the creation of the ion.

In the direction normal to the detector (time-of-flight direction, z), the ions move freely at first, then are accelerated towards the detector when the spectrometer field is turned on, and finally - when they reach the field free region - they drift towards the detector. Due to the different electric fields in different parts along the spectrometer - especially the time-dependent field in the pulsed region - there is no straightforward way to calculate the initial momentum from the time-of-flight. However, the reverse calculation of time-of-flight from the initial velocity is a simple task and the assignment of time-of-flight to velocity is bijective. Therefore, a look-up table is created containing the corresponding time-of-flight for all expected velocities at a given mass m_{ion}. The derivation of the total time-of-flight t_f is as follows:

$$\begin{aligned} s_{1,f} &= s_{1,i} - v_{0,z} \cdot t_{delay} \\ a_1 &= \frac{eE}{m_{ion}} \\ t_1 &= -v_0/a_1 + \sqrt{(v_0/a_1)^2 + 2s_{1,f}/a_1} \\ v_1 &= a_1 t_1 + v_0 \\ t_2 &= s_2/v_1 \\ t_f &= t_1 + t_2. \end{aligned} \tag{4.2}$$

Here, E is the electric field in the acceleration region. $s_{1,i}$ is the length of the acceleration stage, starting at the jet position. When the electric field is switched on after the effective time t_{delay} the ion has moved to the altered length $s_{1,f}$ due to its movement with the initial velocity $v_{0,z}$ in the time-of-flight direction. Subsequently the acceleration length differs in the calculation of the flight time t_1 through the acceleration stage, where the acceleration is a_1. Then, t_2 is the time the ions take to pass through the drift region with length s_2 and t_f is the final time-of-flight. The time t_{delay} is longer than the set delay and has to be obtained experimentally using calibration measurements. The offset comes from the response time of the pulser and the rise time of the spectrometer pulse. In the calibration measurements it was found that t_{delay} is 310 ns longer than the set delay. The total time-of-flight can also be used for the identification of the mass-to-charge ratio of unknown fragments after calibration.

The created look-up table presents a simple way to determine the difficult relation between time-of-flight and momentum. However, it is only correct for a perfect setup with well defined acceleration and drift region. In the used setup there is no conducting grid between these two stages and therefore the two regions are not well separated. The resulting electric field and the exemplary flight paths of fragments with a mass[2] of 16 amu are shown in figure 4.4. Therefore, the lengths of the two regions in the formula are not the physical lengths but effective lengths which have to be determined experimentally. They are chosen so that they yield the correct time-of-flight for fragments of different masses when comparing to the experimental results in calibration measurements and so that they are also in agreement with simulation of ion trajectories produced using the SIMION software. Due to the form of the electric field, there is a slight time-of-flight focusing, i.e. the time-of-flight spread is reduced, and there is a lensing effect in the detector plane which increases the size of the distribution on the detector. These effects lower the measured momentum by 26% compared to the expected one in the direction normal to the detector plane (time-of-flight direction) and they increase the measured momentum in the detector plane by 20%. These values are found by calibrating the momenta with DEA in oxygen where the expected kinetic energy release is well determined because no energy is stored in internal degrees of freedom.

For the ion trajectory simulation in the SIMION software, the spectrometer geometry has been modeled exactly as it is used in the experiment, including the MCP at its end. The pulsing characteristics of the first spectrometer plate have been directly measured and the voltage pulse has been modeled by an exponential saturation function with a time constant of 175 ns. The ions have been started with an initial downwards velocity due to the average speed of the supersonic gas jet. The time-of-flight and position distribution of ions in the simulation are in good agreement with experimental results. The simulation confirms that the imaging of the momenta works properly, i.e. there is a linear dependence between position on the detector and ion momentum, despite the imperfect field geometry. A slight distortion of the momentum sphere was observed in the time-of-flight direction. The ions initial downwards velocity and the magnetic field both result in an off-center position of the ion cloud on the detector. Combined with the geometry of the electric field, acceleration is slightly changed for different distances from the spectrometer

[2]The atomic mass unit amu - with $1\,\text{amu} = 1.660\,54 \times 10^{-27}\,\text{kg}$ - is used throughout this work when referring to masses of particles.

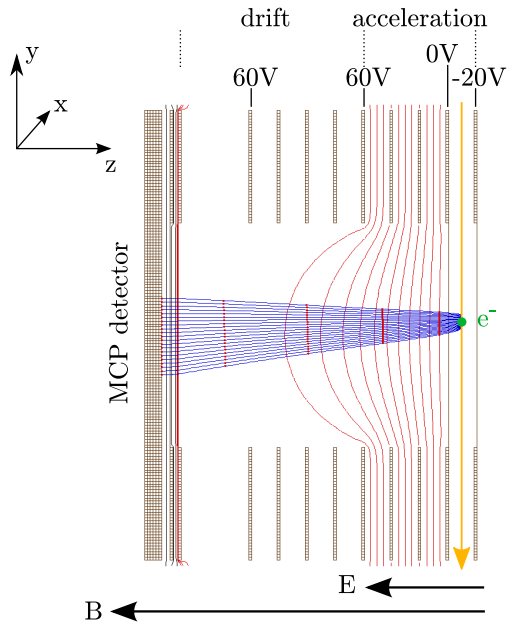

Figure 4.4: Simulation of the electric and magnetic field and the resulting ion flight paths inside the spectrometer of the Heidelberg DEA apparatus using the SIMION 8.1 software. Red and black lines show equipotential lines of the electric field, blue lines are exemplary flight paths for anions with a mass of 16 amu with different momenta in the vertical direction (y-direction). The green dot shows the direction of the electron beam through the depicted plane and the orange line shows the target gas jet direction.

axis. This leads to a minor dependence of the time-of-flight on the vertical position of the ion as can be seen in figure 4.4. There, the blue lines show ion flight paths and the red dots are time markers. The distortion is easily corrected for in the analysis by setting the time-of-flight for zero momentum in this direction depending on the vertical position.

4.2 The GASIC apparatus

Some of the dissociative electron attachment experiments were carried out using the GASIC setup at the Open University in Milton Keynes, United Kingdom. This apparatus is based on the design described by Nandi *et al.* [81] and therefore uses the same general measurement principle as the Heidelberg setup, but differences in the gas delivery and the data acquisition give it a different field of application. The setup is depicted in figure 4.5. In short, a pulsed electron beam is crossed with an effusive gas beam and any produced negative ions are pushed into a time-of-flight spectrometer and towards an MCP detector. The electron beam is created using a thermionic electron gun. A tungsten filament is heated by passing a current of 2.1 A through it and is set to a voltage corresponding to the required electron energy. The ejected electrons are extracted via the cathode aperture which is on a slightly positive potential compared to the filament and they are accelerated towards the anode at ground potential. The beam is pulsed at repetition rates ranging from 10 kHz to 30 kHz by applying a voltage pulse with a length of 200 ns to a grid in the path of the electrons between the cathode and anode, only allowing the electrons to pass during the pulse and blocking them otherwise. The electron beam is guided to the target by a magnetic field of up to 4 mT. After passing through the intersection region the electron beam is collected by a Faraday cup and the current measured by a pico-amperemeter.

The target molecules are delivered to the interaction region using an effusive gas beam. This beam is created by expanding the gas into the interaction region through a thin titanium capillary with an inner diameter of 0.02″ (0.5 mm), pointing out

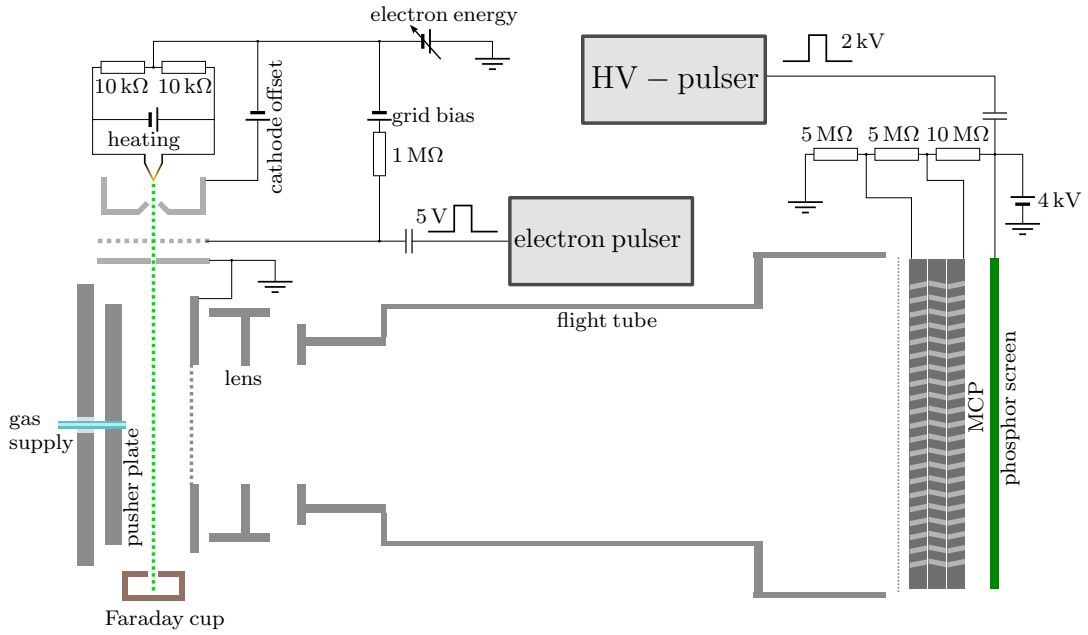

Figure 4.5: Schematic setup of the GASIC experiment.

of the pusher plate towards the time-of-flight spectrometer. The gas flow is controlled by a precision leak valve and the pressure in the chamber is kept around 1×10^{-6} mbar during operation of the gas beam.

400 ns after the electron pulse, the anions which are created in the collision with the gas target are accelerated towards the spectrometer by applying a voltage pulse to the pusher plate. The spectrometer consists of a focusing lens and the flight tube. The fields inside the spectrometer are shielded from the interaction region by a high transmission grid in front of the lens. The ions are then detected using an MCP and phosphor screen assembly.

The experiment can be used in two different acquisition modes. The first one is the ion counting mode. In this mode, the time-of-flight of each ion hitting the detector is measured in a similar way to the Heidelberg setup. The voltage drop on the back side of the detector is measured by capacitive coupling to a constant-fraction-discriminator. The time between the start of the electron pulse and the ion signal is converted to an analog voltage by a time-to-amplitude converter (TAC) and the voltage is read by a PC via an analog-to-digital converter (ADC). Measuring the time-of-flight distributions in this way allows an identification of the mass of the ions. Alternatively, in this mode a single-channel-analyzer output of the TAC can be used to select only events in a certain time-of-flight range and the resulting ion yield is measured while scanning the electron energy via a computer program. This way, the ion yield curves of a certain anion produced in the dissociative electron attachment as a function of impact energy can be determined. However, in this operating mode, no information about the angular distribution or the kinetic energy of the fragments is obtained.

The second acquisition mode of the experiment is the velocity slice imaging mode. In this mode, the phosphor screen located behind the MCP is set to 2 kV above the voltage of the MCP backside. The whole detector is set to a voltage below the normal operating voltage to be inactive. At a predetermined time, corresponding

to the time-of-flight of the investigated ion, a high voltage switch gives a 2 kV pulse to the MCP backside and phosphor screen, activating the detector for 100 ns. The ions arriving within this time-of-flight window are detected on the phosphor screen and imaged by a CCD camera. The images are stored on a PC and evaluated in post analysis. From those images, the positions of the ions on the detector are reconstructed and angular distributions as well as the kinetic energy of the investigated ion can be obtained.

Compared to the Heidelberg DEA apparatus, this setup has the important advantage that the target density in the effusive beam is at least one order of magnitude higher than in the supersonic gas jet [69]. This allows the investigation of reactions with a lower cross section than in the Heidelberg DEA setup. The effusive gas beam also has the advantage that the backing pressure can be far below atmospheric pressure, which allows the investigation of liquids without the necessity of a heated inlet system. However, the effusive beam is not cooled and collimated like a supersonic jet and the target will be only slightly below room temperature. This reduces the momentum resolution of the experiment compared to the Heidelberg apparatus. Additionally, the thermionic electron gun has a lower energy resolution (typically 0.8 eV) than the photoemission gun used in the Heidelberg apparatus (typically 0.2 eV) and the velocity slice imaging introduces restrictions to the measurement by only allowing the measurement of one fragment at a time. The repetition rate is also restricted to 10 kHz in the velocity slice imaging mode, which is limited by the high voltage pulser responsible for the activation of the detector. As a result, the velocity slice imaging technique is useful when cross sections are high and therefore the number of recorded events is high. In that case the ability of the phosphor screen and CCD camera detection system to detect many events in one picture is advantageous. For low count rates on the other hand, the higher efficiency and higher possible repetition rate when using a delay-line detector like the one used in the Heidelberg apparatus is the better choice. However, even with those restrictions in the GASIC apparatus, the accessibility of reactions with low cross sections outweighs its disadvantages.

Momentum reconstruction in the GASIC apparatus

The different acceleration fields in the VSI spectrometer, especially the focusing lens inside the acceleration region impede the calculation of momenta from the detection position. Therefore, no effort was taken to calculate the detection position of ions as a function of their momentum. Instead, the well known momentum distribution of DEA in oxygen has been used to translate the detector image into momentum. When the instrument is running in imaging mode, information about the momentum in the direction normal to the detector plane (the time-of-flight direction) is not accessible and not needed since the obtained time-of-flight-slice contains information about all scattering angles.

The time-of-flight mode on the other hand is used to identify of the fragment masses and therefore the flight times of fragments with different masses need to be known. The time-of-flight has been determined by modeling the spectrometer in the SIMION program, which is depicted in figure 4.6. The obtained times-of-flight in the simulation were checked against experimental observations of known peaks such as O^-/O_2 and F^- and Cl^- from 1,2-dichlorotetrafluoroethane, showing excellent agreement

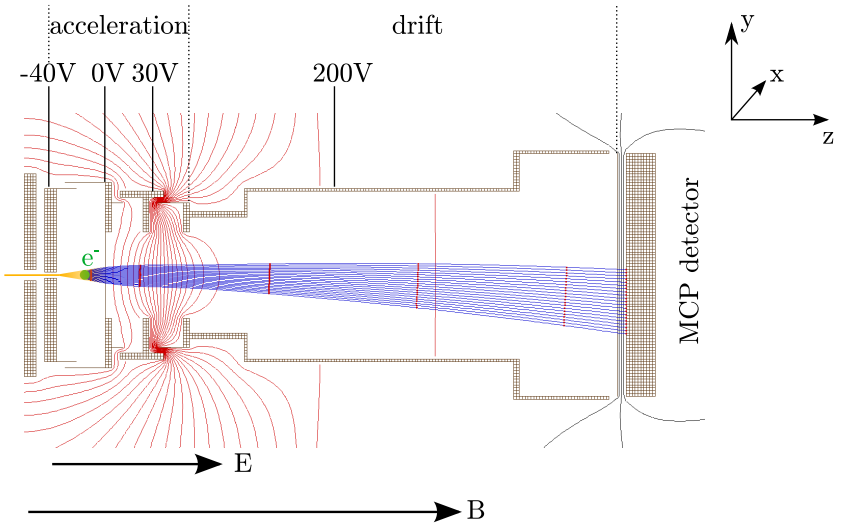

Figure 4.6: Simulation of the electric and magnetic field and the resulting ion flight paths inside the GASIC VSI spectrometer using the SIMION 8.1 software. Red and black lines show equipotential lines, blue lines are exemplary flight paths for anions with a mass of 16 amu with different momenta in the vertical direction. The green dot shows the path of the projectile electrons perpendicular to the depicted plane and the orange line shows the effusive gas beam. The indicated voltages are the ones used in this simulation but they are changed as needed, depending on the investigated fragment.

between simulation and experiment. This enabled the identification of unknown fragments by comparison of experimental time-of-flight peaks to the time-of-flight obtained in the simulation for different masses. Additionally the simulation was used to confirm the linear relationship between detector position and momentum which is necessary to calculate the momenta from the position information.

4.3 Momentum reconstruction using Abel inversion

In the electron impact excitation experiment the momentum resolution in the direction along the gas jet - which is normal to the detector plane - is low due to the large initial momentum spread in this direction. In the dissociative electron attachment experiments, momentum resolution in the time-of-flight direction can also be low when the experiment is operated in the high mass resolution mode, which is described in the beginning of this chapter. In this mode, the extraction field is chosen so as to compress the time-of-flight spread created by the initial momentum of the fragment and to create sharper peaks in the time-of-flight spectrum. The information about the momentum in this direction - which is usually obtained from the time-of-flight of a fragment - is then lost.

Due to the symmetry of the problem, namely a rotational symmetry around the electron impact direction, all information about the scattering is contained in any plane which contains this symmetry axis. The detector planes in the both the electron impact excitation experiment and the dissociative electron attachment experiment fulfill this condition. Using an inverse Abel transformation, the angular distribution

in the detector plane is reconstructed from the projection of all momenta into this plane (cf. figure 4.7(a)). This will be described in the following.

Figure 4.7(a) shows the momentum distribution (blue) in two planes: the gray plane containing the electron impact direction (shown in red) and a plane perpendicular to the electron impact direction. We want to reconstruct the distribution in the gray x-y-plane. The momentum distribution is rotationally symmetric around the x-axis. Therefore, any cut through the y-z-plane (e.g. the white plane in figure 4.7(a)) contains a momentum distribution which only depends on the radius: $f(y,z) = f(r)$, with $r = \sqrt{y^2+z^2}$.

We start out with this function $f(r)$ describing the 2-dimensional symmetric distribution as shown in blue in figure 4.7(b). The Abel transformation then is obtained as the projection of the distribution on one of the Cartesian coordinates, here we use the y-coordinate:

$$h(y) = 2\int_y^R f(r)\,\frac{r}{\sqrt{r^2-y^2}}\mathrm{d}r\,. \tag{4.3}$$

The direction of projection is illustrated in figure 4.7(b) by the thick black arrows. Along those arrows, the distribution is integrated and assigned to $h(y)$. Here, R is the maximum value of r for which $f(r) \neq 0$. As can be seen from eq. (4.3), if there is no maximum value, i.e. $R \to \infty$ then $f(r)$ must approach zero faster than $1/r$ for the integral not to diverge. In the experiment a maximum value R for which $f(r) \neq 0$ exists because there is a maximum momentum which the detected fragment can have, depending on the available excess energy of the reaction. A function $f(r)$ exists for any slice of the momentum sphere in a plane perpendicular to the axis of rotational symmetry, i.e. perpendicular to the electron impact direction.

Eq. (4.3) can be inverted to give the original function from the projection:

$$f(r) = -\frac{1}{\pi}\int_r^R \frac{\mathrm{d}h(y)}{\mathrm{d}y}\,\frac{1}{\sqrt{y^2-r^2}}\mathrm{d}y\,. \tag{4.4}$$

In the analysis of experimental data, a MATLAB implementation [61] of the numerical method for Abel inversion developed by G. Pretzler [96] was used. The method will be explained in short. The original function $f(r)$ is expanded into the series

$$f(r) = \sum_{n=N_l}^{N_u} A_n f_n(r) \tag{4.5}$$

where A_n are amplitudes and $f_n(r)$ is chosen as the following set of cosine functions:

$$f_0 = 1,\ f_n(r) = 1-(-1)^n\cos\left(n\pi\frac{r}{R}\right)\,. \tag{4.6}$$

This allows a good representation of arbitrary functions while also simplifying the calculations of the integrals and derivatives. N_u and N_l are an upper and lower

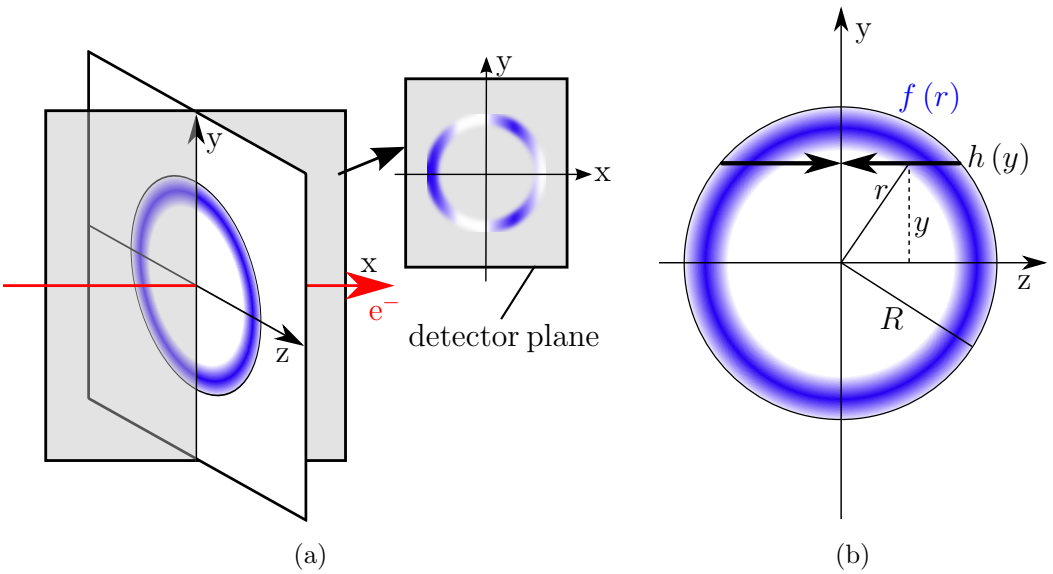

Figure 4.7: (a) Sketch of the application of the Abel transformation in the analysis of the experiment. The transformation is performed in the white plane and any plane parallel to it. These planes are normal to the electron impact direction (red arrow) as well as to the detector plane (gray plane). The momentum distribution in the gray plane is reconstructed from the projection of all momenta into it. (b) The radially symmetric function $f(r)$ and the forward Abel transformation $h(y)$, containing the integral of all values along the thick black arrow. The original function $f(r)$ has values differing from zero only for $r < R$, allowing the restriction of all calculations to within this range. Figure (b) adopted from [96].

frequency limit, respectively. These can be used as a noise filter. Using eq. (4.5) as the original function, the projection becomes

$$H(y) = 2 \sum_{n=N_l}^{N_u} A_n \int_r^R f_n(r) \frac{r}{\sqrt{r^2 - y^2}} \mathrm{d}r \,. \tag{4.7}$$

The value of the integral is calculated numerically and the resulting function is fitted to the measured projection, yielding the values of A_n and allowing the calculation of the original distribution by inserting the obtained A_n into equation (4.5).

For the analysis of the experimental data the 2-dimensional momentum image of the ions or atoms will be created by projecting all momenta into the desired plane. In figure 4.7(a) this is the gray x-y-plane. The Abel inversion is then performed for every slice of the image perpendicular to the electron impact direction. This corresponds to the cut between the gray and the white plane in figure 4.7(a). The original momentum distribution in the white plane is obtained for every slice.

5. Results - electronic excitation of metastable states

We developed a new experimental technique for momentum imaging of inelastically scattered electrons. The method relies on the recoil momentum resolved detection of atoms which have been excited into metastable states by the electron-atom collision. High excitation energies are favorable in this experiment because their detection efficiency on the microchannel plate detector is high. Furthermore, for good momentum resolution light atoms are preferable. For these reasons we used helium and neon for the first measurements with this new setup. The experimental apparatus is described in detail in section 3.1.

5.1 Electronic excitation in helium

The energy dependence of the total metastable yield from electron impact in helium has been investigated with very high energy resolution by Brunt *et al.* [19] and was also obtained in *ab initio* calculations by Bartschat [8]. The calculations showed excellent agreement with the experiments and were used for calibration of the electron impact energy and determination of the energy resolution in our experiments. In a first step, the energy dependence of the metastable yield was measured in the threshold region between 19 eV and 22 eV. In this region, the $n = 2$ states are populated and the rise of the cross sections for excitation of different states just above their threshold results in a rich structure in the yield curve. This is used to compare the experimental helium yield curve to literature data and theory.

The obtained excitation yield curve is shown in figure 5.1 and compared to the theoretical calculations of Bartschat. The lifetimes of the states of interest are listed in table 5.1 and should be compared to the experimental time-of-flight of the helium atoms which is around 55 µs. The $2\,^3\mathrm{P}$ state decays on a time-scale much shorter than the time-of-flight but its decay is dominated by the $2\,^3\mathrm{P} \rightarrow 2\,^3\mathrm{S}$ transition. Atoms which are created in the $2\,^3\mathrm{P}$ state can thus still be detected because the state they decay into has a high internal energy and a long lifetime. The $2\,^1\mathrm{P}$ state on the other hand has a lifetime much shorter than the experimental time-of-flight

Table 5.1: Excitation energies E_{exc} (from [105]) and lifetimes τ for the singly excited states in the helium atom which are energetically accessible in the considered energy range up to 22.2 eV.

state	short name	E_{exc}	τ with reference
He* (1s2s ^{3}S)	2 ^{3}S	19.820 eV	≈4000 s (→ 1 ^{1}S) [78]
He* (1s2s ^{1}S)	2 ^{1}S	20.616 eV	20 ms (→ 1 ^{1}S) [124]
He* (1s2p ^{3}P)	2 ^{3}P	20.964 eV	≈100 ns (→ 2 ^{3}S) [19]
He* (1s2p ^{1}P)	2 ^{1}P	21.218 eV	0.5 ns (→ 1 ^{1}S) [105]

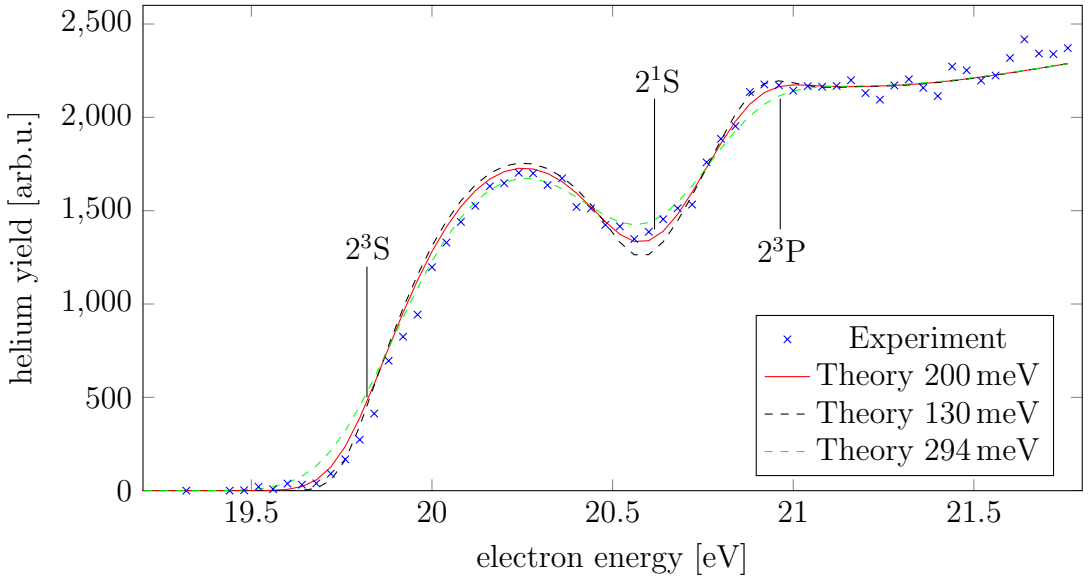

Figure 5.1: Comparison of measured total helium metastable yield (blue crosses) with theoretical cross section after convolution with an impact energy spread with a FWHM of 200 meV (solid red line). Two other expected yield curves for different energy spreads are shown for comparison (dashed lines). This measurement is used to determine the experimental energy spread of the electron beam. The electron current during firing of the electron gun was around 5 µA during this measurement.

and its main transition leads to the ground state (1 ^{1}S). It will therefore not be detected and its contribution is ignored in the theoretically expected cross section.

Electron impact excitation cross sections for a particular excited state always consist of a sharp onset at the threshold energy for excitation and a fast rise of the cross section. The characteristics of the cross section at higher energies depend on the process. In the investigated case, several of the excited states are triplet states which can only be reached by exchange of the projectile electron with a bound electron. This process requires a capture of the projectile and is only efficient in a narrow energy range of a few eV above the threshold energy. These excitation processes exhibit a maximum of the cross section close to the threshold energy and a fast drop of the cross section for higher impact energies. Excitation of singlet states shows a high cross section over a much broader range of energies because no electron capture is necessary. The resulting experimental total yield curve shown in figure 5.1 thus shows a fast rise at the threshold for 2 ^{3}S excitation followed by a peak in the cross section for excitation of the 2 ^{3}S state and a minimum in the yield curve just at the threshold for excitation of the 2 ^{1}S state. This rich structure in the yield curve is

very sensitive to the electron energy resolution. In order to extract the experimental energy resolution of the projectile electrons, the expected yield curve provided by theoretical calculations has been convoluted with Gaussian distributions in electron energy and compared to the experimental yield curve. Excellent agreement can be found when an energy spread of 200 meV FWHM is assumed for the electron beam. Figure 5.1 also shows the expected yield curve for different energy resolutions. Sharp features like the onset at 19.82 eV or the dip prior to the onset of $2\,^1$S excitation clearly show the influence of the energy spread.

This measurement also represents the commissioning of this GaAs photoemission electron gun in an experiment and its performance clearly is superior to that of conventional thermionic electron guns for which the usual energy spread is around 0.5 eV - 0.8 eV at comparable currents. The photoemission electron gun is crucial to allow the investigation of energy sensitive properties like the angular distribution of scattered electrons which can change drastically within less than 0.5 eV in the investigated low energy region.

The additional time and position information of the MCP detector is used to measure the momentum change of the excited helium atoms. This information is used to calculate the scattering angle of the projectile electron as well as the energy loss of the projectile electron which allows the determination of the state which has been populated in the collision.

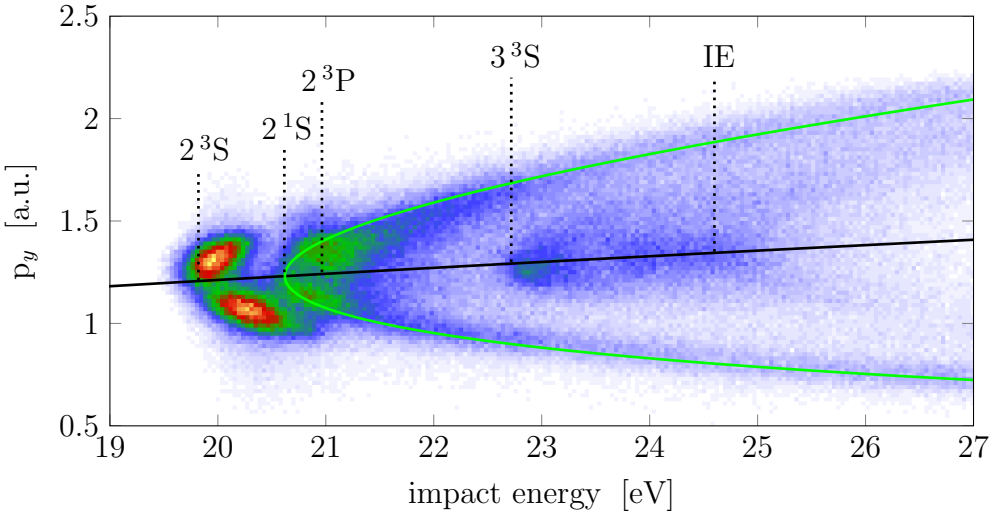

Figure 5.2: Momentum distribution of atoms in excited states for scattering along the impact direction (y-axis) by restricting the momentum in x-direction (transverse momentum) to ±0.1 a.u. The black line shows the momentum of the incident electron. Due to conservation of energy all events that correspond to excitation of the same electronic state lie on one parabola as shown exemplary for the $2\,^1$S state by the green line.

While in the total yield in figure 5.1 the contributions of the different electronically excited states are superimposed, momentum resolved measurements give a clearer picture and are able to separate different states by the momentum transfer to the helium atom. This is made visible in figure 5.2, showing the momentum of the atoms in excited states in the direction of the electron impact. For this picture, only the yield for events with low momentum transfer perpendicular to the electron impact

direction (<0.1 a.u.) are considered which corresponds to scattering in the forward and backward direction. This representation will obviously not give the full picture, but it is well suited to distinguish different states and still recognize features like forward/backward asymmetry in the scattering. In figure 5.2, the black line shows the momentum carried by the incident electron. When helium atoms are observed with the same momentum as the projectile, the electron must have transferred all its momentum to the helium. This means that events close to the projectile momentum must be at the energy threshold for excitation of a particular state. This can be seen in figure 5.2 at impact energies around 19.8 eV, 20.6 eV and 22.7 eV, corresponding to excitation of the $2\,^3$S, $2\,^1$S and $3\,^3$S state, respectively. The threshold energies for excitation of several states as well as the ionization threshold (IE) are marked in the figure. Events with higher momentum than the initial momentum of the projectile electron correspond to backwards scattering because the atom received more forward momentum than was carried by the electron and events below the initial projectile momentum correspond to forward scattering of the electron. All events that correspond to excitation of the same state lie on a parabola like the one shown as the green line for the $2\,^1$S state. In general the equation

$$E_{exc} = E_e - \frac{|\mathbf{p}_{He} - \mathbf{p}_e|^2}{2m_e} \tag{5.1}$$

must be fulfilled where E_{exc} is the excitation energy, E_e is the projectile electron energy and $\mathbf{p}_{He}$ and $\mathbf{p}_e$ are the momentum of the helium obtained from the electron and the momentum of the incident electron before scattering. The $2\,^1$S state is the only singlet state investigated in this experiment and is best suited to show this behavior because its cross section is high over the whole investigated impact energy range since it does not rely on an exchange mechanism. The triplet states which are excited are seen e.g. in the first two maxima at around 20 eV which correspond to the $2\,^3$S state. At 23 eV, the onset of excitation to several $n = 3$ states can be seen close to the black electron momentum line. At higher energy up to the ionization energy (IE) at 24.56 eV, excitation of many higher lying states which are indistinguishable in this experiment can be seen.

The experiment also gives information about properties of the supersonic gas jet. When measuring the time-of-flight distribution at the threshold energy of 19.8 eV, it is dominated by the initial distribution of velocities along the jet axis. From the time-of-flight distribution we can estimate the longitudinal temperature (i.e. the temperature along the jet direction) using

$$\bar{E} = \frac{m}{2}\bar{v}^2 = \frac{1}{2}k_B T. \tag{5.2}$$

The velocity spread $\bar{v}$ around the mean velocity of the gas jet is $110\,\mathrm{m\,s^{-1}}$, which yields a temperature of 3 K in the direction of the jet axis. The measured distribution of atom velocities in the direction of the supersonic jet is shown in figure 5.3. In this direction the gas is only cooled by the adiabatic expansion from the high pressure reservoir to the vacuum. Perpendicular to the jet axis, the velocity spread is reduced further when the jet is collimated by the skimmers and the aperture. These reject atoms which have a high velocity in the plane perpendicular to the jet axis and

leave only slow atoms in the jet, thereby lowering its temperature. It also means that the momentum distributions are not isotropic. The momentum spread in the plane perpendicular to the jet direction usually is an order of magnitude lower than along the jet direction. The calculated temperature is required to model the expected momentum images in simulations of the experiment. The temperature perpendicular to the jet direction was too low to be measured since the experimental momentum resolution was restricted by the finite size of the interaction region.

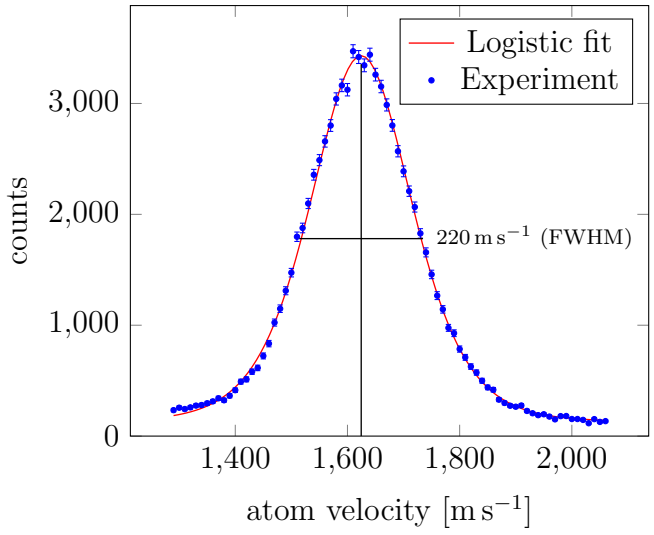

Figure 5.3: Velocity distribution of the supersonic gas jet in the direction of flow. From the velocity spread, a gas temperature of 3 K in the direction of the gas flow can be estimated.

Angular distributions are investigated using the created momentum images from time-of-flight and position on the detector as described in section 3.5. Due to the velocity spread in z-direction it is not possible to reconstruct the momentum component p_z with the same precision as the other directions. Instead, either a time-of-flight slice corresponding to a velocity of $\pm 50\,\mathrm{m\,s^{-1}}$ around the mean jet velocity is used to suppress the influence of out-of-plane scattering or only the momenta perpendicular to the jet direction are measured. In the latter case, all momenta are projected onto the detector plane, and an Abel inversion is performed to reconstruct the 3D-distribution (cf. chapter 4.3). In both cases the obtained momentum images are compared to simulations using cross sections from different theoretical calculations. An example of the resulting experimental momentum images at an impact energy of 22.2 eV can be seen in figure 5.4 along with the results of the corresponding simulations. Both methods of reconstructing the original momentum images (time-of-flight slice in figure 5.4(a) and Abel inversion in figure 5.4(c)) yield excellent results when comparing to the simulations. The Abel inversion in general is better suited to separate different states because the broadening influence of the momentum uncertainty in the time-of-flight direction is completely compensated but numerical uncertainties lead to intensity artifacts for low absolute transverse momenta.

In figure 5.4 the excitation of the $2\,^3\mathrm{S}$ state is responsible for the outermost features and is clearly separated from the events due to excitation of the higher states. The $2\,^1\mathrm{S}$ and $2\,^3\mathrm{P}$ states however are only separated by a difference in excitation energy of 350 meV and in this experiment it is not possible to separate them. The simulations show that both the energy resolution of the electron beam and the size of the interaction volume are responsible for limiting the resolution and only improving both by about a factor of at least three would make the $2\,^1\mathrm{S}$ and $2\,^3\mathrm{P}$

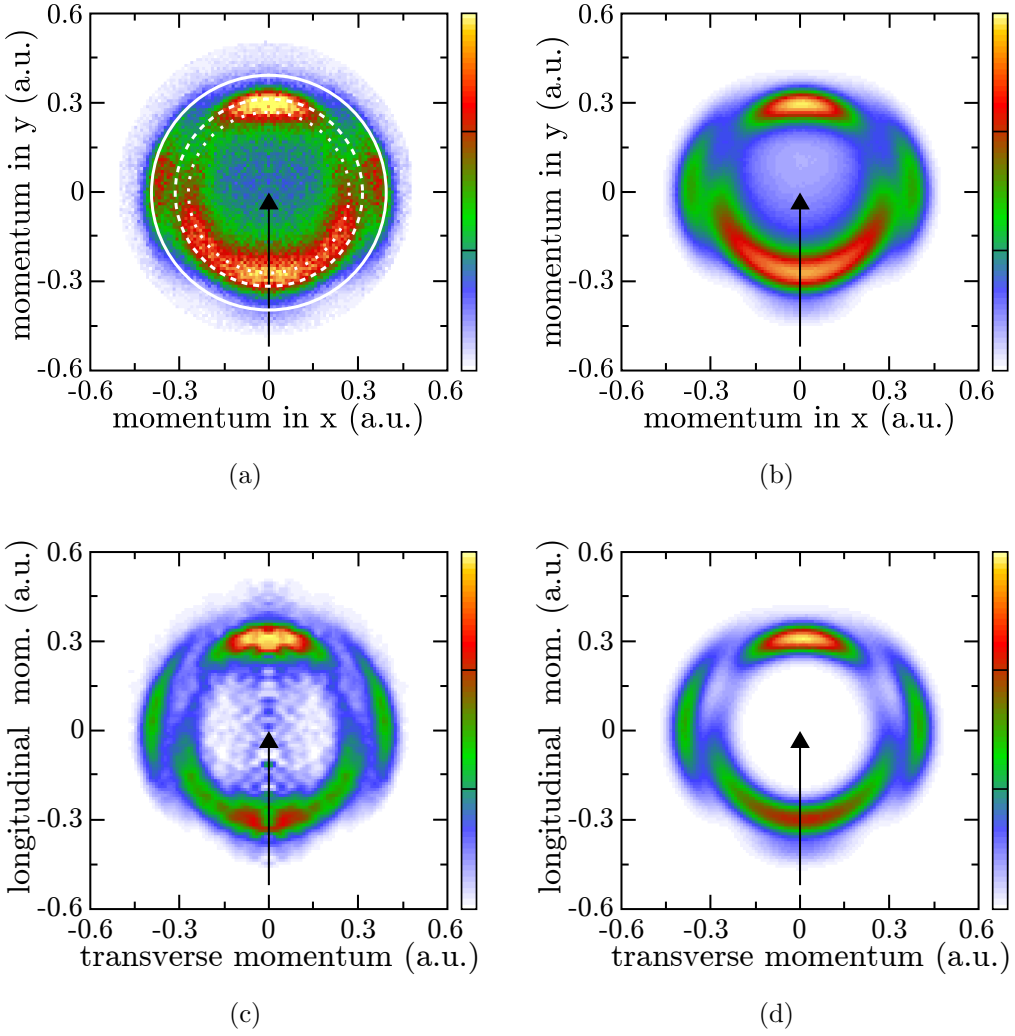

Figure 5.4: Momentum images for electron impact excitation of helium atoms at a projectile impact energy of 22.2 eV. The projectile direction is indicated by the black arrow. (a) shows the momentum image for a time-of-flight slice of $\pm 50\,\mathrm{m\,s^{-1}}$ around the mean velocity in z-direction as recorded in the experiment. White circles are the expected momenta for the $2\,^3$S state (solid), $2\,^1$S state (dashed) and $2\,^3$P state (dotted). (b) shows the expected momentum image when simulating the experiment using differential cross sections from RMPS calculations. (c) shows the Abel inversion of the projection of all momenta into the detector plane and (d) shows the expected momenta using the RMPS data when restricting scattering to a plane. Excellent agreement between (a) and (b) as well as between (c) and (d) is visible.

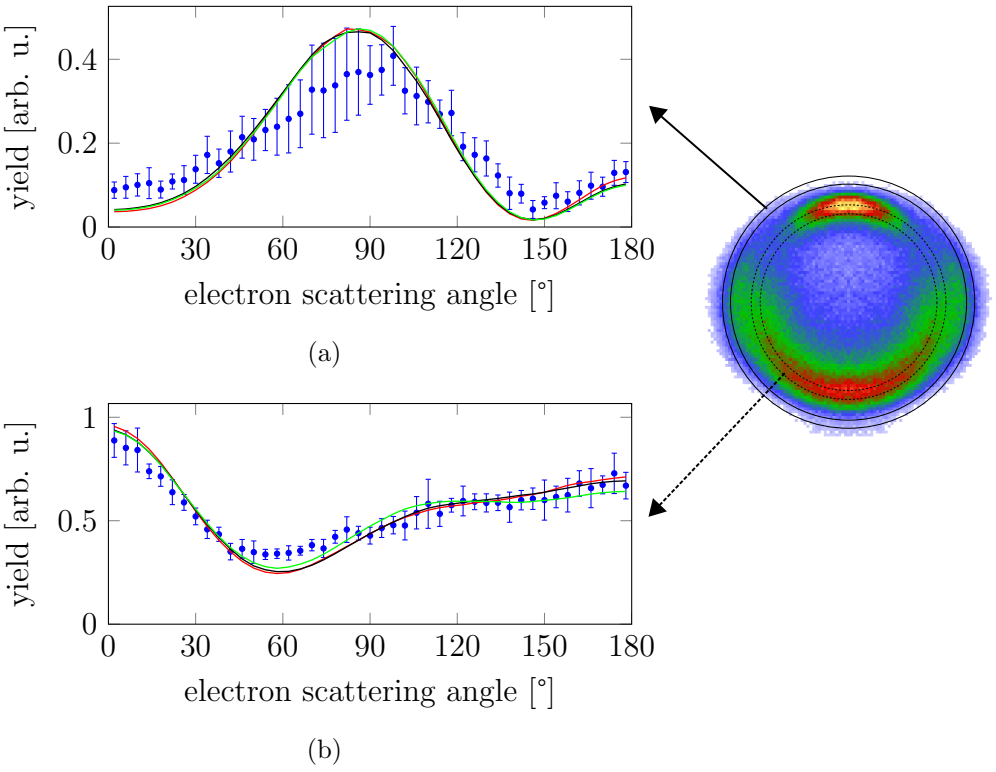

Figure 5.5: Electron scattering angle distributions as measured in the experiment are compared to the simulation for electron impact excitation of helium at an impact energy of $E_e = 22.2\,\text{eV}$. The plots are restricted to events from helium atoms with certain total momenta, corresponding to a specific energy loss of the electron. In (a) the momentum is set to $0.42\,\text{a.u.} \pm 0.015\,\text{a.u.}$, corresponding to an energy loss of 19.8 eV and therefore excitation of the $2\,^3\text{S}$ state. In (b) the momentum is $0.32\,\text{a.u.} \pm 0.015\,\text{a.u.}$ and the corresponding energy loss of 20.8 eV includes contributions from excitation of both $2\,^1\text{S}$ and $2\,^3\text{P}$ states. Blue circles are experimental values, red lines show RMPS calculations, black lines show BSR calculations and green lines show CCC calculations.

state separately accessible. This was beyond the ability of the current setup but is in principle possible in this type of experiment.

Instead of scattering angle distributions for particular states, distributions for different measured electron momentum intervals are used to separate the states as well as possible. The comparison to theory is again done using the simulations which show the expected distribution in the experiment using theoretical cross sections. In the simulation the same "apparent" momentum range of the scattered electron is selected as in the experiment. The results of this analysis are shown in figure 5.5 and excellent agreement between all three theories and our experimental results can clearly be seen. One visible difference between experiment and theory is observed for scattering angles with low yield where in the experiment a higher yield is observed. This can be attributed to a low constant background of false events in the experiments which is also visible in the outer part of the momentum image in figure 5.4(a). The background events are most likely produced by metastable states excited in background helium gas in the experimental chamber because the gas jet could not be dumped in an extra chamber. Those events are expected to create a constant background - as it is observed in the experiment - due to their large momentum and spatial spread.

Although all three theories give very similar angular distributions, the CCC (convergent close-coupling) calculations show a somewhat different distribution for the low excess energy in figure 5.5(b) which corresponds to the $2\,^1S$ and $2\,^3P$ states. It shows a higher yield in the region around 100°, creating a broad maximum which is almost invisible in the RMPS (R-matrix with pseudo-states) and the BSR (B-spline R-matrix) calculations. The results of RMPS and BSR calculations are in better agreement with the experimental results than the CCC calculations, which seem to slightly overestimate the broad peak around 100°. The CCC calculations also predict a lower helium yield at 180° than both our experiment and the other theories for the $2\,^1S$ and $2\,^3P$ states. Overall the R-matrix calculations (RMPS and BSR) give a slightly better agreement with our measured angular distributions than the convergent close-coupling calculations.

5.2 Electronic excitation in neon

The technique of detecting the deflection angle of excited atoms works best for light targets where the deflection and therefore the momentum resolution is highest. Nonetheless, measuring angular distributions for neon (mass: 20 amu) is well within the accessible range. This can be seen in a momentum image for electronic excitation of neon at an impact energy of 19.4 eV in figure 5.6(a). At this energy, four different $2p^5 3s$ states ($^1P_1$, $^3P_0$, $^3P_1$, $^3P_2$) with excitation energies in the range of 16.62 eV to 16.85 eV can be excited [18]. Additionally, 10 different $2p^5 3p$ states exist in the energy range from 18.38 eV to 18.97 eV, of which seven are triplet states with long lifetimes. The momentum ranges corresponding to both groups of transitions are shown in figure 5.6(b). Out of the four $2p^5 3s$ states where the momentum transfer is high enough to observe angular distributions, the $^1P_1$ state can decay to the ground state in a 2-photon decay and is therefore expected to be not visible in this experiment. Although these states are too close in energy to be observed separately, the angular distribution of the sum of all three ^3P states can be investigated and compared to theory.

Allen *et al.* calculated the cross sections for excitation of the ^3P states relevant in our experiment at several scattering angles [3]. The comparison of the angular distributions obtained in our setup - using the Abel inversion - with the theoretical calculations is depicted in figure 5.6(c). It shows generally a very similar distribution. The main scattering peak is observed in forward direction and a smaller peak exists for backward scattering. However, clear differences arise for scattering angles close to 0° and 180°. In our experiment, the broad forward peak has its highest yield at 30° and the yield drops towards lower scattering angles while the theoretical calculations show an increase towards 0°. For the backwards scattering peak we measure a higher intensity than expected from theory. Other experiments show excellent agreement with the theory even at the angles where our results differ [3]. It is therefore prudent to check for possible errors in this new type of experiment. As was shown for the electronic excitation of helium, the apparatus is able to generate accurate momentum images which are in agreement with theory. The most likely step to introduce errors is the Abel inversion. Already for helium we recognized that for transverse momenta close to zero, the method is imprecise and scattering angles around 0° and 180° fall into this part of the momentum image. Comparing the original 2-dimensional projection of the momentum distribution shown in figure 5.6(a) to

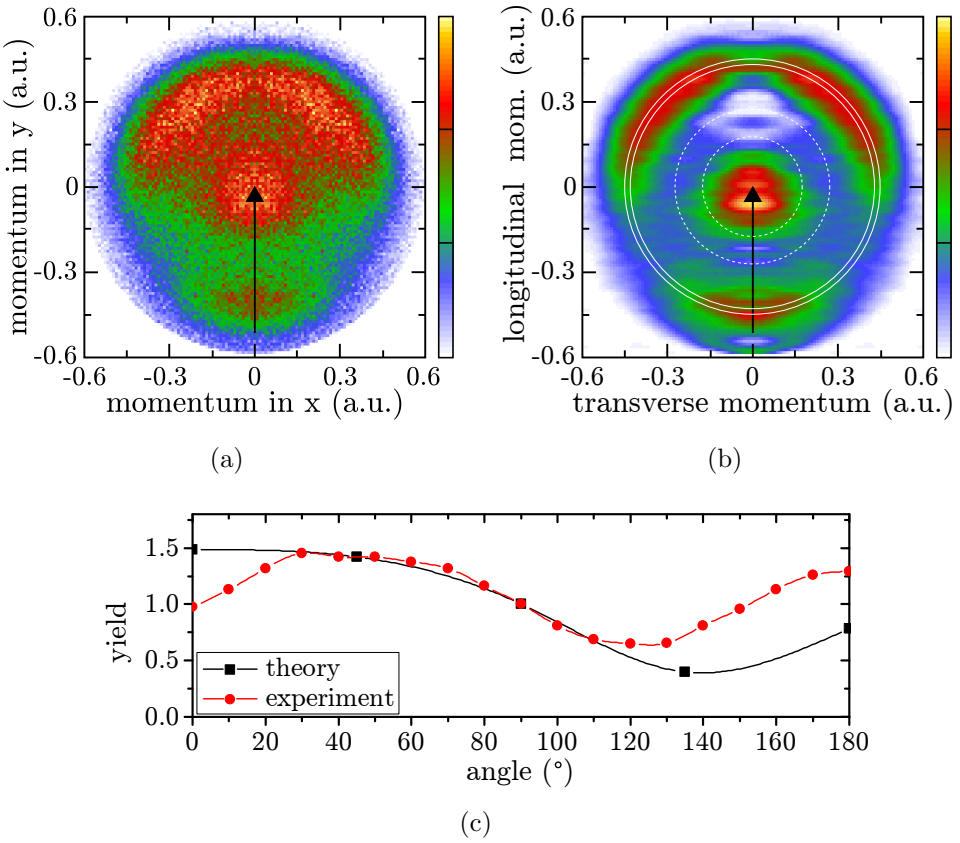

Figure 5.6: (a) Measured projection of the electron momentum distribution for electron impact excitation of neon at an impact energy of 19.4 eV. (b) Reconstruction of the 3D-electron scattering distribution $\sigma\,(p_{\mathrm{long}}, p_{\mathrm{trans}})$ from (a) using the Abel inversion. Solid white circles mark the momentum range for population of the 3s-orbital, the dashed circles mark the momentum range for population of the 3p-orbital. (c) Comparison of the experimental and calculated scattering angle distribution for excitation of the ^{3}P states of M. Allen *et al.* [3]. Both distributions have been normalized to the yield at 90°. Lines connecting data points are a guide to the eye.

the Abel inversion in figure 5.6(b) illustrates this behavior. For backward electron scattering[1], the narrow peak in the projection is broadened in the Abel inversion, which overestimates the width of the peak around 180°. The decrease in metastable yield for forward electron scattering[2] compared to the maximum at 30° however is visible even in the projection and cannot be due to errors induced by the Abel inversion. Instead, the results suggest that the forward scattering minimum is a feature of the differential cross section which is not reproduced by the theoretical calculations. Further investigations should be undertaken to resolve this discrepancy between theory and experiment.

Figure 5.6(b) also shows that there are almost no events in the momentum range in which excitation of the neon atom leading to population of the 3p-orbital is expected. The calculated excitation cross sections by Allan *et al.* [3] for population of the 3p-orbital are lower than the cross section for population of the 3s-orbital. In the shown experiment they are thus indistinguishable from background. Instead, a

[1] around a longitudinal momentum of −0.4 a.u. and a transverse momentum of 0 a.u.
[2] around a longitudinal momentum of +0.4 a.u. and a transverse momentum of 0 a.u.

peak around zero momentum is observed which corresponds to higher energy loss of the projectile electron. This low energy peak can only be created by population of the 4s-orbital in neon. Excitation to the corresponding states has threshold energies ranging from 19.66 eV to 19.78 eV [3]. At an electron impact energy of 19.4 eV in the experiment, those states are accessible for some projectiles due to the energy resolution of the electron beam of 200 meV (FWHM).

Overall, we could show that our newly developed experimental design is very well suited for investigating electron impact excitation of metastable states. In helium we obtained excellent agreement for the angular distributions of inelastically scattered electrons between our experiment and different theories. In neon, the agreement with theory was good as well, but some differences between experiment and theory were observed. Measuring electron scattering angles around 0° and 180° is a challenge to many other experiments which could be overcome in this design.

6. Results - dissociative electron attachment

In this chapter, the dissociative electron attachment measurements are evaluated. The chapter starts with a description of the calibration measurements which were used to calibrate both the projectile energy scale and the fragment momentum scale. Afterwards, the different investigated molecules and molecular clusters are discussed.

6.1 Calibration measurements

The calculation of the fragment momentum from its recorded time-of-flight and impact position has been described in section 4. These calculations already mention several corrections which are necessary to model details of the setup and which require a calibration measurement. Additionally, the projectile impact energy must be known very precisely. Therefore, the two properties which are recorded in the experiments - namely the projectile electron impact energy and the fragment momentum - have to be calibrated before any useful measurements can be performed. We chose to use the well established negative ion production in sulfur hexafluoride and oxygen for this purpose. The Heidelberg DEA setup has been calibrated using both calibration measurements. SF_6^- production by electron attachment to SF_6 is used for calibration of the electron impact energy and measurement of the electron beam energy resolution. O^- production from O_2 by dissociative electron attachment is used for calibration of the electron impact energy as well, and additionally for the calibration of the momentum of the anionic fragment. The energy calibration shows the offset between the voltage which is applied to the cathode and the energy of the electrons created at the cathode. This difference is due to contact potentials between different metals in the connection of the cathode to its power supply, lowering the voltage of the cathode. The momentum calibration shows the influence of the field geometry on the flight paths. While we created a working simulation of the spectrometer, uncertainties in the exact position of the interaction region and possible small deviations between experiment and simulation mean that the simulation can only be precise after it has been adjusted to recreate the calibration measurements. In the GASIC setup, the calibration was performed using the O^-/O_2 resonance only.

SF_6^-/SF_6 calibration

Several past investigations showed that sulfur hexafluoride (SF_6) exhibits a sharp electron attachment resonance at an impact energy of 0 eV [26, 35]. This can be used to calibrate the electron beam energy by scanning the energy around 0 eV. The physical peak width of this electron attachment resonance is much lower than the energy spread of the electron beam and can therefore be used to estimate the energy resolution as well as calibrating the 0 eV position. Measurements were carried out in the Heidelberg apparatus using the tantalum photo-cathode and yielded energy resolutions between 280 meV and 370 meV FWHM after optimizing the voltages on the einzel lenses. A constant energy offset of the electron beam compared to the cathode voltage of −200 meV was measured in several calibration runs.

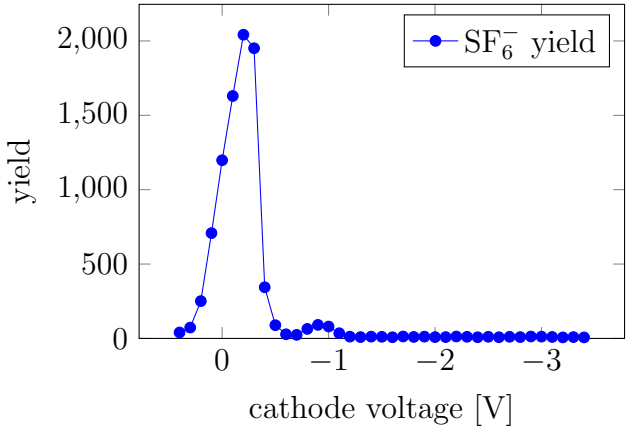

Figure 6.1: SF_6^- yield from electron impact in SF_6. The measurement is used for calibration of the projectile electron energy and for measurement of the projectile electron energy resolution. The electron beam energy resolution is estimated from the sharpness of the peak at the side with higher negative cathode voltage, since the width on the other side is influenced by space charge effects.

Figure 6.1 shows the experimental SF_6^- yield as a function of the cathode voltage. The peak is asymmetric with a lower width on the high energy side, i.e. the side with negative cathode voltage, than on the low energy side. The low energy side includes positive cathode voltages for which electrons should not be able to escape the cathode region. This leads to high space charges at the cathode and to a corresponding broadening of the energy spread of the electrons, allowing some of them to escape from the electron gun towards the interaction region. The width on this side of the peak overestimates the energy spread in the electron beam because space charge effects are much lower for negative cathode voltages where the electrons are immediately repelled by the cathode and guided towards the interaction region. The much lower width of the peak on the high energy side shows the realistic energy spread of the electron beam.

For the GaAs-photoemission electron source no energy calibration using SF_6 was performed since the observed yield curves for electron impact excitation in helium was used to obtain both impact energy and energy resolution of the projectile beam. This measurement has already been discussed in section 5.1.

O^-/O_2 calibration

Dissociation of a diatomic molecule is very well suited for quantitative calibration of the momentum measurement as well as the projectile energy. The energy of the anion at a certain projectile energy can be calculated if the bond dissociation energy of the molecule and the electron affinity of the atom which retains the electron are known. For oxygen, the bond dissociation energy $E_{bind} = 5.116\,\text{eV}$ [63] and

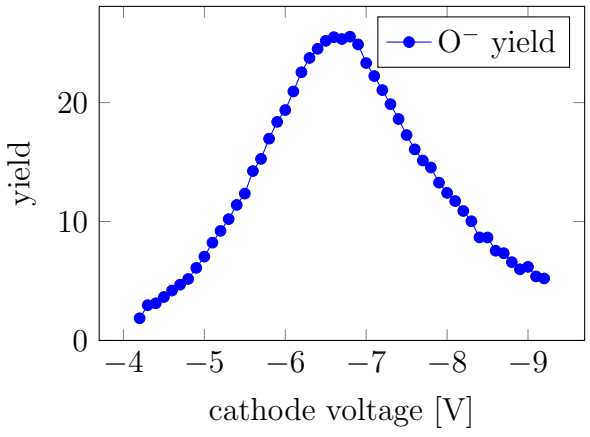

Figure 6.2: O^- yield for electron energy calibration. The remaining yield at the highest energy is due to background events. The maximum is expected at an electron energy of 6.5 eV which here corresponds to a cathode voltage of −6.7 V.

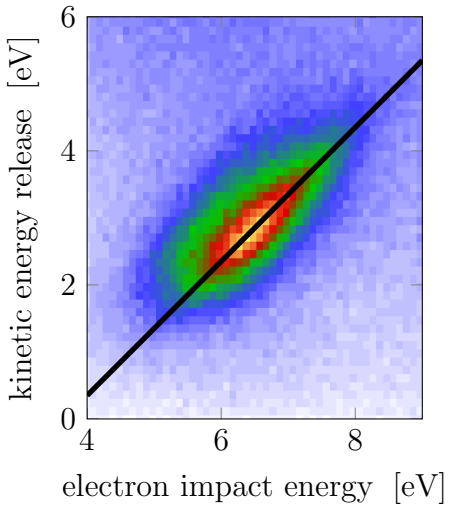

Figure 6.3: Kinetic energy release distribution of O^- from dissociative electron attachment to oxygen as a function of electron impact energy after calibration of the measured momenta. The black line shows the expected kinetic energy release according to eq. (2.1) where $E_{bind} = 5.116\,\text{eV}$ [63] and $EA = 1.465\,\text{eV}$ [15].

the electron affinity $EA = 1.465\,\text{eV}$ [15] have been well established which allows a quantitative calibration according to equation (2.1).

The oxygen molecule exhibits a well known broad DEA resonance with its maximum at 6.5 eV [22, 80, 98, 123]. The production of O^- at this resonance has been measured and the obtained ion yield curve is shown in figure 6.2.

In the reaction

$$O_2 + e^- \longrightarrow O^- + O \tag{6.1}$$

all excess energy is present as kinetic energy of the fragments with each fragment receiving half of the total energy. First, the sphere in momentum space on which all anion momenta from DEA are found is used for a qualitative calibration of the measured momenta in the three directions, ensuring that no distortion of the sphere in any direction is visible.

The KER of the reaction is then calculated from the momentum of the detected negative ion and is plotted against the electron impact energy in figure 6.3. The resulting distribution must be a straight line with a slope of one which crosses the electron impact energy axis at $E_{bind} - EA = 3.651\,\text{eV}$. This knowledge is used for quantitative calibration of the KER as well as the projectile energy. After calibration of electron impact energy as well as of all momentum components the KER is in very good agreement with the expected value which is shown by the black line in figure 6.3.

6.2 DEA in ammonia

The ammonia molecule has a C_{3v} symmetry and its shape is depicted in the inset of figure 6.4. In its electronic ground state ammonia has the electronic configuration $1a_1^2 2a_1^2 1e^4 3a_1^2$ and the state has a $^1A_1$ symmetry. In dissociative electron attachment, an electron from the $3a_1$ orbital can be excited to the $4a_1$ orbital while the projectile is captured in the $4a_1$ orbital as well. The resulting NH_3^- ion is in the $1a_1^2 2a_1^2 1e^4 3a_1 4a_1^2$ (symmetry $^2A_1$) configuration. This attachment process is an $A_1 \rightarrow A_1$ transition, in which the symmetry of the electronic wave function in both the initial state and the final state are the same. This transition occurs around a projectile energy of 6 eV. Alternatively, an electron from the lower lying $1e$ orbital can be excited, leading to the anion in the $1a_1^2 2a_1^2 1e^3 3a_1^2 4a_1^2$ (^2E) configuration. This attachment process is an $A_1 \rightarrow E$ transition and it occurs around a projectile energy of 11 eV.

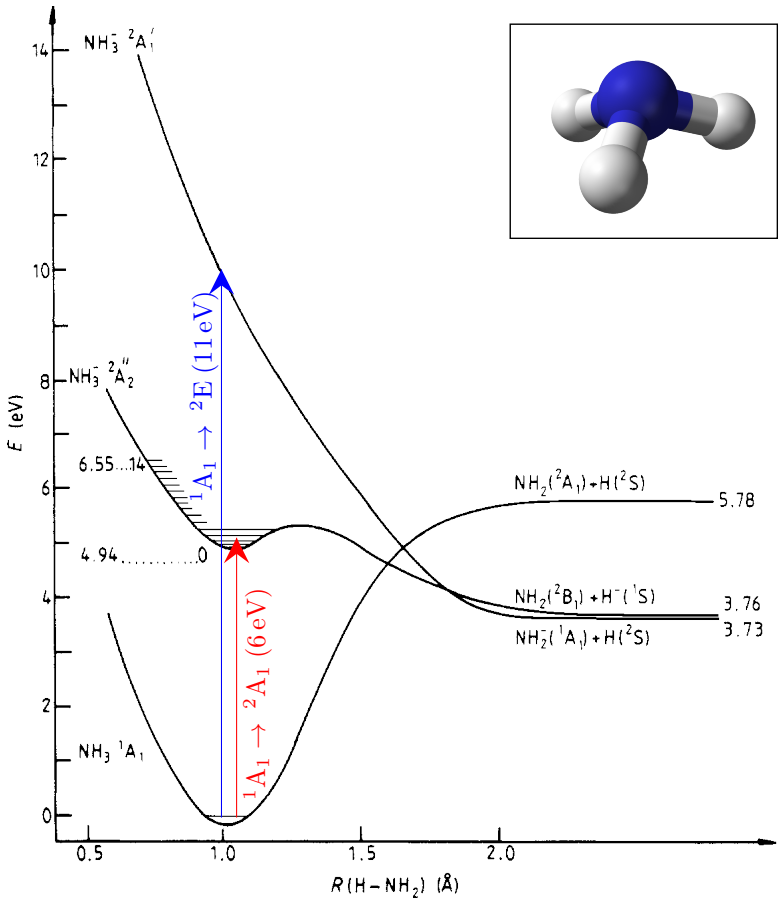

Figure 6.4: Sketch of some potential energy curves as a function of N-H bond distance. The figure has been adopted from Tronc *et al.* [121] and their labeling of the states differs from ours because changing the length of one N-H bond lowers the symmetry. $^2A_2''$ corresponds to the $^2A_1$ state and $^2A_1'$ corresponds to the ^2E state. The transitions shown in red and blue use the nomenclature for the states in equilibrium geometry. The inset shows the molecular geometry in ammonia, where the blue sphere represents nitrogen and the white ones represent hydrogen.

Figure 6.4 shows a sketch of the potential energy curves from Tronc *et al.* for the different electronic states as a function of N-H bond distance. The above mentioned transitions which lead to dissociative electron attachment are shown in the figure as well. The $A_1 \rightarrow A_1$ transition is shown by the red arrow and the $A_1 \rightarrow E$ transition

by the blue arrow. The labeling of the states in this figure differs from the ones used above because changing the length of only one N-H bond breaks the rotational symmetry of the system and the molecule is left in a C_S symmetry. When naming states, we will use the labeling from the equilibrium geometry of the neutral and additionally give the labels of the states in C_S symmetry in brackets.

Tronc *et al.* performed anion yield measurements which showed a vibrational structure in the 6 eV resonance. This led them to the conclusion that the potential curve of the $^2A_1$ state ($^2A_2''$ in C_S symmetry) of the parent anion NH_3^- has a minimum at a bond length similar to the equilibrium bond length of the neutral molecule. It means that the dissociation via this resonance is not direct, but the parent anion is metastable. The absence of a vibrational structure in the anion yield at the second resonance (with the parent anion in the ^2E state) showed that this state is directly dissociating.

The electron attachment occurs via a Franck-Condon transition, i.e. the electron attachment is much faster than the nuclear motion. In a graph like the one in figure 6.4 this means that the transitions are vertical. The projectile energy at which a transition can take place is therefore restricted by the potential difference of the electronic states within the range of bond distances allowed for the vibrational ground state. The metastable character of the lower resonance via the $^2A_1$ ($^2A_2''$) state leads to a more complex dissociation process because the molecular shape can change after the attachment but before the dissociation. This resonance will be investigated in the following section.

6.2.1 Momentum imaging in ammonia

Most experiments and theoretical calculations which investigate the differential cross sections for dissociative electron attachment focused on small - usually diatomic - molecules in the past. Polyatomic molecules like ammonia add complexity to the problem, e.g. because the shape of the molecule can change after electron attachment and before dissociation which in turn influences the angular distribution of the fragments. Additionally, vibrational excitation of the fragments is possible, which influences the kinetic energy release. The theory of O'Malley and Taylor which describes the allowed angular distributions for different symmetries of the involved electronic state is only valid if no change in the molecular shape takes place. Small polyatomic molecules therefore are good test objects for this theory, while at the same time being a challenge for *ab initio* theoretical calculations.

Before this work, no reliable angular resolved experiment for the NH_2^- fragment was available because previous experiments were unable to measure the low kinetic energies involved. We investigated ammonia both in the Heidelberg DEA setup and in the GASIC setup at the Open University in Milton Keynes. In the Heidelberg setup, we were able to study the momentum distributions of NH_2^- via the resonance around 6 eV projectile energy in detail. The Milton Keynes setup was used to measure both the H^- and NH_2^- fragments at this resonance.

Figure 6.5 shows momentum images of NH_2^- from several groups compared to our own measurements in the Heidelberg setup. The comparison clearly shows the su-

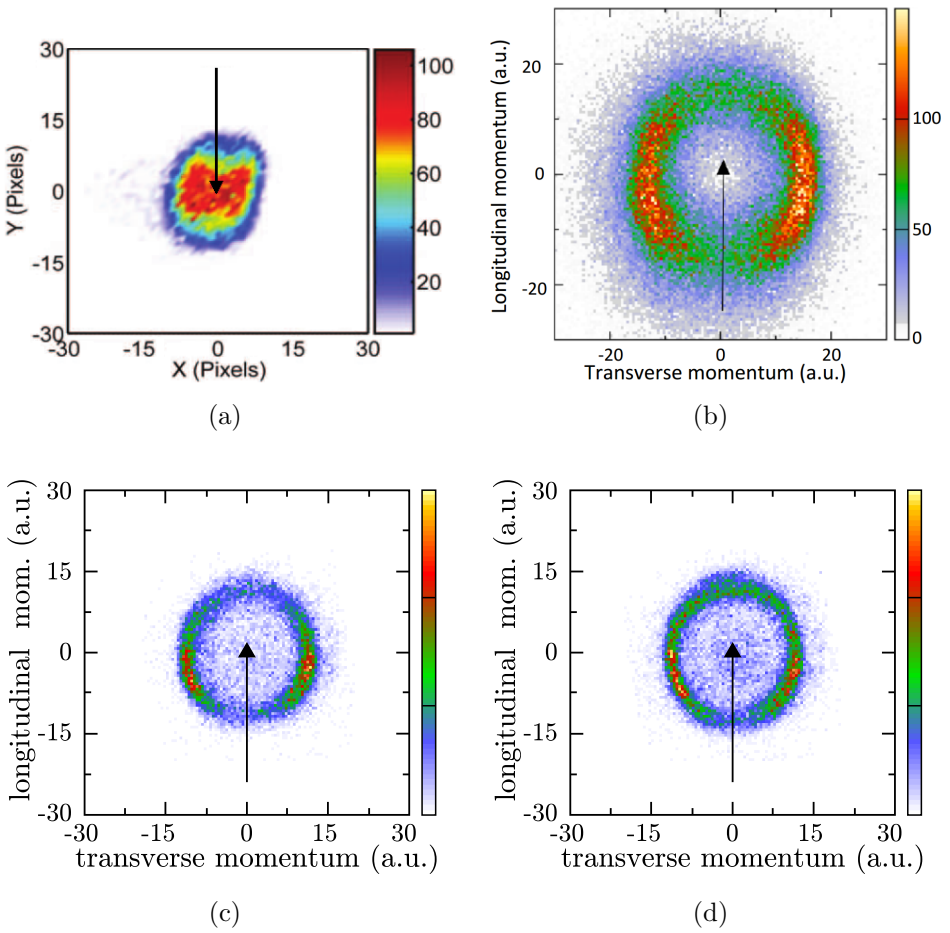

Figure 6.5: Momentum images of NH_2^- taken (a) by Ram *et al.* [11] in the TIFR apparatus at 5.5 eV projectile energy and (b) by Slaughter [101] in the LBNL apparatus at 5.0 eV projectile energy are compared to our measurements using the Heidelberg apparatus at (c) 5.0 eV impact energy and (d) 6.3 eV impact energy. The black arrows show the electron impact direction. Note that the experiment by Ram *et al.* has no quantitative momentum scale and a different electron impact direction than the other measurements.

perior resolution of our apparatus. The measurements at the TIFR apparatus[1], which are shown in figure 6.5(a) are barely able to observe any anisotropy in the momentum distribution. The measurements in the LBNL apparatus[2], shown in figure 6.5(b) already show a good momentum image but with broader structures. In figure 6.5(c), the direct comparison to our momentum image at the same projectile energy shows a much better resolution.

At an impact energy of 5 eV our momentum images show a broad peak around 110° from the projectile direction and a sharp kinetic energy distribution, which can be seen by the narrowness of the ring in figure 6.5(c). The observed momentum image is the inversion of the H^- distribution which was measured by other groups [121, 11] as well as in our own experiments using the GASIC setup at the Open University

[1]The measurements were performed by B. Ram and E. Krishnakumar at the Tata Institute for Fundamental Research in Mumbai, India.

[2]The measurements were performed by D. Slaughter at the Lawrence Berkeley National Laboratories in Berkeley, California, US.

(cf. figure 6.9). The distributions are expected to be inverted images of each other because both H^- and NH_2^- production arises from electron attachment to the same dissociative state of the parent anion, namely the $^2A_1$ ($^2A_2''$) state. H^- is the natural product of the dissociation. However, there is a crossing of the energy curve with that of the ^2E ($^2A_1'$) state, which leads to the creation of NH_2^-. This level crossing can be seen in figure 6.4 at a bond length of R=1.7 Å.

The crossing of the energy curves takes place in a late stage of the dissociation when the bond length of the dissociating bond is high and it can lead to a charge transfer from the hydrogen fragment to the NH_2 fragment [121, 101]. This charge transfer has no influence on the angular distribution because the direction of the fragments is already set at that time in the dissociation process. In a 2-body dissociation like this one, the two fragments have to be ejected back-to-back and with the same momentum to observe momentum conservation. We therefore expect the same angular distributions for both fragments, except being inverted. The kinetic energy release for both products has to be almost the same as well because the energy of both the $^2A_1$ ($^2A_2''$) state and the ^2E ($^2A_1'$) state for infinitely large separation of the fragments (i.e. after dissociation) differs by only 30 meV which is below the experimental resolution. The final energies are so close in these processes, because the electron affinities of the fragments NH_2 and H are very similar.

Angular distribution of NH_2^- at 5 eV projectile energy

The angular distribution of the NH_2^- fragment after DEA of ammonia at a projectile energy of 5 eV can be compared between different experiments as well as theory. Figure 6.6 shows the angular distributions which were measured in different groups, including our own observations (red diamonds), as well as the theoretical calculations (black lines). All experiments agree qualitatively and show a broad peak around 110°. The experiments by the LBNL group (green circles) and the TIFR group (blue squares) both show a much lower contrast between the directions with highest and lowest yield compared to our observations. When the angular distribution of the H^- fragment measured by the LBNL group is reflected through 90° (purple triangles), it matches perfectly with our NH_2^- results. This agreement between the angular distributions of the two fragments shows that they are produced from the same state of the parent anion. The comparison of our measured angular distributions for NH_2^- with those from other groups (the LBNL group as well as the TIFR group) show only mediocre agreement. The much lower contrast between angles with highest and lowest yield in the experiments by other groups demonstrates the insufficient momentum resolution for heavy or slow fragments resulting from the use of an effusive gas beam. These experiments are better suited for the measurement of fragments with high kinetic energy, like the H^- fragment.

The DEA dynamics in ammonia at an impact energy of 5 eV have recently been described using *ab initio* complex Kohn calculations by Rescigno *et al.* [101]. Their calculation of the angular distribution is carried out in several steps. In the first step, the electron entrance amplitude is calculated. The square of the modulus of this value describes the probability for the electron to be captured by the molecule (the electron attachment probability), depending on the projectiles direction relative to the molecule. This attachment probability is depicted in figure 6.7. In this picture the direction of a lobe corresponds to the direction in which the incoming electron

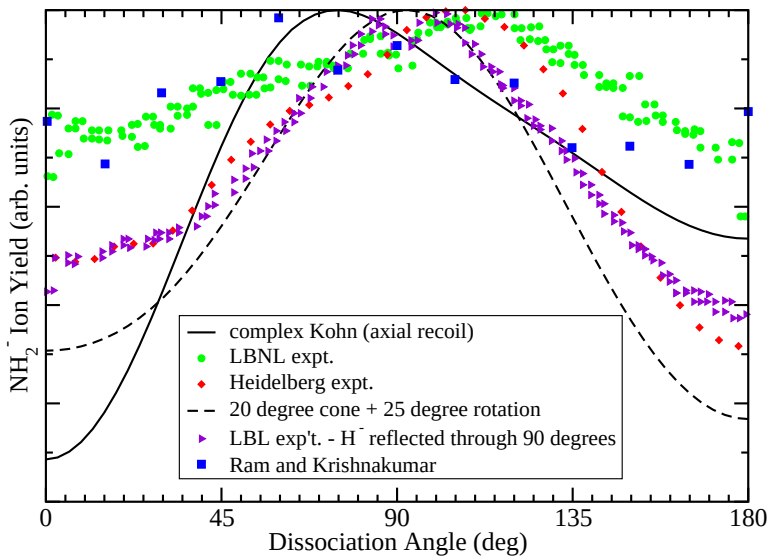

Figure 6.6: Angular distributions for production of NH_2^- by DEA in ammonia at an impact energy of 5 eV. Experimental results from several groups and theoretical calculations are compared. The figure has been taken from [101].

was traveling before the attachment. It shows that the attachment occurs most likely along the rotational symmetry axis of the molecule and more likely from the side of the hydrogen atoms. In a second step the angular distribution of a fragment is calculated from the electron attachment probability, assuming axial recoil of the fragments.

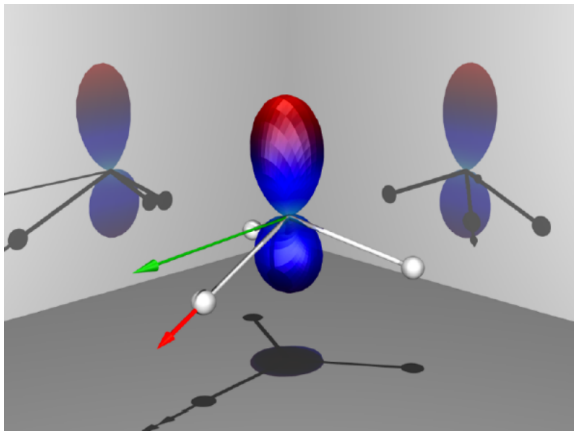

Figure 6.7: Electron attachment probability as a function of the projectile direction, calculated by Rescigno *et al.* using the complex Kohn variational method at a projectile energy of 5 eV. The white balls represent hydrogen atoms, ammonia is located in the middle of the picture. Figure taken from [101].

With this method, Rescigno *et al.* calculated the angular distributions which should be expected for the NH_2^- fragment as well as the H^- fragment. The calculations do not include a change in the geometry of the molecule after electron attachment by default. When the calculations are performed with the equilibrium geometry of ammonia, they obtain a different angular distribution than has been observed in all experiments (cf. figure 6.6, solid black line). They reach better agreement with experimental results by adding a rotation of the dissociating N-H bond by 25°

towards higher angles[3] as well as an averaging over a dissociation angle range of 20° to account for the experimental resolution. The rotation of the dissociating bond is backed up by structure calculations which show a barrier against direct dissociation at the equilibrium geometry of NH_3. Rotating the N-H bond lowers the energy barrier and makes the parent anion unstable at a rotation of 25° [101]. When this structural change between attachment and dissociation is taken into account, the *ab initio* calculations reproduce the measured angular distributions very well. The results of those calculations are also shown in figure 6.6 by the dashed black line.

Momentum imaging of NH_2^- at different projectile energies

The energy resolution of 200 meV in our setup is better than in most comparable setups which use a thermionic emission gun and give resolutions between 500 meV [11] and 800 meV [2]. We made use of this ability by scanning the electron energy in small steps of 100 meV over the whole range of the $^2A_1$ ($^2A_2''$) resonance from 4.3 eV to 7.3 eV to observe any changes in the momentum images within the resonance.

Firstly, figure 6.8(a) shows the kinetic energy release over the whole range of the resonance. When increasing the electron beam energy within the range of the resonance, the additional energy must either be converted to internal energy of a fragment in the form of rotational or vibrational excitation, or it must increase the kinetic energy release. While measurements of rotational and vibrational excitation are not possible in the kind of experiment we performed, additional kinetic energy will increase the size of the momentum sphere and is therefore detectable in our setup. For diatomic molecules, this increase in kinetic energy release is very well observable because there are no internal degrees of freedom (rotation or vibration) to store energy and all excess energy is transferred to kinetic energy of the fragments.

The kinetic energy release in dissociation of ammonia however only shows a slight increase with increasing impact energy as can be seen in figure 6.8(a). Over an impact energy range of 2.2 eV the kinetic energy release only increases by 0.4 eV. At the low energy end of the resonance, at 4.7 eV, all available energy is accounted for. The energy difference between the ammonia ground state and the dissociation products after electron attachment is 3.7 eV and the kinetic energy release at this impact energy is 1 eV. Therefore, the NH_2^- fragment at this energy is expected to be produced in the vibrational ground state or in one of the lowest vibrationally excited states. At the other end of the resonance, at 6.9 eV impact energy, the kinetic energy release is 1.4 eV, leaving around 1.8 eV "missing". This energy must be stored in the internal degrees of freedom of NH_2^-. The fragment thus has to be present in a high vibrationally excited state.

Additionally, the angular distributions over the full range of the resonance have been observed and are shown in figure 6.8(b). They stay constant with the broad peak around 110° for low energies. Approximately at the resonance maximum of 5.7 eV the direction of maximum yield shifts backwards until it reaches 140° at around 7.0 eV impact energy while another peak develops for forward scattering at 0°. This is the first measurement which shows a change of the fragment angular distribution for DEA in ammonia. Previous studies were all performed at only one impact energy.

[3] In figure 6.7 this corresponds to turning the hydrogen of the dissociating bond upwards.

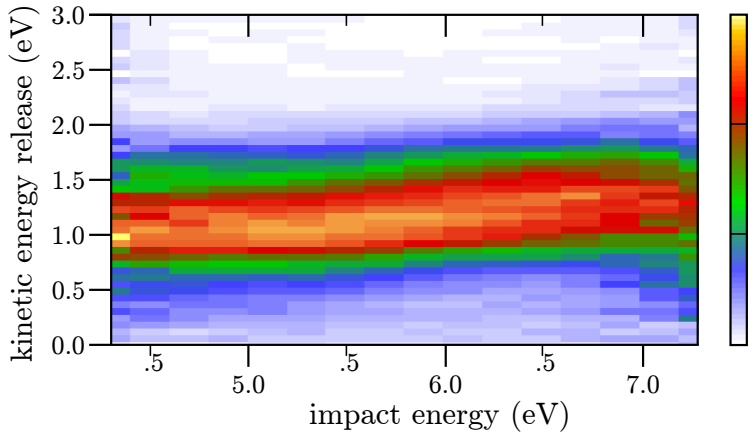

(a)

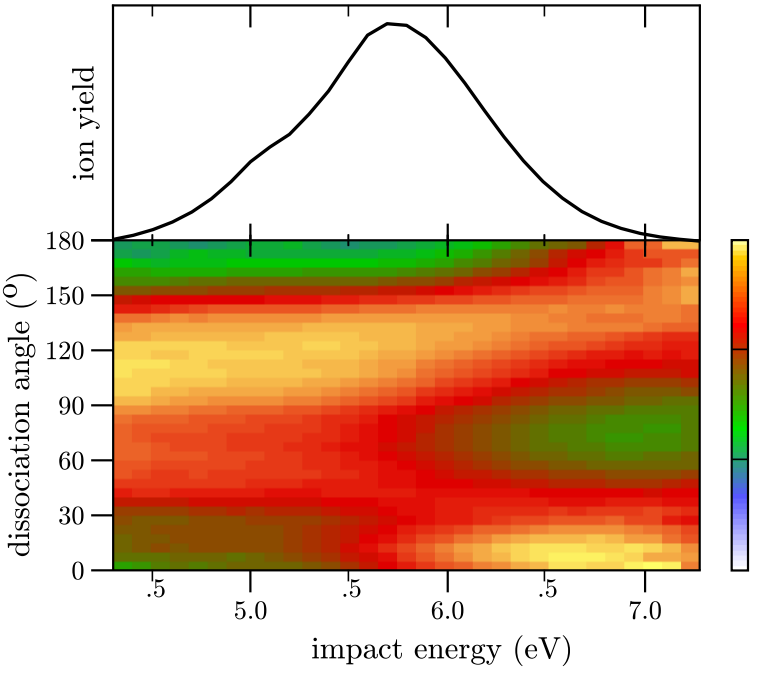

(b)

Figure 6.8: Change of (a) the kinetic energy release and (b) the angular distribution of NH_2^- ions with changing electron impact energy within the $^2A_1$ ($^2A_2''$) resonance. The ion yield curve of the resonance is shown in (b) as well.

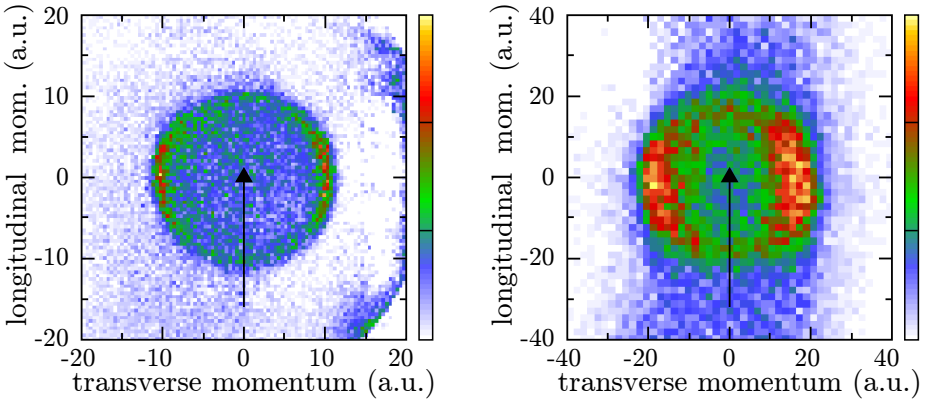

Figure 6.9: Momentum images of H^- from NH_3 at 5.5 eV (a) as well as NH_2^- from NH_3 at 5.9 eV (b), taken in the GASIC apparatus at the Open University.

We observe a discrepancy between the momentum images of the NH_2^- fragment measured in the Heidelberg setup and the measurements performed by D. Slaughter in the LBNL apparatus, which are shown in figure 6.5(b) and (c). We measure a momentum of 12 a.u. while in the LBNL apparatus apparatus a momentum of 20 a.u. is observed. We also performed our own measurements of H^- and NH_2^- in the GASIC apparatus at the Open University, which are shown in figure 6.9. For the NH_2^- fragment, we observed a momentum of 20 a.u. and for the H^- fragment a momentum of 12 a.u. The momentum of both possible anions created in this reaction must have the same absolute value because the electron affinities for both fragments are very similar. Therefore, the same excess energy is available in both cases. The lower momentum measured for H^- is in agreement with the kinetic energy measurement of Tronc *et al.* [121] and with momentum images of this process by Ram *et al.* [11] as well as with the results obtained at the Heidelberg DEA setup for NH_2^-. The higher momentum for NH_2^- has been observed in the GASIC setup as well as by the LBNL group and the TIFR group in their experiments. All three setups use an effusive gas beam. This higher momentum is clearly not representing the physical reality but is an experimental effect induced by the gas delivery system. The observation of larger momenta in these measurements is most likely caused by the higher initial thermal velocity distribution in the warm gas beam [101]. This assumption is backed up by the fact that in the Heidelberg experiment we observe the expected momentum of 12 a.u. for the NH_2^- fragment (cf. figure 6.5(c)) and the main difference between our experiment and the other experiments is the lower initial velocity spread of the ammonia in our supersonic gas jet. At room temperature, the kinetic energy of a molecule due to thermal motion is around 40 meV. In the dissociation process, the NH_2^- fragment only gains a kinetic energy of 65 meV, which is comparable to the initial velocity. Since the gas is not cooled in the effusive gas beam, the uncertainty of the momentum measurements is very high in that case. Momentum measurements of H^- yield the correct values even when using effusive gas beams to introduce the ammonia into the experiment. This is to be expected because the H^- fragment gains a kinetic energy around 1 eV and therefore the initial thermal motion becomes negligible.

Angular distribution analysis of NH_2^- using the partial wave expansion

In this section we investigate if the energy dependent angular distribution can be understood from changing partial wave amplitudes and phases in the attachment process. As a second possibility we examine if a transition energy dependence of the change of the molecular bond angle after electron attachment can describe the angular distributions.

At first the measured angular distributions will be fitted by the partial wave expansion (cf. chapter 2.4). Here, the results of the original partial wave expansion by O'Malley and Taylor (from here on called the "uncorrected fit") assuming the equilibrium angle β between the N-H bond and the main axis will be compared to the ones obtained when including our own corrections for the change in the molecular geometry of $\Delta\beta$ =25° which were explained in chapter 2.5 (from here on called the "corrected fit"). We apply this fit for all measured energies, which shows the development of the contributions of different partial waves with changing impact energy.

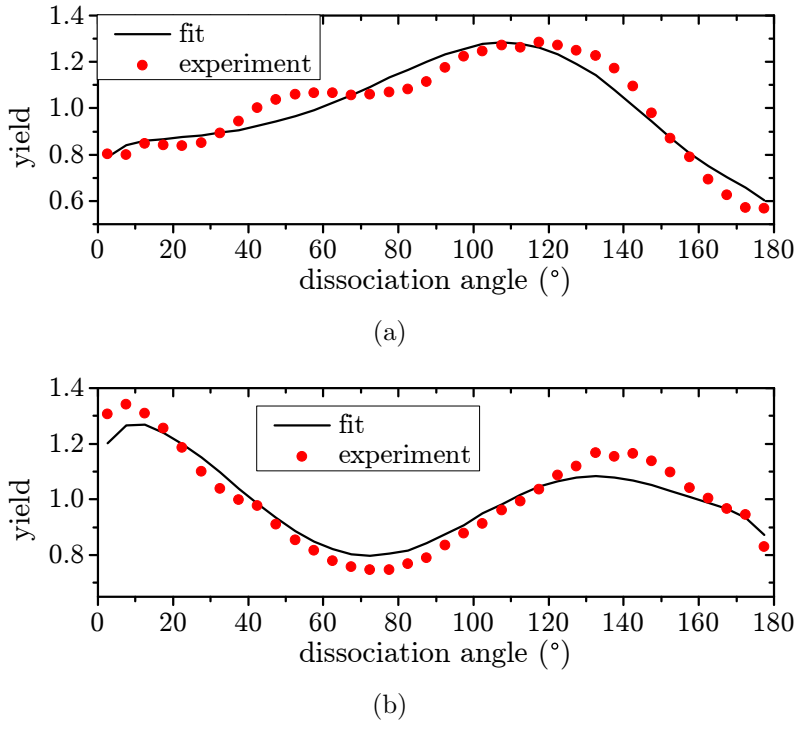

Figure 6.10: Results of the corrected partial wave fit assuming $\Delta\beta = 25°$ compared to measured angular distributions for electron impact energies of (a) 5.0 eV and (b) 6.7 eV.

Figure 6.10 shows measurements and corrected partial wave fits for two different energies. The different angular distributions are in excellent agreement with the fit which assumes a $A_1 \rightarrow A_1$ transition leading to the observed dissociation resonance.

Fitting the angular distributions with partial waves up to $l = 2$ (d-wave) leads to a minimum of five independent parameters: the amplitude of p- and d-wave as well as their phases while the contribution of the s-wave is held fixed, as well as the angle β between symmetry axis and dissociation axis. The angle β is known during electron attachment and can be fixed to the equilibrium angle, reducing the problem to only

four free parameters. When β is left as a fitting parameter as well, the equilibrium angle was found to give the best fit, too. This was checked to verify that fixing β is a reasonable assumption. The s-wave amplitude can also be fixed because both the measured and the calculated distributions are normalized to the same total yield before comparison, which eliminates the total yield as a variable[4].

The amplitudes and phases of the partial waves as a function of projectile energy are shown in figure 6.11. Within the energy range of the investigated resonance, the amplitudes and phases of the partial waves change noticeably. The shown values were obtained when running the fitting procedure several times with random starting points and they furthermore gave very low residuals. Although fitting results varied slightly depending on the starting conditions, the partial wave fits always produced very similar results.

When using the original fitting procedure - which ignores the change of the molecular shape - the phase of the d-wave always stayed at 200° for fits at all electron impact energies. For the partial wave contributions which are shown in figure 6.11 the phase of the d-wave was therefore held constant. This reduced the number of free parameters to three and simplified the fitting procedure. The uncorrected fits are only able to reproduce the experimental results at all due to the fact that the observed reaction is an $A_1 \rightarrow A_1$ transition which allows contributions of all partial waves and thus can show a wide variety of angular distributions. In many other transitions a contribution of the s-wave is forbidden, resulting in much stronger constraints for the allowed angular distributions. For those transitions it is likely that ignoring changes in the molecular geometry will make it impossible to get an adequate fit of the angular distribution at all.

In our corrected fits which include the change of the N-H bond angle, no reduction in the number of parameters was possible. To verify robustness of the fits they were carried out several times, using random starting points. The results of eleven independent fits are shown in figure 6.11. The fitting algorithm gives very reproducible results as can be seen from the almost identical results for all independent fits.

Our partial wave analysis shows that the data can be fitted both with the corrected and the uncorrected fit. In an $A_1 \rightarrow A_1$ transition like the one investigated here, the partial wave analysis is therefore unable to describe the process on its own. The additional information about the molecular dynamics which the *ab initio* calculations provided are necessary to obtain correct partial wave contributions.

Figure 6.11 shows a direct comparison of the amplitudes and phases of the partial waves when using the corrected fit in red and the uncorrected fit in black. Unsurprisingly it shows significant differences between both procedures. When applying the corrections for the changed geometry, we assumed a change in the N-H bond angle of 25°, the same value which was obtained in the *ab initio* calculations of Rescigno *et al.* We further assumed that the change of the bond angle before dissociation does not depend on the projectile impact energy but only on the populated electronic state. According to the structure calculations of Rescigno *et al.*, the potential surface of the populated electronic state becomes unstable and allows dissociation starting at an increase of the bond angle of 25°.

[4]For the figure 6.11, the amplitudes are normalized to one instead of being normalized to the s-wave amplitude, thereby representing the relative contributions.

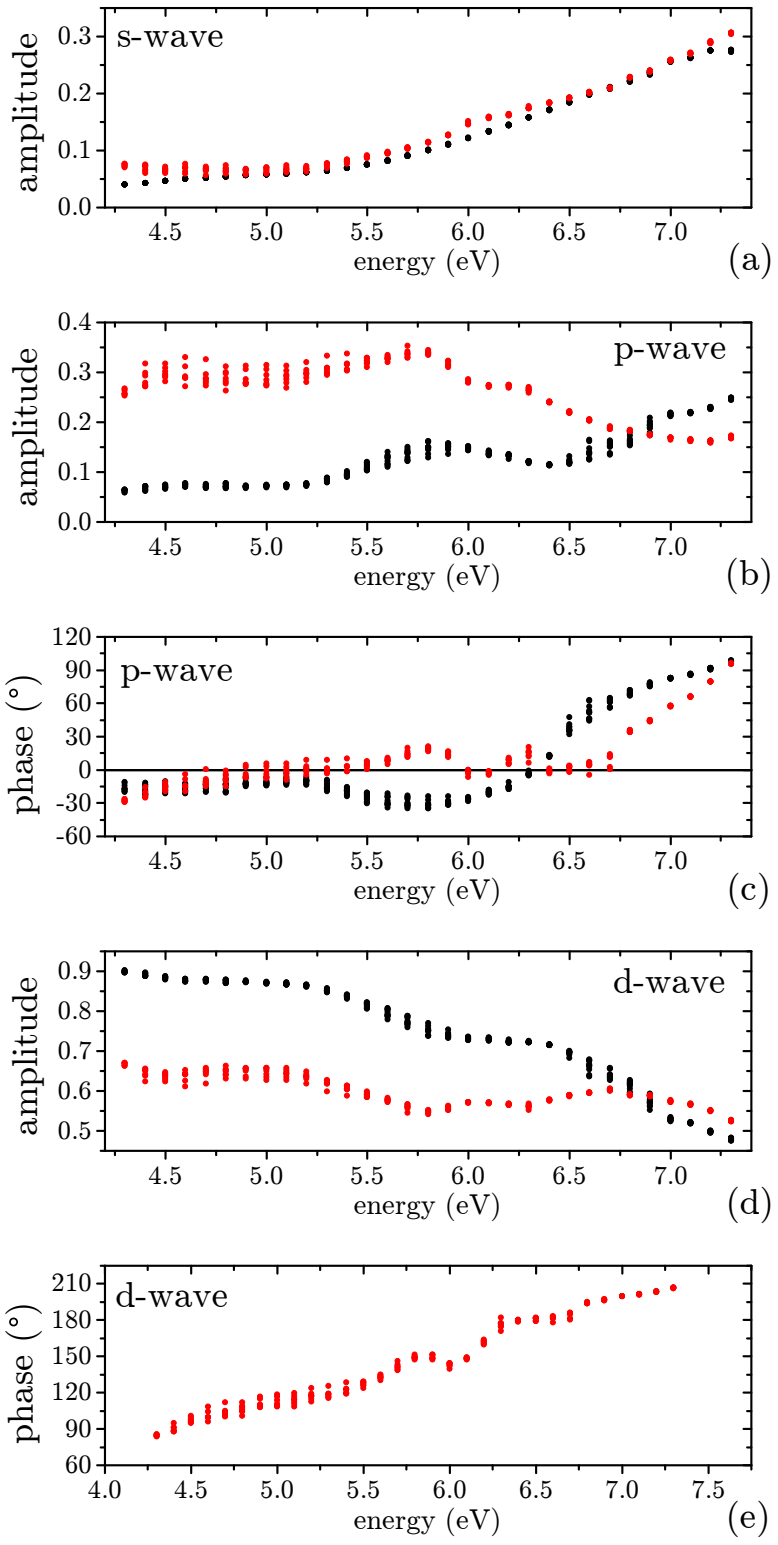

Figure 6.11: Results of 11 independent partial wave fits of the NH_2^- angular distributions. The partial wave amplitudes are normalized. (a) s-wave amplitude, (b) p-wave amplitude, (c) p-wave phase, (d) d-wave amplitude and (e) d-wave phase. The black dots show results for the uncorrected fitting procedure, ignoring the change in the molecular geometry between electron attachment and dissociation. The d-wave phase in this case was constant at 200°. The red dots show the results for the partial wave fit after correcting for the changed molecular geometry.

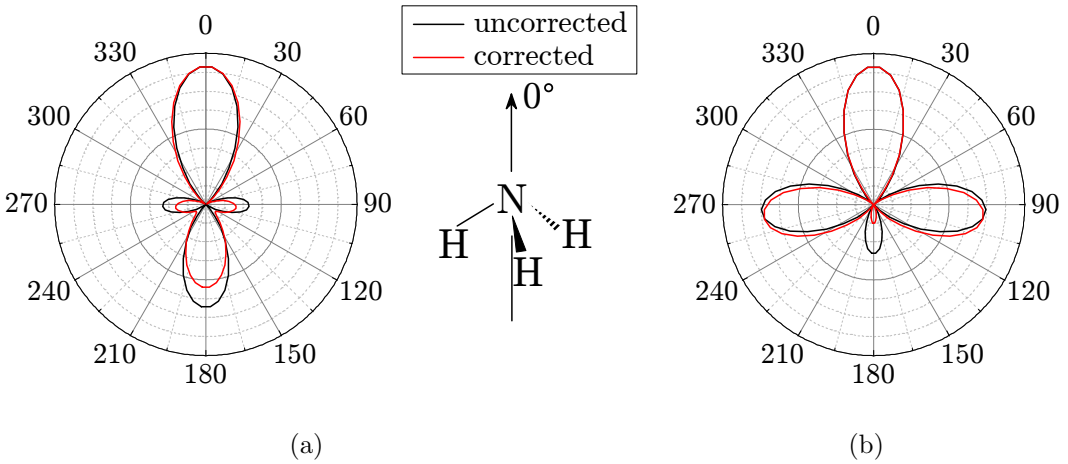

Figure 6.12: Electron attachment probability as a function of the angle between molecular symmetry axis and projectile direction for (a) 5.0 eV impact energy and (b) 6.7 eV impact energy. The distributions which were obtained with the corrected analysis procedure are shown in red and the distributions obtained with the uncorrected theory of O'Malley and Taylor are shown in black. The orientation of the ammonia molecule is shown by the sketch of the molecule. The symmetry axis is oriented vertically and all probabilities are normalized to their maximum.

Using the obtained partial waves, we are able to reconstruct part of the electron attachment probability and compare it to the *ab initio* calculations. The calculated attachment probabilities are shown in red in figure 6.12 as a function of the angle between molecular symmetry axis and projectile direction for two different projectile energies. In the figure, the symmetry axis is oriented along the vertical, as can be seen by the sketched molecule. The orientation is the same as in figure 6.7. The calculated attachment probabilities are averaged over all rotations around the molecular axis because our experiments are not sensitive to the rotation. At an impact energy of 5 eV, the attachment probability which we obtained can be compared directly to the *ab initio* calculations shown in figure 6.7 and good agreement is found. Since the attachment probability which Rescigno *et al.* obtained shows rotational symmetry around the molecular axis, our measurements were able to obtain a very similar picture and preserve all important features. Figure 6.12 also shows the results when using the uncorrected fit in black. In this case, the differences in the obtained attachment probabilities are small and the main effect of our corrected analysis is a lower yield in the attachment probability around 180°.

At a higher impact energy of 6.7 eV, our calculated electron attachment probability changes drastically (cf. figure 6.12(b)). Electron attachment from the side of lone electron pair of nitrogen (at 180°) becomes very unlikely and a peak of high attachment probability develops at 90° from the molecular axis.

Alternatively, we can try to explain the energy dependent fragment angular distribution not by changes in the electron attachment probability but by different changes of the N-H bond angle before dissociation. In this case, the attachment probability at a projectile energy of 5 eV, which is confirmed by *ab initio* calculations, is assumed to be unchanged and is used at the higher energy as well. The resulting angular distribution is shown in figure 6.13 for a projectile energy of 6.7 eV. When applying this analysis, the angular distribution can be at least qualitatively reproduced. For

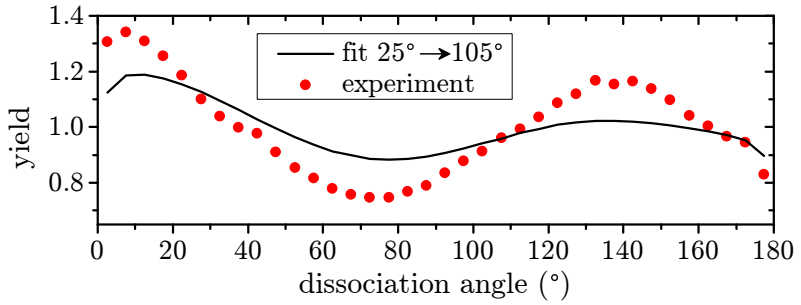

Figure 6.13: Comparison of the fragment angular distribution at a projectile energy of 6.7 eV with the expected angular distribution calculated from the known electron attachment probability at 5 eV when the N-H bond angle is changed by 105°.

the fit in the figure, the angle between the N-H bond and the molecular axis had to be increased by 105° prior to dissociation. At this extreme change of the angle, the dissociating N-H bond has to be almost aligned with the molecular axis before dissociation. Additionally, at this new orientation the hydrogen atoms are closer together than they are in the equilibrium geometry of ammonia. This is unlikely to be an energetically favorable geometry.

When changing the electron attachment probability with the projectile energy we reach very good agreement between the experimental observations and the theory of O'Malley and Taylor, when the theory is adapted to a change in the direction of the dissociating N-H bond. A fixed attachment probability and a strongly changing position of the dissociating N-H bond after attachment however is only able to reproduce the observations qualitatively. A changing attachment probability therefore is the more likely explanation at this point but further *ab initio* calculations are necessary to confirm or refute this finding.

6.2.2 DEA in small clusters

The higher stagnation pressure in the supersonic gas jet compared to effusive gas beams in combination with the cooling of the gas during the expansion in the jet leads to the production of small clusters of molecules [48, 20]. To characterize the jet composition we performed an electron impact ionization experiment for ammonia in our setup. The measured time-of-flight spectrum is shown in figure 6.14. It shows ions with masses corresponding to clusters made from up to 17 ammonia molecules. For the monomer we observe a triple peak containing NH_2^+, NH_3^+ and NH_4^+. While NH_3^+ can be produced by single ionization of a lone ammonia molecule, the other two peaks are created in a dissociative ionization. This is especially important with respect to NH_4^+ because its parent cluster must have been at least a dimer. The presence of this fragment with a yield on the same magnitude as the dimer peak shows that clusters regularly lose molecules or molecular fragments in electron impact ionization and the distribution of measured clusters does not represent the abundance of those clusters in the jet. This can also be inferred from the width of the time-of-flight peaks in figure 6.14. Only the second peak of the triple peak structure for the monomer ($n = 1$ in figure 6.14) is sharp. It corresponds to single ionization of ammonia without dissociation. All other peaks are much broader. This is a typical sign of ions which are produced in a dissociation and therefore have a much higher kinetic energy than ions produced in non-dissociative ionization. Therefore, the abundance

of clusters in the jet will be shifted towards larger clusters compared to what this measurement shows. This also has an important implication for the analysis of negatively charged clusters observed in dissociative electron attachment experiments. We are unable to say with certainty that the cluster size which is observed also is the size of the parent cluster. It is however still possible to compare observations for different fragment sizes because the average size of the parent cluster will rise with rising fragment size. This means that while we cannot analyze individual cluster sizes, we can still study the general influence of the cluster size on the DEA process.

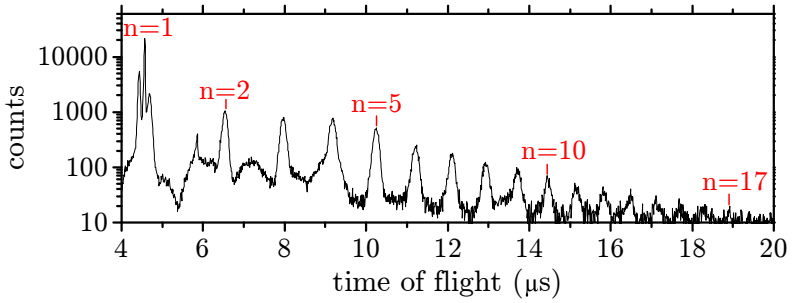

Figure 6.14: Time-of-flight spectrum of the ammonia jet when ionizing the target via electron impact ionization. The peaks show ammonia clusters with size n - the number of molecules in the cluster after ionization - reaching up to n=17.

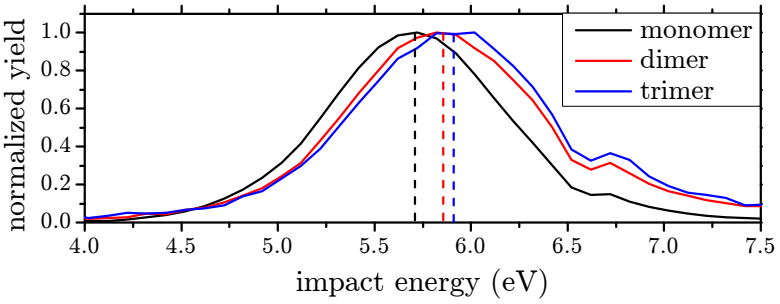

Figure 6.15: Negative ion yield curves as a function of projectile impact energy for the three smallest fragment cluster sizes: NH_2^- (black line), $(NH_3)NH_2^-$ (red line) and $(NH_3)_2NH_2^-$ (blue line).

We investigated the same DEA resonance which was already discussed for the ammonia monomer. We scanned the electron impact energy around the expected resonance energy of 5.7 eV to determine the energy of highest yield for every fragment. Figure 6.15 shows the negative ion yield curves for the three smallest fragments, with the projectile energy of highest yield indicated by the dashed line. This energy of highest yield is shown as a function of the detected fragment size in figure 6.16. The maximum yield position grows quickly from 5.7 eV to 5.9 eV for very small fragments, i.e. dimers and trimers. For larger fragments the maximum yield position soon reaches a constant value for all observed fragments up to a cluster size of n = 17. All fragments were measured simultaneously in the same experiment, i.e. the results are well comparable and not affected by systematic errors between different fragment sizes. We use the following hypothesis to explain our observation: From the theoretical calculations on DEA in ammonia and from the experimental results in ammonia monomers it is known that the vibrational excitation of ammonia after the electron capture plays an important role in the dissociation. The negative ion

has a threshold against dissociation which has to be overcome, this has been shown by several groups [121, 101]. Vibrational excitation of the negative parent ion leads to a destabilization of the N-H bond and subsequently to dissociation. While in a lone molecule the amount of vibrational excitation of the parent anion depends only on the energy of the attached electron, in a cluster the vibrational excitation of each molecule can be lower than in the monomer because the neighboring molecules can be vibrationally excited as well, sharing the excess energy between several molecules. Thus, on average an attachment of an electron with more energy is necessary to reach the same level of vibrational excitation for one molecule in a cluster than in a monomer. Since the energy is transferred to a neighboring molecule, the rise in energy is expected to saturate quickly when a maximum number of nearest neighbors in the cluster is reached and increasing the cluster size does not further help the distribution of vibrational excitation to more molecules.

This process explains our observations: the increase of the maximum ion yield energy, the new constant energy for larger clusters and the amount of the change which is in the range of a vibrational excitation. The lowest vibrational excitations in ammonia have an energy of 115 meV and 200 meV [50]. However, it is not possible to proof this assumption further using our experimental method.

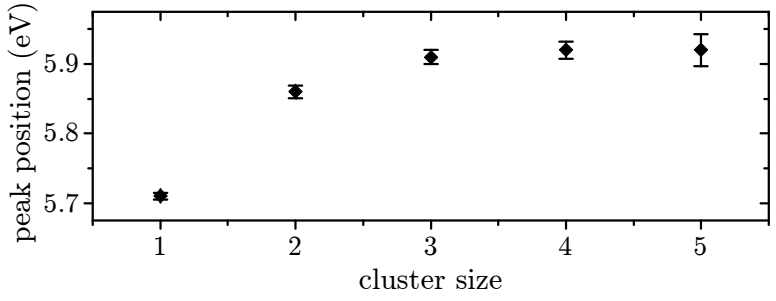

Figure 6.16: Dependence of the energy with the highest yield for dissociative electron attachment to ammonia clusters on the detected fragment size.

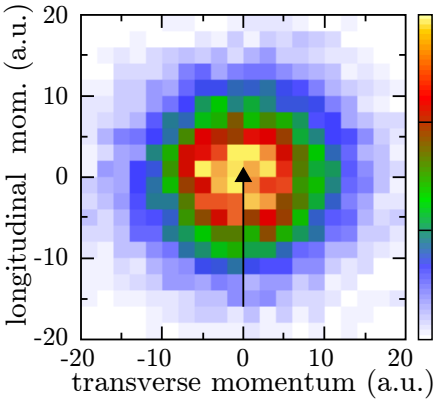

Figure 6.17: Momentum distribution image of the dimer fragment from dissociative electron attachment to ammonia clusters. The black arrow shows the projectile impact direction. The high mass and low kinetic energy of the fragment lead to almost no deflection of the fragment in the dissociation. This makes a measurement of the fragment angular distribution impossible.

An analysis of the angular distribution of the cluster fragments was not possible due to their very low kinetic energy. Combined with the higher mass of the fragments this results in very a small deflection of the ions and the resulting momentum image is dominated by the initial thermal momentum spread and the size of the jet instead of the momentum due to dissociation.

6.3 DEA in formic acid

Formic acid (HCOOH, mass: 46 amu) is an interesting target to investigate DEA in hydrogen bonded clusters of molecules compared to lone molecules. It forms very

stable dimers via hydrogen bonds which can easily persist in the gas phase. The structure of the dimer is depicted in figure 6.19(a). Dissociative electron attachment in formic acid has been studied before and several DEA resonances were found in the monomer [92, 93, 95]. One of those resonances is a shape resonance at a low energy around 1.2 eV which leads to the loss of one hydrogen atom from the molecule. The DEA cross section measurement of this resonance by Pelc *et al.* is shown in figure 6.18 [92] and the same resonance will be investigated in clusters in our experiments. DEA in clusters of formic acid has only been investigated once so far. Martin *et al.* performed mass spectrometry measurements in a jet of clusters [72]. Their experiments were however limited to a single projectile energy of 1 eV. In our experiments we will measure the energy dependence of the hydrogen loss channel in a cluster jet and investigate the processes which influence the dissociation process in clusters.

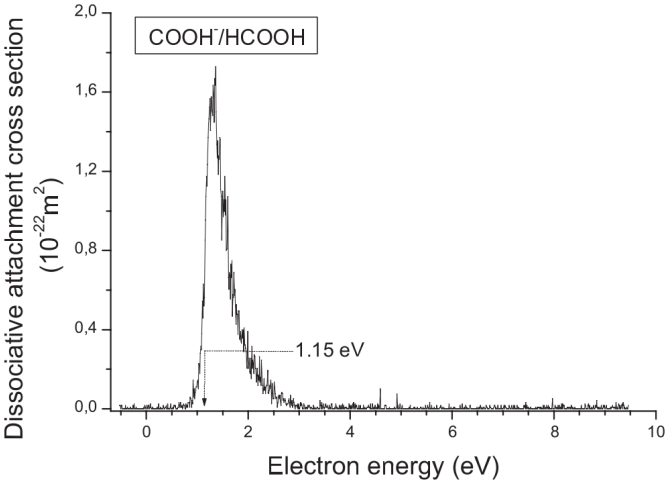

Figure 6.18: Cross section measurement by Pelc *et al.* for the production of $HCOO^-$ from a formic acid monomer by loss of a hydrogen. The picture has been taken from [92].

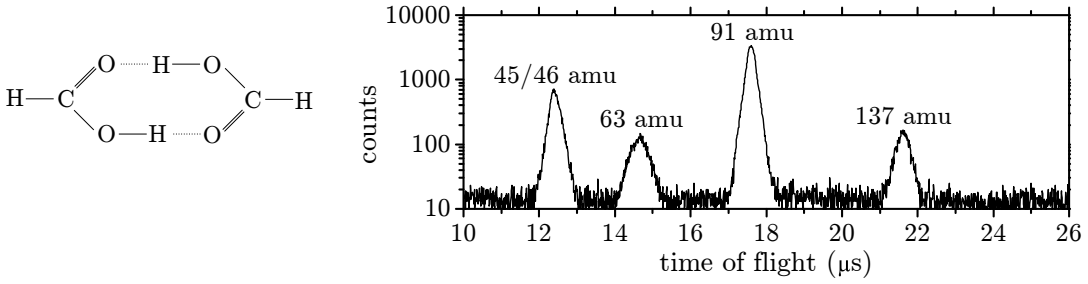

(a) (b)

Figure 6.19: (a) Structure of the formic acid dimer. The two hydrogen bonds (dotted) between the molecules make the dimer very stable. (b) Time-of-flight spectrum of negative ions created in dissociation of formic acid clusters. The electron impact energy has been scanned between 0 eV and 3 eV for this measurement.

In our cold supersonic gas jet we found a high amount of dimers and can use them to compare dissociative electron attachment in dimers to monomers. Figure 6.19(b) shows the time-of-flight spectrum of negative ions which we obtained in a projectile energy range from 0 eV to 3 eV. We observe DEA resulting in an anionic fragment with a mass of 91 amu as the most abundant one. This fragment corresponds to hydrogen loss from a formic acid dimer. The next highest contribution in the time-of-flight spectrum is a combination of ions with the masses 45 amu and 46 amu. The

fragment with the mass 45 amu can in principle be created from the monomer. As we have found from the energy dependence of this fragment however, this fragment can be assigned to the dissociation of a cluster as well. This will be explained below. Therefore, we know that most of the molecules in the gas jet are present as dimers. Small amounts of heavier fragments at 137 amu - whose parent clusters must have been at least trimers - are also observed.

In figure 6.19(b) the fragments with the masses 45 amu and 46 amu are indistinguishable. However, we are able to reconstruct the different contributions. The procedure is shown in figure 6.20. It shows the amount of detected event as a function of fragment mass (calculated from the time-of-flight) and projectile impact energy. In the upper left corner of the distribution the contribution of the 46 amu fragment is visible at an impact energy of around 1 eV. Although the distributions from both fragments overlap, the distribution of each fragment has a width of only 2 amu which allows us to separate them completely. The depicted area is separated in the two parts A and B, where A contains only events with a time-of-flight corresponding to a mass of 45 amu and lower. B contains all events with a higher time-of-flight. Area B includes all events from the 46 amu fragment and half of the events from the 45 amu fragment. Area A however only contains half of the events of the 45 amu fragment and none of the 46 amu fragment. All events from area A are then used to create the resonance curve for the 45 amu fragment, while the difference between area B and area A reconstructs the resonance curve for the 46 amu fragment.

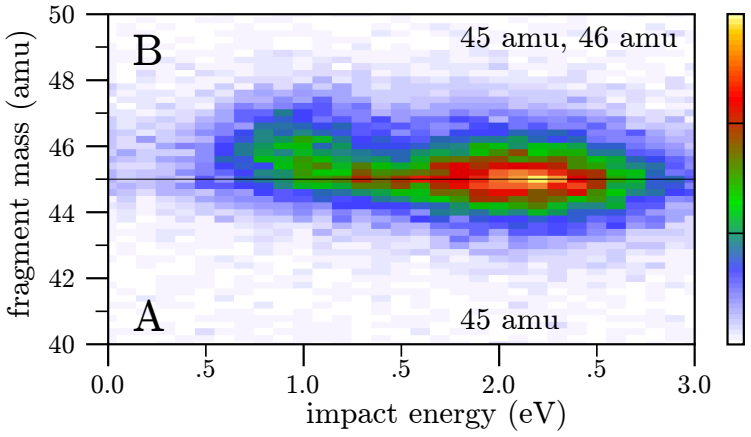

Figure 6.20: Distribution of the measured fragment masses in a projectile impact energy range from 0 eV to 3 eV. The image only shows the region containing the 45 amu and 46 amu fragments. They are separated by dividing the depicted range into two areas. Area A contains the events of the 45 amu fragment and the difference between area B and area A contains the events of the 46 amu fragment.

Formic acid shows several different DEA resonances: one low energy peak in the DEA cross section which is caused by a series of shape resonance at energies around 1.5 eV [93] and several core excited resonances at energies around 8 eV. In this study we will focus on the dissociative electron attachment involving the shape resonances at low electron energy. The different shape resonances in the parent anion $HCOOH^-$ overlap because they are very close in energy. Therefore, in the DEA channel there is only one peak in the energy range of 1 eV to 2.5 eV, the range in which the shape resonances are located. Other groups have shown that these resonances lead to the hydrogen loss channel of DEA, producing the $HCOO^-$

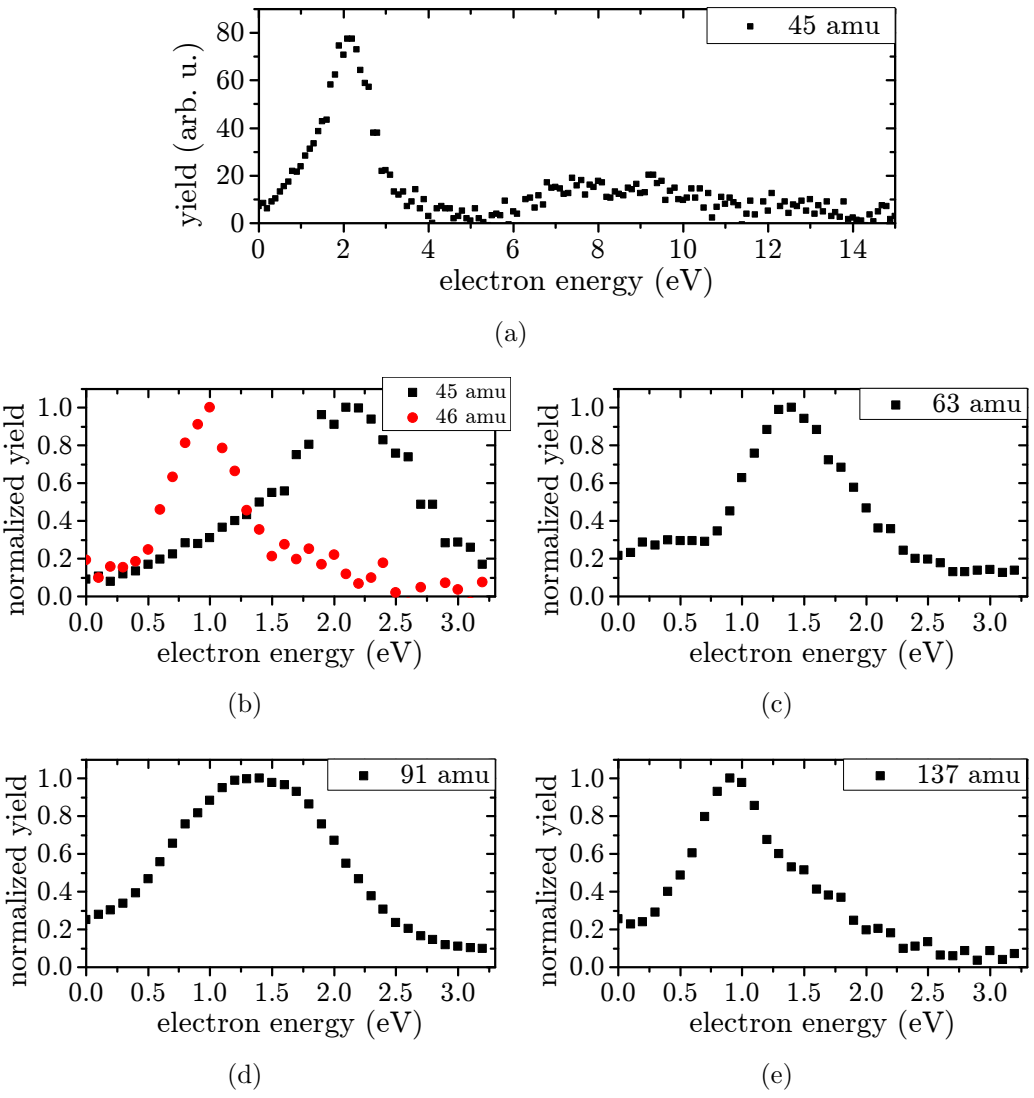

Figure 6.21: Resonances of all observed fragments created by DEA in formic acid clusters.

fragment. In our measurements, we observe hydrogen loss from the dimer (91 amu) as well as from the trimer (137 amu). We also observe hydrogen loss from the dimer in combination with a breaking of the hydrogen bonds of the cluster (45 amu). In the following, we will call the breaking of the hydrogen bond between two molecules of the cluster *evaporation*, while *dissociation* is only used for the breaking of a bond within a molecule. Although we cannot exclude that the 91 amu fragment which we observe contains ions created from evaporation of a formic acid molecule from a trimer combined with dissociation of a hydrogen, it is clear that this process - if present - will have little influence on the 91 amu peak due to the low fraction of trimers in the gas jet compared to dimers.

Additionally we can clearly distinguish a non-dissociative contribution at 46 amu with a resonance at 1.0 eV, which was shown in figure 6.20. The 46 amu fragment has not been observed in studies using effusive gas beams. One study by Martin *et al.*, in which DEA to formic acid clusters at a single fixed projectile energy of 1 eV was investigated using a mass spectrometer, observed the 46 amu fragment [72].

In figure 6.21 we show the the resonance curves for all detected fragments. The fragments with masses 45 amu, 91 amu and 137 amu (figure 6.21(b), (d) and (e)) are all produced by loss of a hydrogen atom in the dissociation but all three ion yield curves are different. The resonance energy in those measurements depends on the mass of the parent cluster. As can be seen in figure 6.21 the energy of maximum yield for the fragments with masses 45 amu (2.2 eV), 91 amu (1.5 eV) and 137 amu (0.9 eV) decreases with increasing fragment mass. The main differences between the formation of those fragments is the parent cluster. We assume that the trimer is the largest cluster contributing significantly to the reactions, which is plausible since we have not observed a tetramer, neither in DEA experiments as shown in figure 6.19 where it would be expected at a time-of-flight of 25 µs, nor in electron impact ionization. When comparing the ion yield curve which we observed for the 45 amu fragment (figure 6.21(b)) with the cross sections measured by Pelc *et al.* (figure 6.18), it can be seen that both distributions are very different. While the distribution which Pelc *et al.* obtained has its maximum at a projectile energy of 1.25 eV, our distribution peaks at 2.2 eV. This shows that the fragment which we observe at a mass of 45 amu does not have the monomer as a parent molecule, but rather the dimer.

We can therefore assume that our jet contains mostly dimers and an additional small contribution of trimers. With this assumption, the production of the 137 amu fragment can be assigned to simple hydrogen loss in a trimer. The 91 amu fragment will be produced mostly by hydrogen loss from a dimer. A very small portion will be produced by evaporation of one formic acid molecule from a trimer followed by hydrogen loss from the remaining dimer. In the same way the 45 amu fragment is produced by the evaporation of one molecule from the dimer, followed by a hydrogen loss. The evaporation of two molecules from the trimer and hydrogen loss is a minor contribution to the production of this fragment. The same process has also been suggested by Martin *et al.* [72] from their mass spectrometric results. Our additional observation of the changing energy of maximum yield for different fragment sizes reinforces this interpretation, as will be discussed in the following.

The capture of the projectile electron adds energy to the molecule. The energy can be stored in the molecule as electronic, vibrational and rotational excitation. In the low energy range (below 5 eV) investigated here the electron is captured into a shape resonance. Therefore the transient negative ion will not show any electronic excitation and the electron will be captured into the lowest unoccupied molecular orbital. No energy is inherently transferred to an internal degree of freedom in this resonance, but when the negative ion has a new equilibrium geometry, higher vibrational levels are excited. The larger clusters are only stable when the internal energy after dissociation is low. If the energy which is stored in vibrational excitation is higher than the energy necessary to break the hydrogen bond between the molecules, a molecule can evaporate from the cluster. This process shifts the yield for larger fragments to lower energies within the resonance while the yield for small fragments is shifted to higher energies where the probability for evaporation of a molecule from the cluster (i.e. predominantly from the dimer) is increased. The binding energy of a formic acid dimer is 0.62 eV [60] which fits very well to the experimental shift in the DEA peak maxima of 0.7 eV between the 45 amu and 91 amu fragments as well as the shift of 0.6 eV between the 91 amu and 137 amu fragments.

The only fragment which does not fit this scheme is the non-dissociative negative ion

at 46 amu. It has only been reported in the study of Martin *et al.* before and they conclude that it is a result of electron attachment to a cluster followed by evaporation of intact molecules from the cluster. The evaporation removes excess energy from the system and stabilizes the remaining fragment at least on the experimental time scale of tens of microseconds. This observation is especially interesting because it contradicts earlier *ab initio* calculations by Pelc *et al.* [93] which obtained a negative electron affinity for formic acid. Accordingly, no stable parent anion was found or even expected in studies of the formic acid monomer.

Our ion yield measurements show a shift in the energy of maximum yield for the non-dissociative anion to lower energies than any fragment which is created by dissociation. These findings are consistent with the picture of Martin *et al.* When evaporation occurs after attachment of a low energetic electron, the internal energy of the remaining negative ion can be decreased below the energy necessary for dissociation. A decay by auto-detachment of the electron however is only inhibited when the molecule has a positive electron affinity which stabilizes the negative ion, as suggested by Martin *et al.* [72]. However, their assumption of a positive electron affinity is in conflict with the negative electron affinity which has been calculated by Pelc *et al.* The existence of fragments created both by non-dissociative evaporation (creating $HCOOH^-$) and non-evaporative dissociation ($HCOOH{\cdot}HCOO^-$ from $(HCOOH)_2$) shows that both processes are occurring at the same time and are competing.

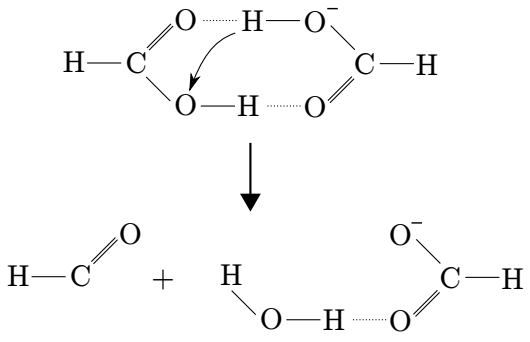

Figure 6.22: Dissociation pathway for creation of the 63 amu fragment. The detached hydrogen reacts with the OH-group on the neutral side of the dimer, forming water which stays attached to the negative ion via a hydrogen bond. Figure adopted from [72].

The 63 amu fragment consists of a dehydrogenated formic acid molecule with a water molecule attached to it. As shown in figure 6.22, the water can be created after dehydrogenation of a dimer, when the free hydrogen atom doesn't leave the dimer but instead attaches to the OH-group on the neutral side of the dimer, as concluded by Martin *et al.* [72]. Our ion yield curve for this fragment (cf. figure 6.21(c)) shows the maximum yield at the same energy as the production of the dehydrogenated dimer (figure 6.21(d)), but the resonance for this channel is narrower than that for the dimer hydrogen loss. Instead, the width and shape are in excellent agreement with hydrogen loss from a monomer as measured by Pelc *et al.* [93], which was shown in figure 6.18. The first step in the production of the 63 amu fragment is exactly the same as the hydrogen loss channel in the monomer. Despite the interaction of the hydrogen with the second molecule, the ion yield curve of this channel is influenced less by the presence of other molecule.

Finally, we discuss the $HCOO^-$ (45 amu) yield at higher energies between 6 eV and 14 eV, which is depicted in figure 6.21(a). Previous studies in monomers showed no

such peak for this fragment and only small cross sections for production of OH^- and H^- via a core-excited resonance in the impact energy range between 6 eV and 10 eV. The observed $HCOO^-$ fragment at this higher energy must therefore be created from a cluster, most likely a dimer. It shows that the dissociation paths are strongly influenced by the second molecule in the dimer. This can be expected since a dissociation path which would lead to production of OH^- by breaking one of the C-O bonds will be suppressed by the presence of the second molecule. When the C-O bond is broken the fragment is still bound to the second molecule via the hydrogen bond. Therefore, the hydrogen bond needs to be broken as well. This process is less likely because it requires two bonds to be broken which requires more energy. If it should occur nonetheless, the process would be very slow because the created fragments are heavy and thus dissociation takes a longer time than in the case of a hydrogen loss. Auto-detachment is therefore more likely in clusters than in monomers and DEA is suppressed for those slow channels.

Hydrogen loss channels are influenced by the additional hydrogen bond in the dimer in the same way. In the low energy range below 3 eV it is very likely that the channel of hydrogen loss combined with evaporation - which creates $HCOO^-$ from dimers - has a lower cross section than simple hydrogen loss from monomers. At this projectile energy, the energy which is added to the system is barely enough to allow dissociation. When the energy is spread between the vibrational degrees of freedom, dissociation can be inaccessible. This is the same process which also leads to the non-dissociative evaporation, which was discussed before.

While in formic acid monomers different negative ions are created in the higher projectile impact energy range above 6 eV, the $HCOO^-$ ion at 45 amu is the only product which we could observe for DEA in formic acid dimers in this energy range. It shows that the reaction pathway in the dimer is different from that in a monomer. The process of hydrogen loss and evaporation of a molecule from the dimer is favored over other dissociation channels.

6.4 DEA in water

Water is a bend molecule with a C_{2v} symmetry. Its ground state electron configuration is $1a_1^2 2a_1^2 1b_2^2 3a_1^2 1b_1^2$ and the H-O-H bond angle in the ground state is 104.5°. This bond angle depends on the occupied orbitals. The Walsh correlation diagram in figure 6.23 depicts the energy of the highest occupied orbitals in water ($2a_1$, $1b_2$, $3a_1$ and $1b_1$) as well as the two lowest unoccupied orbitals ($4a_1$ and $2b_2$) as a function if the bond angle. The $3a_1$ orbital gets stabilized - i.e. its energy is lowered - when the bond angle is decreased while most other orbitals get destabilized. At the equilibrium bond angle shown by the dashed line in the figure the sum of the energies of all occupied orbitals is minimized. With respect to dissociative electron attachment an important consequence of this behavior is that the equilibrium bond angle of the parent anion depends strongly on its electronic state.

There are three DEA resonances in water, corresponding to electron capture into the lowest unoccupied molecular orbital ($4a_1$) in combination with excitation of an electron from one of the outermost orbitals into the $4a_1$ orbital. The first resonance is the $^2B_1$ resonance with the electronic configuration change $1b_1^{-1}4a_1^2$, around an im-

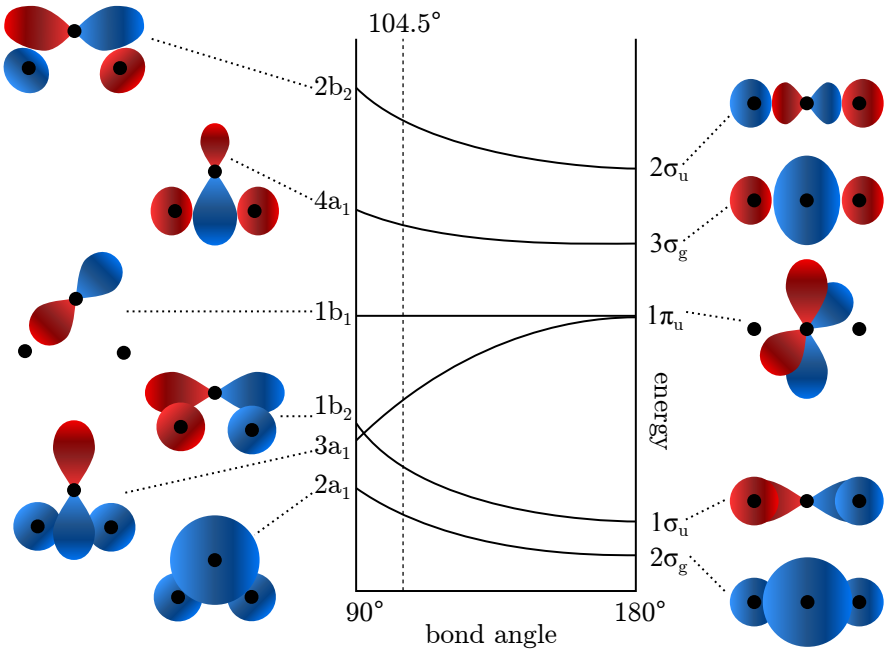

Figure 6.23: Walsh correlation diagram for water. The energies of the different orbitals are qualitatively shown as a function of the H-O-H bond angle. Increasing overlap of the wave functions decreases the energy of the orbital and decreasing overlap of the wave functions increases the energy of the orbital. Sketches of the orbitals are shown for every symmetry. Here, blue and red parts represent positive and negative values of the wave function, respectively.

pact energy of 7 eV[5]. The next resonances are the $^2A_1$ resonance with the electronic configuration change $3a_1^{-1}4a_1^2$, around an impact energy of 9 eV and the $^2B_2$ resonance with the electronic configuration change $1b_2^{-1}4a_1^2$, around an impact energy of 12 eV.

In the dissociation of the H_2O^- parent anion, the negative fragments H^-, O^- and OH^- can be produced. In this work, we will only discuss the dissociation channel which produces O^- which was investigated in our own experiments.

Existing investigations of O^- production by DEA in water

The study of dissociative electron attachment in water is an important step on the way to understanding electron-molecule interactions in biological matter because it represents the usual environment for those reactions in any living organism. For that reason, water has been studied intensively in theory [45, 52, 54, 55, 56] as well as in experiment [1, 10, 29, 38, 62, 99].

Several experimental groups observed O^- production in water and the ion yield curves are well established. A comparison of the O^- production cross section as a function of projectile electron energy by different groups is shown in figure 6.24. All measurements agree very well with each other and three peaks in the cross section are

[5]The electronic configuration change shows the difference between the configuration of the water molecule and the anion. In this case, in the anion there is one electron less in the $1b_1$ orbital and there are two electrons more in the $4a_1$ orbital than in the water molecule.

observed, which correspond to the three electron attachment resonances mentioned above.

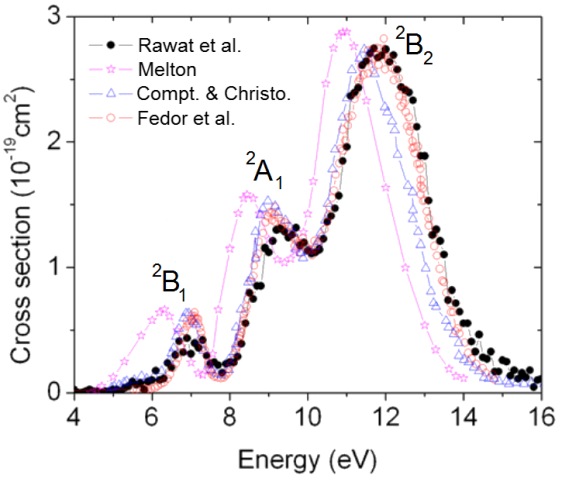

Figure 6.24: Comparison of O^- cross section as a function of projectile electron energy, measured by different groups. The different peaks are labeled with the corresponding resonances. Black dots: Rawat *et al.* [99], pink stars: Melton [75], blue triangles: Compton and Christophorou [27], orange circles: Fedor *et al.* [38]. The figure has been adopted from [99].

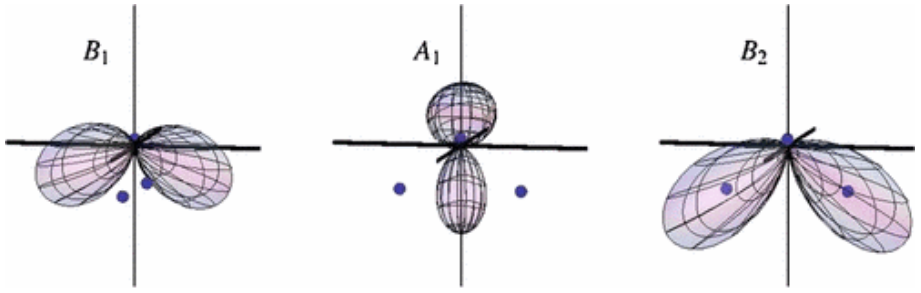

Figure 6.25: Calculations of electron attachment probabilities for all three resonances by Haxton *et al.*, using *ab initio* theoretical methods. The blue ball close to the origin is oxygen and the blue balls below the origin are the hydrogen atoms. The picture has been taken from [1].

In recent theoretical investigations of DEA in water, Haxton *et al.* calculated the dissociation dynamics of water. In their *ab initio* calculations they obtained the electron attachment probabilities for all three resonances as a function of the projectile impact direction relative to the molecule. These are depicted in figure 6.25[6]. Additionally, the O^- channel was found to originate from a symmetric dissociation, in which both hydrogen atoms are ejected simultaneously and with the same kinetic energy. Therefore, the O^- fragment is ejected along the molecular axis and it is expected to resemble the electron attachment probability. For the $^2B_2$ resonance this means that one peak at half the H-O-H bond angle (i.e. at 52°) is expected in the angular distribution of O^-. In the $^2A_1$ resonance on the other hand, two peaks are expected from the electron attachment probability if the fragment is produced in an axial recoil from the equilibrium geometry of the neutral molecule: a sharp peak around 0° and a broad peak around 180°.

Haxton *et al.* also calculated the dependence of the energy of the negative ion states on the H-O-H bond angle to investigate the dynamics of the negative parent ion. As

[6]Haxton *et al.* plot electron attachment probability different than Rescigno *et al.* did in the calculations of DEA in ammonia. Here, the direction in the figure corresponds to the direction from which the electron came and not to the direction it was traveling. When we reconstruct electron attachment amplitudes in this chapter, we will use the same definition like Haxton *et al.* to be able to compare the results.

mentioned above, the equilibrium angle depends strongly on the occupied orbitals. Figure 6.26 shows the calculated energy of the states as a function of the bond angle. Excitation of the lowest $^2B_1$ state only changes the equilibrium angle slightly. The equilibrium geometry for the $^2A_1$ state however is a linear molecule and the state is excited far from its equilibrium position. Consequently, the anion is produced in a high vibrationally excited state. In the vibration the bond angle stretches beyond 180°.

If the H-O-H bond angle is larger than 180° when the dissociation takes place, the oxygen anion is ejected opposite to the expected direction and the angular distribution of the observed fragment is inverted, creating a broad peak in the forward direction and a sharp peak in the backward direction instead. This inversion of the angular distribution was found in a momentum imaging experiment by B. Rudek [103]. Figure 6.27(a) shows a momentum image of O^- production at the $^2A_1$ resonance, obtained by B. Rudek. A broad peak in forward scattering and a narrow peak in the backwards scattering direction show that the dissociation took place after the hydrogen bond angle increased beyond 180°.

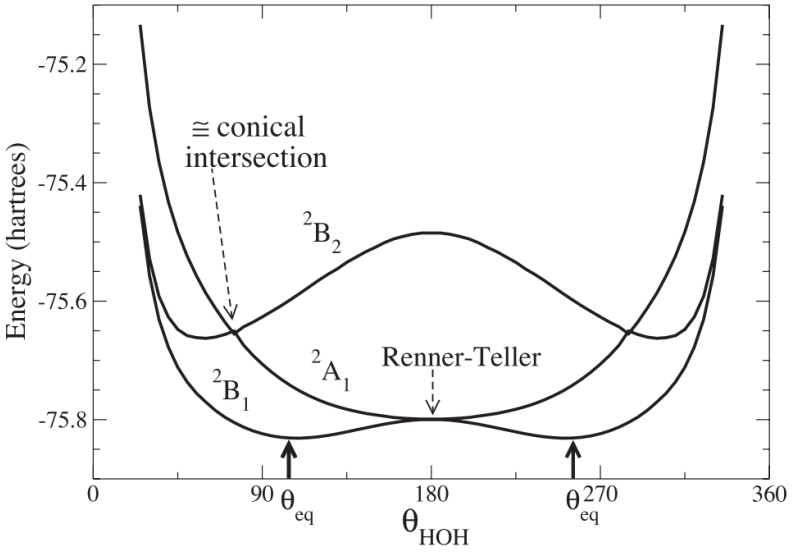

Figure 6.26: Energy of different states of the H_2O^- parent anion as a function of the H-O-H bond angle. The depicted states are the ones populated in the three resonances. The calculations were performed by Haxton *et al.* The $^2B_2$ state has a conical intersection with the $^2A_1$ state which allows a transition between both states. The figure has been taken from [54].

Figure 6.26 also shows the energy dependence of the $^2B_2$ state on the bond angle. The equilibrium bond angle in this state is lower than in the ground state water molecule. Additionally, there is a conical intersection between the potential surfaces of the $^2B_2$ state and the $^2A_1$ state at a bond angle of 76°. At this conical intersection, both states are strongly coupled and transitions between the states are possible.

Haxton *et al.* studied the dissociation dynamics on the relevant potential surfaces and found that in general the O^- production can be attributed to both 2-body dissociation and 3-body dissociation. In the $^2A_1$ resonance, the O^- fragment is only produced via the symmetric 3-body dissociation channel O^-+H+H. In the $^2B_2$ resonance however, there are contributions from both 2-body dissociation which

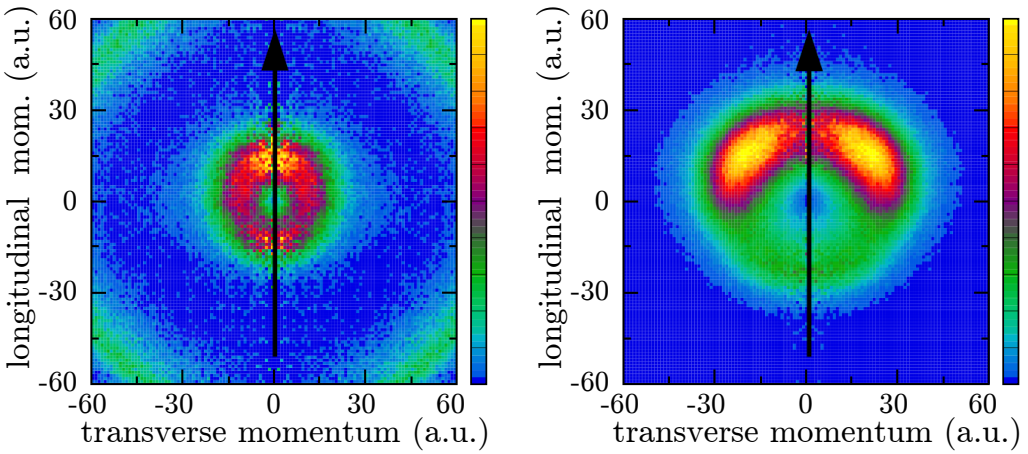

Figure 6.27: Momentum images of O^-, produced by dissociative electron attachment to water at different projectile energies: (a) $^2A_1$ resonance at an impact energy of 8.5 eV and (b) $^2B_2$ resonance at an impact energy of 11 eV. These measurements have been performed by B. Rudek [103].

produces O^-+H_2, and 3-body dissociation which produces O^-+H+H. According to the calculations of Haxton *et al.*, around 85% of the O^- yield is caused by 3-body dissociation and 2-body dissociation is only a minor contribution [56].

The change of the molecular geometry makes the O^- channel especially interesting for our studies. Since the negative fragment is ejected along the molecular axis in a symmetric 3-body dissociation, the angular distribution of this channel is unaffected by the molecular dynamics except for the inversion after the change in the bond angle in the $^2A_1$ resonance. In the dissociation leading to the production of H^- on the other hand, angular distributions would depend strongly on the H-O-H bond angle at the moment of dissociation.

Experiments in the Heidelberg DEA apparatus

The experiments mentioned above used an effusive gas beam to deliver the water to the interaction region. For momentum imaging experiments the resolution was limited by the room temperature target. In dissociation of ammonia, which was discussed in chapter 6.2, we could already show that our apparatus is able to obtain reliable momentum images for slower fragments than other apparatuses. The goal of our studies therefore was to find a possible influence of the supersonic gas jet on the dissociative electron attachment reactions and to obtain quantitatively reliable momentum images which allow us to analyze the dissociation dynamics.

The experiment was performed at the Heidelberg DEA apparatus, using the tantalum electron gun to produce the electron beam and the heated jet system to create the supersonic water jet. Deionized water was heated to 90 °C in a sealed stainless steel chamber (the bubbler) and was transported to the nozzle through heated pipes. The water gas was expanded through a large nozzle with a diameter of 100 µm to prevent clogging. Compared to the normally used 30 µm nozzle, this leads to a less efficient cooling in the expansion. Additionally, the backing pressure was determined

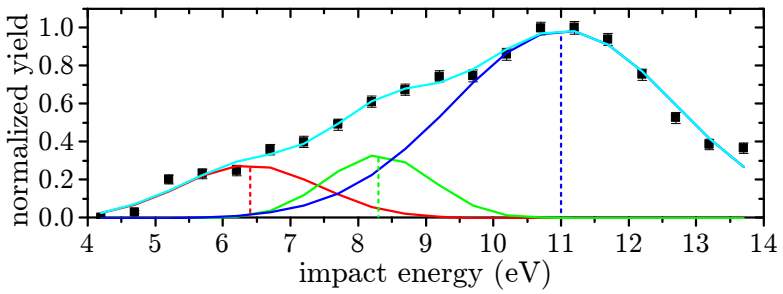

Figure 6.28: Ion yield curve for the O^- production from dissociative electron attachment in water. The curve was fitted with three Gaussian curves (red, green and blue lines), corresponding to the three resonances. The light blue line shows the sum of the Gaussians.

by the water vapor pressure of 700 mbar at 90 °C. The pressure can be increased to 1 bar when an inert gas is added to the bubbler which creates a seeded jet. At this pressure, the high flow rate through the large nozzle meant that the pumping speed was limiting the possible gas flow. Nonetheless, the conditions were sufficient to create a supersonic gas jet.

We could identify O^- as a fragment of dissociative electron attachment in the investigated energy range and a small contribution of $(H_2O) \cdot O^-$ which is created in the fragmentation of water dimers. The observation of H^- was not possible in our apparatus for technical reasons and we did not try to measure it.

The projectile impact energies in our experiments were scanned from 4 eV to 14 eV, covering the whole range in which previous experiments found dissociative electron attachment in water monomers. Our ion yield curve for O^- production in this energy range is shown in figure 6.28. In our ion yield curves, the three resonances are less well separated than in the measurements of other groups, which were shown in figure 6.24. The broad peaks in our experiment are the result of a very low electron energy resolution. Although the energy resolution was checked periodically and showed a low energy spread of 300 meV before these measurements were performed, some unknown factors led to a much poorer energy resolution than expected. One possible origin of high energy spread may be deposition of water atoms on the tantalum photo-cathode, changing the work function of the material. To find the energy of maximum yield for all resonances in this measurement, we fitted the ion yield curve with three Gaussian functions. The Gaussians for the production of O^- from the water monomer are centered at 6.4 eV ± 1.1 eV ($^2B_1$ resonance), 8.3 eV ± 0.6 eV ($^2A_1$ resonance) and 11.0 eV ± 0.2 eV ($^2B_2$ resonance). These values are in agreement with results from other groups but especially the position of the $^2B_1$ resonance has a very high uncertainty.

When different DEA resonances are overlapping in the projectile energy, we can generally use the momentum imaging capability of our apparatus to distinguish different resonances. In the present case, it was possible to separate the $^2A_1$ resonance from the $^2B_2$ resonance, which can be seen in figure 6.29. The kinetic energy (and momentum) of O^- which is produced in the $^2B_2$ resonance at impact energies between 10 eV and 12 eV is significantly higher than the kinetic energy of O^- from the $^2A_1$ resonance below 10 eV impact energy. In our momentum imaging experiments we were however unable to observe the $^2B_1$ resonance (not shown in the figure). The

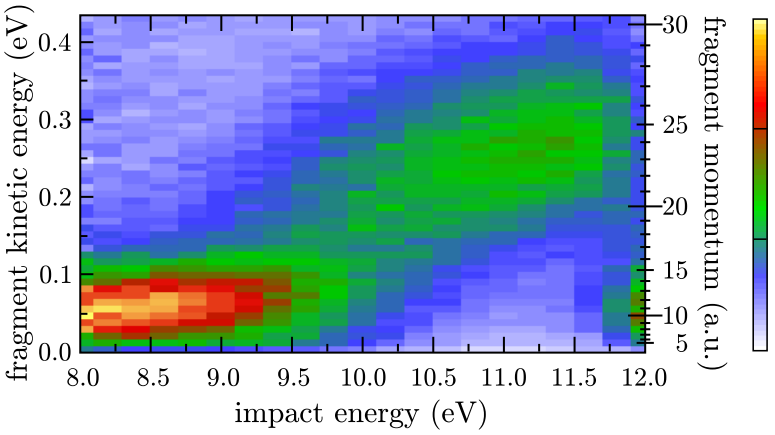

Figure 6.29: Kinetic energy and absolute value of the momentum of the O^- fragment in dissociative electron attachment to water are shown as a function of the electron impact energy. The $^2A_1$ resonance which yields a low kinetic energy can be distinguished from the $^2B_2$ resonance, leading to higher kinetic energy in the detected fragment.

$^2B_1$ peak showed a much lower yield in earlier studies and is indistinguishable from the $^2A_1$ peak in our experiment due to the broader resonance peaks and the low kinetic energy of the fragment in both resonances.

For the production of O^- via the $^2A_1$ resonance and the $^2B_2$ resonance, we recorded the ion momenta and reconstructed the momentum images using the Abel inversion method. The Abel inversion was necessary to improve the statistics as compared to using a slice through the momentum sphere. The momentum images and and angular distributions for both resonances are shown in figure 6.30. The momentum image of the $^2B_2$ resonance at a projectile energy of 11 eV in figure 6.30(b) shows some contribution at low momenta because it overlaps with the $^2A_1$ resonance in our measurement. Since they are separated by their momenta however, the angular distribution of the O^- fragment from the $^2B_2$ resonance in figure 6.30(d) could be reconstructed by selecting only events with high momentum.

Discussion of the $^2A_1$ resonance

The angular distribution of O^- created in the $^2A_1$ resonance is shown in figure 6.30(a) for an electron impact energy of 8.5 eV. It shows a very broad peak in forward scattering direction and a sharp peak in the backwards direction. This distribution is consistent with the observations by B. Rudek [103], which are shown in figure 6.27(a).

The theoretical calculations which were performed by Haxton *et al.* were explained above. They calculate the differential electron attachment probability, i.e. the angular distribution of the electron attachment probability. They then used the axial recoil model to create the expected angular distributions of the ion created in the dissociation and found that the experimental distribution is the inversion of the theoretical predictions. Additional dynamics, which were also found by Haxton *et al.* can explain the measured angular distribution of the O^- fragment. Instead of ejecting the hydrogen atoms along the equilibrium bond direction, the hydrogen bonds scissor back to the opposite side of the molecule in a symmetric vibration motion prior to dissociation. The situation is depicted in figure 6.31. The O^- ion is ejected opposite of the direction which would be expected from an axial recoil model, which

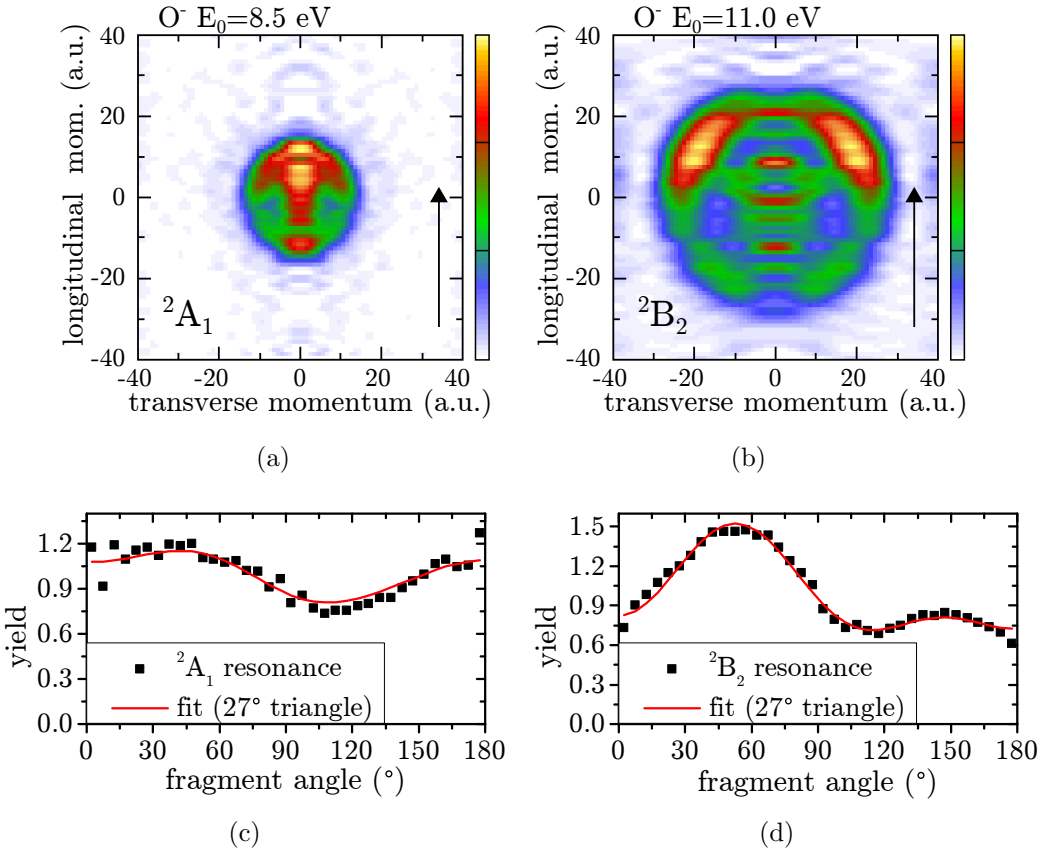

Figure 6.30: Momentum images for production of O^- from water at (a) 8.5 eV ($^2A_1$ resonance) and (b) 11 eV ($^2B_2$ resonance) and the corresponding angular distributions of those resonances: (c) $^2A_1$ resonance, (d) $^2B_2$ resonance. The images are obtained by applying an Abel inversion to the projection of all momenta on the plane containing the electron impact direction (black arrow) and the time-of-flight direction. Red lines in (c) and (d) show the results of a partial wave fit including an experimental spread of the electron impact direction, a triangular distribution with a width of 27°.

leads to the inversion of the distribution. This internal dynamic happens independently of the electron attachment direction.

Our momentum image of O^- production in the $^2A_1$ resonance in figure 6.30(a) can be compared to the measurement of B. Rudek which is shown in figure 6.27(a). The shape of both distributions is in good agreement but the sizes of the distributions are different. While the experiments of B. Rudek show the maximum of the absolute momentum at 15 a.u., our measurements show a smaller momentum of 11 a.u. for the same electron impact energy as in their experiment, namely 8.5 eV. This corresponds to a change in the kinetic energy of the fragment by a factor of two, from 105 meV in the earlier experiments to 56 meV in our measurements. The change in kinetic energy is similar to the one found for the NH_2^- fragment in the ammonia experiments between our measurements and the results of other groups which all use an effusive gas beam (cf. section 6.2). The overestimation of the kinetic energy for slow and heavy fragments seems to be a common source of error for setups which deliver the target gas via an effusive gas beam. For the ammonia fragment we could show that our lower kinetic energy results are consistent with other measurements as well as with theory and that other experiments overestimated the kinetic energy.

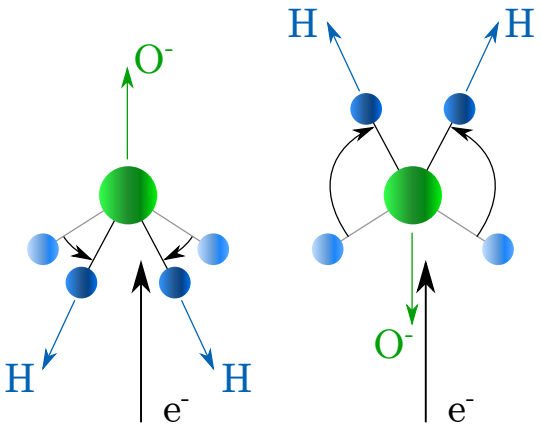

Figure 6.31: Influence of the molecular dynamics on the angular distribution of the O^- fragment (green). Left: In this example, O^- is emitted in forward direction when the hydrogen bonds break at a H-O-H bond angle below 180°. Right: O^- is emitted in the opposite direction when the hydrogen bonds break at a H-O-H bond angle above 180°. The light blue balls show the equilibrium position of the hydrogen atoms and the dark blue balls show their positions during the dissociation.

We therefore are confident that the new kinetic energy which was measured in our experiment is more accurate than the earlier measurements.

Discussion of the $^2B_2$ resonance

Although theoretical calculations predict both 2-body and 3-body dissociation at the investigated electron energy of 11 eV, we do not find signatures which allow us to distinguish two different processes. It can be expected that both processes would not produce O^- ions with the same kinetic energy. As can be seen in figure 6.29 though, there is only one peak in the kinetic energy spectrum in the range of the $^2B_2$ resonance (10 eV to 12 eV impact energy). According to the calculations of Haxton *et al.* [56], the 2-body dissociation produces only 15% of all O^- events and the yield might be too low to be recognized in our experiments. The contribution of 2-body dissociation will therefore be neglected in the discussion of the kinetic energy distribution. The additional low kinetic energy peak which is visible at the highest measured projectile energy of 12 eV is an artifact from the energy scanning process in the experiment and should be ignored.[7]

The 3-body dissociation occurs in a symmetric process. The H-O-H bond angle decreases as it is sketched in the left part of figure 6.31 because the equilibrium geometry of the negative parent ion has a smaller bond angle. The symmetric dissociation means that both hydrogen atoms are ejected at the same angle with respect to the rotational axis of the water molecule and with the same energy. Using energy and momentum conservation it is possible to calculate the total kinetic energy release of the dissociation as a function of the H-O-H bond angle from the kinetic energy of the O^- fragment. At an electron impact energy of 11.5 eV we observe an O^- momentum of 24 a.u., which corresponds to a kinetic energy of the O^- fragment of 270 meV. The summed bond dissociation energy for the two O-H bonds is 9.565 eV [12] and the electron affinity of the oxygen atom is 1.465 eV. This gives an excess energy in this reaction of 3.4 eV which is equal to the kinetic energy release. When the O^- fragment has a kinetic energy of 270 meV, the kinetic energy release of 3.4 eV is reached with a H-O-H bond angle of 68°. This angle is substantially lower than the equilibrium angle of 104.5° and shows that the geometry of the parent ion changes

[7] This has been checked in an additional measurement up to higher energies. When switching the electron energy back from the highest to the lowest value, the whole energy range is sampled, showing the low kinetic energy peak of the $^2A_1$ resonance at the highest investigated energy.

prior to dissociation. In figure 6.26 the energy of the different states of the parent ion was shown as a function of the H-O-H bond angle. For the $^2B_2$ state, the energy curve has its minimum around 58°, close to the observed bond angle.

The experimental kinetic energy distribution of the O^- fragment is quite broad, as can be seen in figure 6.29. In the calculation of the H-O-H bond angle from the kinetic energy, this leads to a broad distribution of possible bond angles with a FWHM of 38°. This width is influenced by the experimental momentum resolution. The initial momentum spread of the water in the jet and the size of the interaction region restrict this resolution and are responsible for the measured width of the kinetic energy of the fragment. We expect the distribution of H-O-H bond angles at which the dissociation takes place to be much narrower than the calculated FWHM of 38°.

The angular distribution of O^- produced in the $^2B_2$ resonance was investigated as well. A momentum image which was acquired at an electron impact energy of 11 eV is shown in figure 6.30(b). It can be compared to the corresponding momentum image, which was measured by B. Rudek at the same impact energy, in figure 6.27(b) and both measurements show good agreement. The angular distribution in our measurement shows a pronounced peak at 55° and a second smaller peak at 145°. This is also in general agreement with the calculations by Haxton *et al.* for the attachment probability in this resonance [52], which is shown in figure 6.25. Their calculations show that electron attachment happens preferentially along the O-H bond axis which results in a preferred O^- direction of 52° from the electron beam.

The additional peak which we observed at 145° is not predicted from the electron attachment probability by Haxton *et al.* Our calculation of the H-O-H bond angle during dissociation showed that the bond angle decreases prior to dissociation. During this change, the molecule passes a geometry at 76°, at which the molecular dynamics can be influenced by the presence of the conical intersection between the $^2B_2$ state and the $^2A_1$ state. If the parent ion undergoes a transition from the $^2B_2$ state to the $^2A_1$ state at this point, the dynamics of in the $^2A_1$ state can occur. Then, the new equilibrium geometry is a linear molecule and the H-O-H bond angle can stretch beyond 180°. The angular distribution of the O^- fragment in this case is inverted compared to the original distribution. The position of the main peak should then be mirrored around 90°, i.e. the backward peak would have to be observed at 125° instead of 145°. The difference between the experimental position of the backwards peak and the position at which it should occur if it is caused by the described molecular dynamics is large enough that we can distinguish them. Therefore we conclude that it is more likely that the electron attachment probability has a small contribution for attachment at other angles which was not predicted by the calculations of Haxton *et al.*

Reconstruction of electron attachment probabilities

The O^- anion which is produced in symmetric dissociation has the advantage that it is ejected along the main axis of the molecule. Its angular distribution does not change even when the hydrogen molecules change their position as described above. The only possible change in the direction of the O^- happens when the hydrogen bond angle is increased beyond 180° and the anion is ejected in the opposite direction in the $^2A_1$ resonance. Assuming the angular distribution is otherwise unchanged,

we can employ the partial wave expansion to fit the observed angular distribution even though the molecular shape changes in the dissociation. In figure 6.30(d) it is clearly visible that the distribution is not zero at 0° and 180°. For a $^2B_2$ resonance, attachment along the main axis of the molecule is forbidden and the yield for those angles is expected to vanish. Our experiment however has a finite angular resolution. We use slow electrons and guide them using a strong magnetic field which results in a circular motion of the electrons around the magnetic field lines. In the tantalum electron gun which we used in this experiment there are also no apertures to block electrons which are off-axis. Due to this electron steering mechanism, electrons can hit the target at an angle which differs from the expected direction[8]. We model this effect by assuming a triangular distribution with a width of 27°. This is the minimum width necessary to fit the observed angular distribution with a $^2B_2$ resonance. We approximate the electron impact direction as a triangular distribution to keep the main part of the electron beam on the axis and at the same time set a maximum deflection angle. In the experiment, the highest possible deflection depends on the magnetic field and the electron energy.

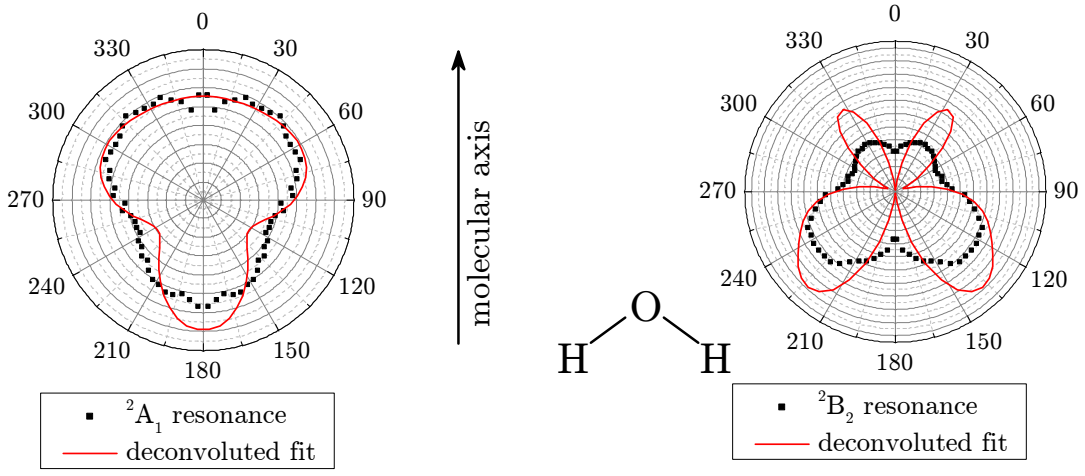

(a) (b)

Figure 6.32: Reconstruction of the expected angular distributions (red lines) for the two investigated resonances (a) $^2A_1$ and (b) $^2B_2$. These results are the deconvolution of the observed momenta where a spread in the electron impact direction was taken into account in the fit and removed to obtain the deconvolved distributions. These distributions correspond to the electron attachment probabilities after integration over the rotation around the molecular axis.

Using the partial wave distributions which we obtained when accounting for the impact direction spread of the electrons, we can reconstruct the angular distributions without the limited angular resolution. The reconstructions based on the fits are shown in figure 6.32 for both the $^2A_1$ and the $^2B_2$ resonance. While for the $^2A_1$ resonance the influence of the limited resolution on the angular distribution is low, for the $^2B_2$ resonance, the sharp minima are filled up.

[8] In the GaAs electron gun, which was used in the electronic excitation experiments and for DEA in ammonia, several apertures block the electrons which are too far off-axis. This selection process leaves only electrons which are aligned with the magnetic field. Therefore, the angular spread could be neglected in the previously discussed momentum imaging experiments in ammonia.

The reconstructed distributions show the electron attachment probability, integrated over all possible rotations around the main axis of the molecule. The dependence of the electron attachment probability on the angle between the incident electron and the main axis of the molecule is preserved in this process. The distributions can be compared to the electron attachment probabilities which were calculated by Haxton *et al.* and which are shown in figure 6.25. In the $^2A_1$ resonance we obtain a very similar electron attachment probability compared to the one by Haxton *et al.* except for an additional isotropic contribution. In the $^2B_2$ resonance our reconstructed electron attachment probability shows an additional lobe at an angle of 145° from the molecular axis which was not predicted in the *ab initio* calculations by Haxton *et al.*

DEA in water dimers

While most experimental studies so far used effusive gas beams which cannot produce clusters, one study by Klots *et al.* was performed in a supersonic jet [62]. In their gas jet they had a mixture of water monomers and dimer and they were able to observe the production of $(H_2O) \cdot O^-$ from a water dimer. In our supersonic jet, the low pressure, large nozzle and high temperature are factors which decrease the amount of clustering. Therefore in our experiments we only observe a very low degree of clustering and the $(H_2O) \cdot O^-$ channel is barely visible.

Figure 6.33 shows a comparison of our ion yield curves for O^- from the water monomer and $(H_2O) \cdot O^-$ from the water dimer in (a). In (b), the corresponding ion yield curves by Klots *et al.* for the same channels are shown. The two channels both correspond to the loss of two hydrogen atoms. In the case of O^-, the parent molecule was a monomer and in the case of $(H_2O) \cdot O^-$ the parent molecule was a dimer.

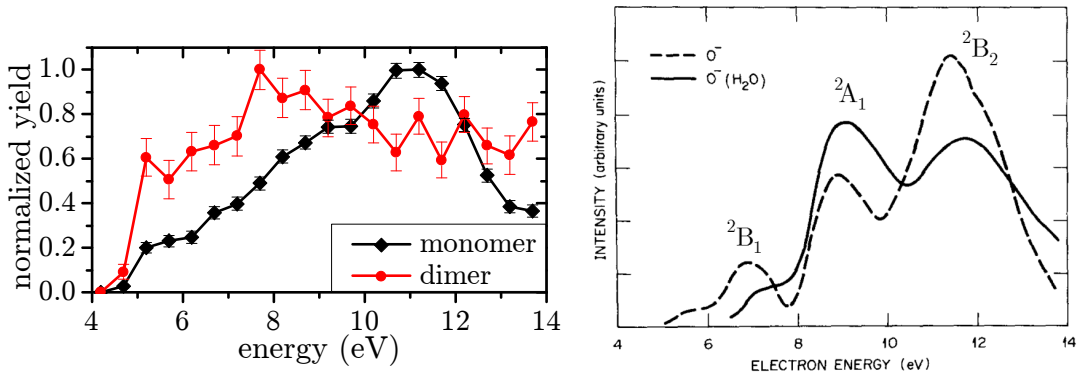

(a) (b)

Figure 6.33: Dissociative electron attachment resonances in water monomers and dimers (a) in our own experiment and (b) the results of Klots *et al.* Both curves show the channel which corresponds to the loss of two hydrogen atoms, i.e. O^- for the monomer and $(H_2O) \cdot O^-$ for the dimer. The graph in (b) is taken from [62].

Our low statistics and low energy resolution mean that single resonances are not visible in our ion yield curve for $(H_2O) \cdot O^-$. Nonetheless, it is visible that the $^2A_1$ resonance around 8 eV becomes more prominent in the dimer as compared to the

monomer. A similar ion yield for the $(H_2O) \cdot O^-$ channel was observed in the study by Klots *et al.*, however they did not have an explanation for their observations. We want to propose an explanation for the increased yield in the $^2A_1$ resonance, compared to the $^2B_2$ resonance. In both cases, the dissociation process is similar to the dissociation in the monomer, which we investigated and discussed above. In the water dimer, both molecules are connected by a hydrogen bond with a bond dissociation energy of around 200 meV [39]. This energy has to be compared to the kinetic energy which the O^- fragment gains in the dissociation. The kinetic energy of the O^- fragment was already shown in figure 6.29. In the $^2A_1$ resonance, the most likely kinetic energy of the O^- fragment is 60 meV. In the water dimer, this is not sufficient to break the hydrogen bond and the $(H_2O) \cdot O^-$ fragment is stable. In the $^2B_2$ resonance however, the measurements in the monomer showed that the O^- fragment is produced with a kinetic energy around 270 meV. In the dimer this is enough to break the hydrogen bond and the $(H_2O) \cdot O^-$ fragment is unstable. Therefore, in the $^2B_2$ resonance dissociative electron attachment in the dimer produces the O^- fragment via the same channel as the $(H_2O) \cdot O^-$ fragment and the total yield of the $(H_2O) \cdot O^-$ fragment is decreased.

6.5 DEA in heterocyclic organic compounds

Many biologically relevant molecules include heterocyclic organic compounds, carbon rings in which one or more members of the ring are of another atomic species, usually nitrogen or oxygen. These molecules can be found in DNA bases, sugars and many other places. Due to their importance, studying the dissociation processes of several representatives of this class of molecules can give insight into the factors which influence the dissociation. We investigated dissociative electron attachment in furan and pyridine. While DEA in furan has been investigated using mass spectrometry in the past [115], no momentum imaging has been performed so far and for pyridine there were no experiments on DEA at all.

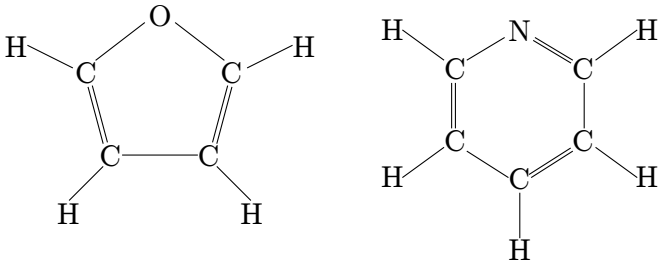

Figure 6.34: Molecular structure of the investigated heterocyclic organic compounds: (a) furan, (b) pyridine.

6.5.1 Furan

The group of Illenberger *et al.* reported dissociative electron attachment to furan (mass: 68 amu) resulting in a number of different fragments [115]. Most of the fragments arise from ring-breaking channels, in which the molecular shape is drastically changed and 3-body dissociation might be possible. So far, the dynamics of the dissociation have not been studied in detail.

The mass spectrometric analysis of anionic fragments by Illenberger *et al.* is shown in figure 6.35. They observed a DEA resonance in a region around an electron

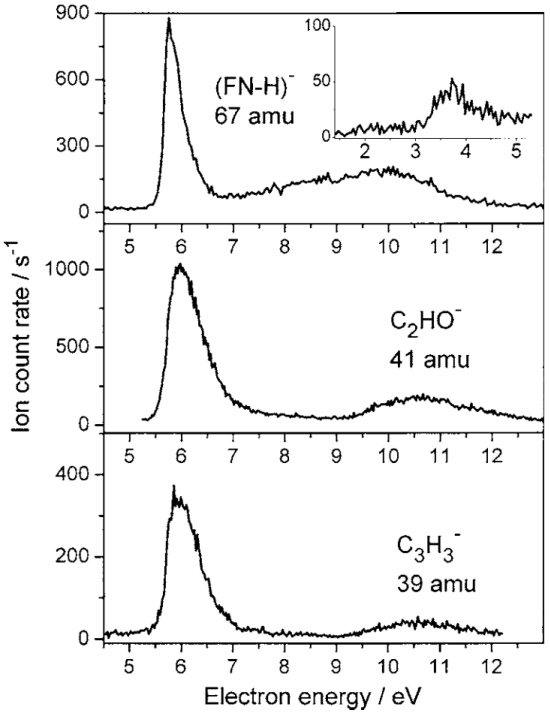

Figure 6.35: Ion yield curves for the most abundant fragments in the dissociative electron attachment to furan, measured by the Illenberger group [115]. A resonance around an electron energy of 6 eV produces many different fragments. Our own momentum imaging experiments were performed at this resonance.

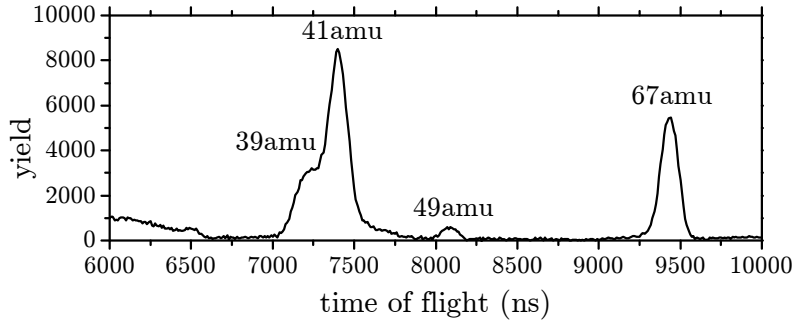

Figure 6.36: Time-of-flight spectrum for dissociative electron attachment in furan at an electron impact energy of 6.2 eV. A constant background has been subtracted in this graph.

impact energy of 6 eV, which they assigned to a core-excited state of the parent anion. Dissociation at this energy leads to the production of several different anionic fragments. Therefore, we chose the same energy range for our momentum imaging experiments and performed the ion momentum measurements at an impact energy of 6.2 eV, where we observed the highest fragment yield. The time-of-flight spectrum at this impact energy is shown in figure 6.36. We can identify fragments of mass 39 amu, 41 amu, 49 amu and 67 amu. The time-of-flight spectrum was obtained using the high mass resolution mode of the spectrometer, which was described in section 4.1. Only in this mode we were able to distinguish the time-of-flight peaks of the fragments with masses 39 amu and 41 amu. Our DEA experiments in furan were performed at the Heidelberg DEA apparatus, using the GaAs photoemission electron gun.

Illenberger *et al.* identified several other, lighter fragments. We can not observe them due to background contamination in our experiment. This background is generally very low, therefore it did not have to be considered in DEA measurements of other molecules. In the case of furan however, the DEA cross section is very low as well.

While it is not straightforward to measure absolute cross sections in our setup, we compared the anion yield in furan to our previous ammonia measurements and found that the yield was lower by about two orders of magnitude.

The furanide anion

The fragment at 67 amu is the closed shell furanide anion which is created by loss of a neutral hydrogen after electron attachment and which we will denote $(FN\text{-}H)^-$. The high mass ratio between the anion and the lost hydrogen means that almost all of the kinetic energy (67/68 or 98.5%) will be carried by the hydrogen atom. This fragment was investigated separately from the other fragments at an impact energy of 5.5 eV and in the low mass resolution mode of the spectrometer. Using this mode increases the momentum resolution for this fragment. We determined the energy of the anion to be 10 meV±5 meV, i.e. the total kinetic energy release of the reaction is 760 meV±380 meV. Those values have been obtained from the momentum images, using the momentum of highest yield to calculate the kinetic energy. The momentum images are shown in figure 6.37.

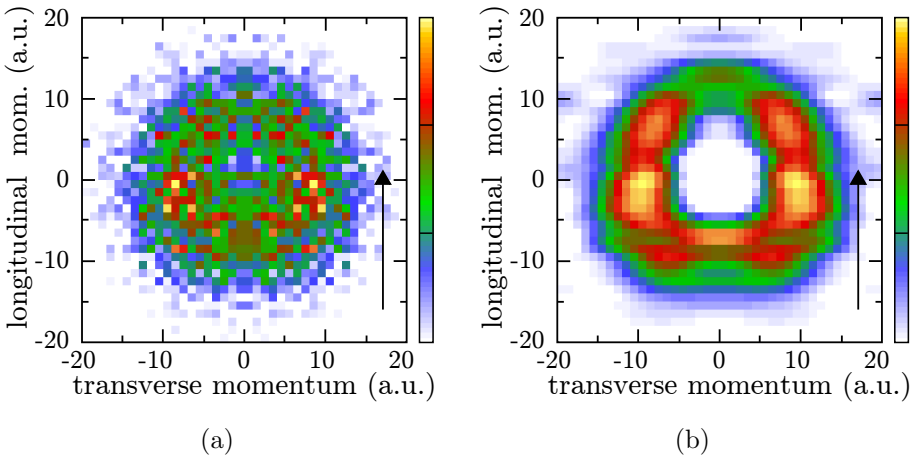

Figure 6.37: Momentum images for production of the closed shell anion $(FN\text{-}H)^-$ from furan at 5.5 eV. (a) projection of all momenta in a plane containing the electron impact direction (black arrow), (b) Abel inversion showing the reconstructed momentum distribution in this plane.

Due to the low energy of the fragment, the momentum and kinetic energy distributions appear very broad. This is a result of the size of the interaction region and the initial thermal momentum distribution, combined with the low deflection of the heavy anion. When the measured momenta are used to calculate the kinetic energy for every event, as a result of the finite momentum resolution the obtained kinetic energy distribution will be shifted towards higher energies. The kinetic energy gets overestimated because of the higher influence of the large momenta. Nevertheless, even with the resulting broad distribution, almost all dissociation events show a kinetic energy release below 1.5 eV. The bond dissociation energy of the C-H bond in furan is 5.2 eV and the electron affinity of the furanide radical (C_4H_3O) is 1.85 eV [126], yielding a reaction enthalpy of 3.35 eV, which is shown in figure 6.41(a). At the projectile energy of 5.5 eV which was used in the experiment this results in an excess energy of 2.15 eV. We clearly observe a kinetic energy release lower than the

excess energy. Therefore, the furanide anion has to be produced in vibrationally excited states with an average vibrational energy of 1.4 eV.

The angular distribution for the $(FN\text{-}H)^-$ fragment was obtained in an event-based analysis from the data as well as from the Abel inversion of the projection of all data. This analysis by two different methods is performed for several reasons. First of all, the event-based calculation should represent the correct distribution but due to the low statistics the errors are quite high. This problem is less severe when using the momentum distribution created in an Abel inversion of the projection of all events into the x-z-plane[9], because it yields a smooth function. On the other hand the result of the Abel inversion strongly depends on the choice of the cutoff frequency (cf. section 4.3), especially when starting with noisy data as it is the case here. The angular distributions obtained with both methods are shown in figure 6.38. The angular distributions obtained in the event-based analysis and the analysis using the Abel inversion are in excellent agreement, showing that the result of the Abel inversion is consistent with the original data. The angular distribution of the $(FN\text{-}H)^-$ fragment consists of a very broad peak with a maximum around 100°.

The $(FN\text{-}H)^-$ fragment can be created by loss of a hydrogen on the side of the oxygen, or on the side opposite to the oxygen (cf. figure 6.34), leading to different hydrogen ejection angles with respect to the rotational symmetry axis of the molecule. Assuming that there is no rearrangement in the internal structure of the molecule, we can use the partial wave expansion to recreate the angular distribution. This assumption is reasonable because the carbon-oxygen-ring which makes up the main structure of the molecule is unaffected by the hydrogen loss. Due to the broad peak and a low amount of structure in the angular distribution however, it is not possible to identify both the symmetry of the state after electron capture and the position of the ejected hydrogen simultaneously. The observed angular distribution can be reproduced with several combinations of symmetry and position of the ejected hydrogen. We can however exclude electron capture into a B_2 state of the parent anion for both positions of the ejected hydrogen as well as loss of hydrogen from the oxygen side if the electron is captured into a parent state of A_2 symmetry because these cases cannot reproduce the observed angular distributions. Since we used the GaAs electron gun in these experiment we assumed the electron impact direction to be constant and did not include a distribution of impact directions in the partial wave fits.

A currently ongoing *ab initio* theoretical study by dos Santos *et al.* using complex Kohn scattering calculations is investigating DEA in furan. Their calculations so far predict a DEA resonance of A_2 symmetry at 6 eV impact energy which leads to hydrogen loss from the side opposite to the oxygen [33]. This is in agreement with our findings, since our observed angular distribution allows this process.

Additional information could be obtained in further measurements using partially deuterated furan, which was not done in the present work. When the hydrogen atoms on the oxygen side of the molecule are replaced by deuterium, the mass of the fragment will allow a distinction of hydrogen (or deuterium) loss from different

[9] The x-direction is the direction of the incoming electron and the z-direction is the time-of-flight direction. The resulting plane is perpendicular to the gas jet direction and yields the best momentum resolution in our setup.

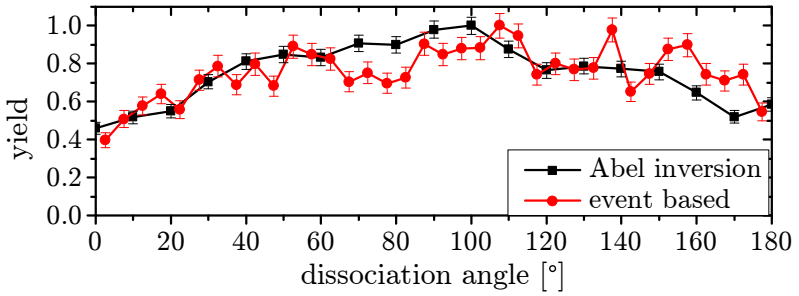

Figure 6.38: Angular distribution of the closed shell anion $(FN\text{-}H)^-$ created in DEA of furan at 5.5 eV impact energy. The results are obtained directly from the measured distributions as well as from the Abel inversion of the projection of all events on the plane normal to the jet direction.

positions. An additional advantage in the use of deuterated molecules in momentum imaging experiments will be the higher kinetic energy of the negative ion due to the lowered mass ratio of the fragments, which results in a better momentum resolution.

Ring-breaking channels

All other fragments which are created by DEA in furan are ring-breaking channels in which at least two bonds have to be broken. They are accompanied by nuclear rearrangement within the fragments when they relax towards a new equilibrium geometry. In general, ring breaking channels can yield fragments in high vibrational states after the rearrangement and they are expected to be slow processes compared to a single bond cleavage which leads e.g. to the hydrogen loss channel. Those factors generally result in negative ions with low kinetic energy, because only a small fraction of the excess energy is converted to kinetic energy. Furthermore, these channels will produce fragments with an isotropic angular distribution if the dissociation is slow compared to the rotation of the molecule. In this case, any possible dependence of the attachment probability on the orientation of the molecule will be lost in the rotational averaging.

The momentum imaging for the ring-breaking channels was performed in the high mass resolution mode of the spectrometer which compressed the width of the time-of-flight distributions due to the fragment momentum in this direction. We used the 2D-projection of the momenta and reconstructed the momentum images using the Abel inversion. In the case of the 39 amu and 41 amu fragment, their time-of-flight distributions overlap even in this mode, which is shown in figure 6.39. The region in which the distributions overlap is limited to the time-of-flight range between the dotted lines. Only events with lower time-of-flight are used for the 39 amu fragment. This corresponds to scattering of the ions in only one hemisphere, in this case left from the point of view of the incoming electron beam. This part of the distributions still includes all information. In the same way, only events with high time-of-flight are used for the 41 amu fragment.

In most cases, momentum images show no structure, as it is the case e.g. for the 41 amu fragment ($HCCO^-$) and the 49 amu fragment (C_4H^-) . The momentum images for these fragments are depicted in figure 6.40(b) and (c). They show broad momentum distributions with their maximum at zero. The broad momentum distributions do not imply high kinetic energy release because - if they were to be

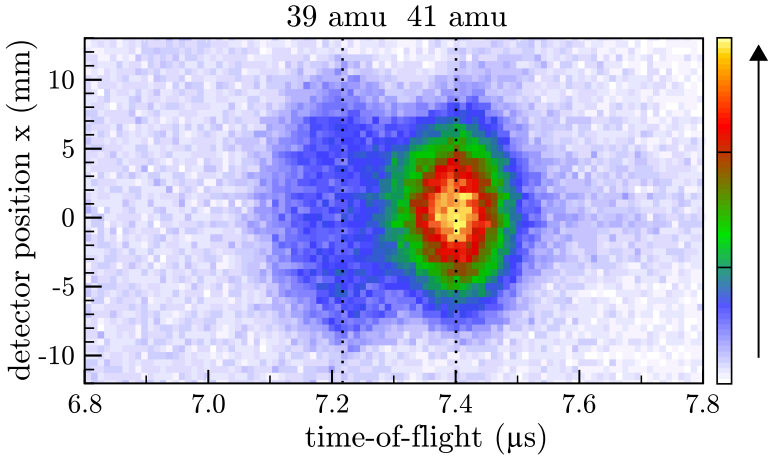

Figure 6.39: Distribution of the positions of recorded events along the electron impact direction x as a function of the time-of-flight. From this raw data, the partial overlap between the 39 amu and 41 amu fragment is visible. The black arrow shows the direction of the incident electron beam.

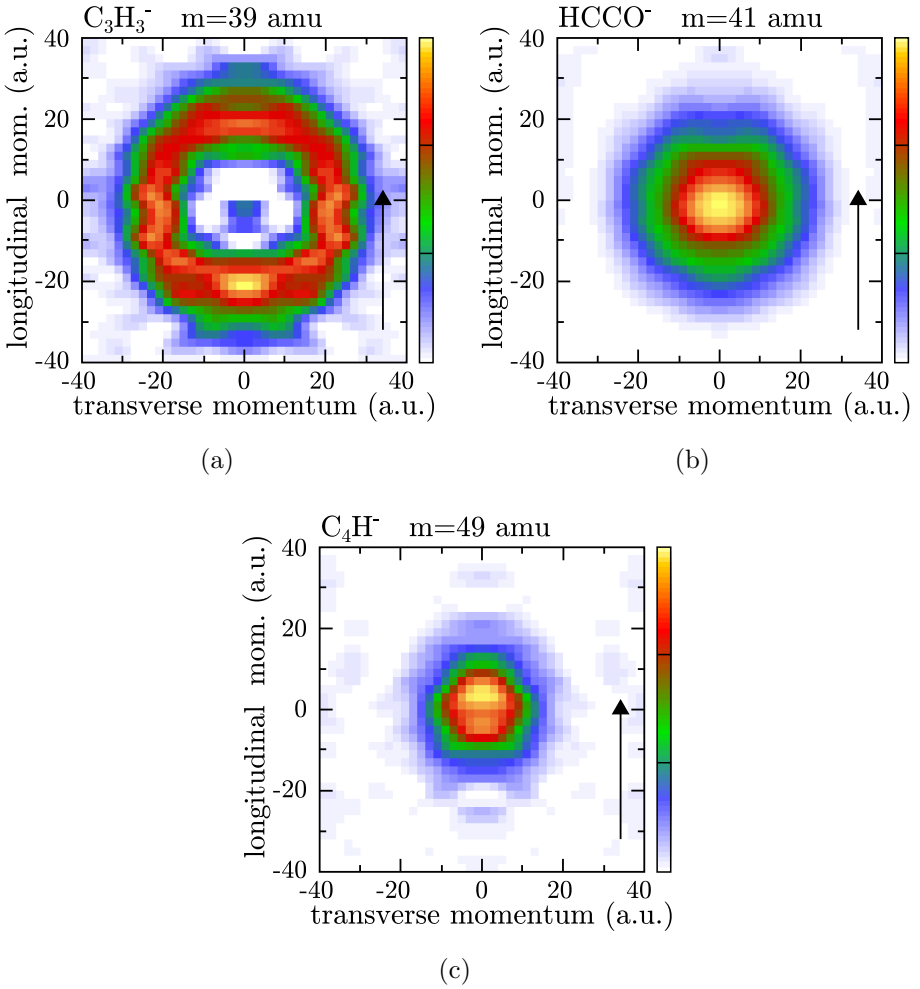

Figure 6.40: Momentum images for production of the fragments (a) $C_3H_3^-$, (b) $HCCO^-$ and (c) C_4H^- created in DEA of furan at 6.2 eV. The results are obtained from the Abel inversion of the projections of all momenta onto the detector plane.

created in a 2-body dissociation - the measured fragments would carry 40% (41 amu fragment) and 28% (49 amu fragment) of the released kinetic energy. Therefore, the overall kinetic energy release for a 2-body dissociation would be below 50 meV in both cases and almost all of the excess energy would be stored in internal degrees of freedom. The kinetic energy distributions will be discussed separately at the end of this section.

The only ring-breaking channel to result in a fragment with a considerable amount of kinetic energy is the 39 amu channel, producing $C_3H_3^-$. The momentum image of this fragment is shown in figure 6.40(a). This fragment is produced by breaking a C-O bond and a C=C bond but no hydrogen bond is broken. It is therefore likely that this fragment is created in a 2-body dissociation, resulting in the kinetic energy of 90 meV for this fragment and a total kinetic energy release of 220 meV. On the other hand the angular distribution is essentially isotropic, as can be seen from the momentum image. This suggests that the dissociation is slow and takes at least as long as the rotation of the molecule.

For ring-breaking channels it is also possible that the molecule dissociates into three or more fragments. We will explore this process by checking if 3-body dissociation is energetically accessible at the investigated impact energy of 6.2 eV.

The $C_3H_3^-$ fragment

The production of the 39 amu fragment $C_3H_3^-$ can be explained by a 2-body dissociation. The reaction path is shown in figure 6.41(b). By breaking two bonds in the ring, the fragments HCO and C_3H_3 can be produced which requires an energy of 4.4 eV [108]. The C_3H_3 radical has an electron affinity of 0.9 eV [83]. The total required energy therefore is only 3.5 eV. In our measurement at an impact energy of 6.2 eV this leaves an excess energy of 2.7 eV which is much higher than the measured kinetic energy release of 200 meV. Thus, 2.5 eV must be left as internal energy of the fragments. Although this reaction can be explained by a 2-body dissociation, it is very likely that the neutral fragment dissociates further because the binding energy of the hydrogen in the HCO radical is only 0.65 eV [12]. Unless most of the 2.5 eV internal energy is stored in the anion, the vibrational excitation energy of the neutral will be above the dissociation limit. However this neutral dissociation will only happen in a subsequent step after the dissociative electron attachment and has to be treated as a separate reaction. It therefore has no influence on the kinetic energy release in the DEA.

The $HCCO^-$ fragment

In the dissociation leading to formation of the 41 amu fragment ($HCCO^-$), three bonds have to be broken: a C-O bond, a C-C bond and a C-H bond, leaving three fragments. It is not necessary to know the exact dissociation dynamics or the reaction path, since we are only interested in the energy difference between the furan molecule and the products. Our choice of the used dissociation path to calculate the energy difference is governed by the available dissociation energy data. To calculate the energy necessary for creating those fragments we handle the dissociation in three steps, which are illustrated in figure 6.41(c). The first step is the dissociation of furan into C_2H_2 and CH_2CO, increasing the energy of the products by 2.14 eV compared to the ground state of the parent molecule [108]. We view the dissociation

of CH_2CO into HCCO and H as the second step, which requires another 4.55 eV [12]. The last step is electron attachment to the HCCO radical, which has an electron affinity of 2.35 eV [84]. This yields an energy difference of 4.34 eV between furan and the three fragments which is well below the available energy of the projectile electron and therefore it is an energetically accessible reaction. The neutral C_2H_2 fragment is a stable molecule which makes it very unlikely that it reacts further with the H radical which is produced on the other side of the former furan molecule. We conclude that the $HCCO^-$ ion is produced in a 3-body dissociation, creating the neutral fragments H and C_2H_2.

The C_4H^- fragment

To produce the 49 amu fragment (C_4H^-), both C-O bonds as well as three C-H bonds have to be broken, so it is possible that this channel also creates more than two fragments. Due to the lack of data for required bond dissociation energies in furan and its fragments, we are unable to calculate the precise energy necessary for the dissociation. Instead, we have to use bond dissociation energies for similar molecules or dissociation from a similar part of a different molecule as a reference for possible bond dissociation energies to give a rough estimate of the required energy. Again we use a dissociation path which might not be the physical one but which provides some known bond dissociation energies. The reaction path is illustrated in figure 6.41(d). The first step is the opening of the furan ring by breaking a C-O bond. We estimate a bond dissociation energy of 3.6 eV for this process[10]. Next, the remaining C-O bond is broken, requiring about 3.9 eV[11]. We now consider the dissociation of the C-H bonds in the remaining C_4H_4 molecule. If no change in the structure occurs, the fragment has one hydrogen bound to every carbon atom, making this molecule a double radical with an unpaired electron at the first and the last carbon atom. Severing the C-H bond at those positions takes about 3.6 eV each[12]. At this point, one more hydrogen atom has to be ejected from the remaining C_4H_2 fragment for which the bond dissociation energy is unknown. Again, we are interested in deciding if the energy available in the reaction is sufficient to lead to many-body decay. Therefore, we can ignore the dissociation energy of the last hydrogen for now, knowing that we obtain a lower bound for the required energy. By now, the bond dissociation energies already sum up to 14.7 eV. Accounting for the electron affinity of the C_4H radical of 3.53 eV [133] this many-body dissociation is not energetically accessible at a projectile energy below 11.2 eV. We observe the fragment at an electron impact energy of 6.2 eV. It must therefore be created in a different process which required less energy. Instead of losing all three hydrogen atoms, only one of the hydrogen atoms may be lost individually, while the other two hydrogen atoms attach to the oxygen, forming water. The energy released in the formation of water (9.6 eV [30]) leads to an energetically allowed dissociation path:

$$C_4H_4O + e^- \rightarrow C_4H^- + H + H_2O. \tag{6.2}$$

[10] The estimate is based on the known value of 3.6 eV for breaking the C-O bond in tetrahydrofuran and 3.7 eV in diethyl ether [46].

[11] This value has been taken from [12] and was calculated for the CH_3O radical. Although this molecule is quite different from the fragment considered here, the "active" part of the molecule is very similar.

[12] The value was taken from the C-H bond dissociation energy in the CH_2CH radical [12].

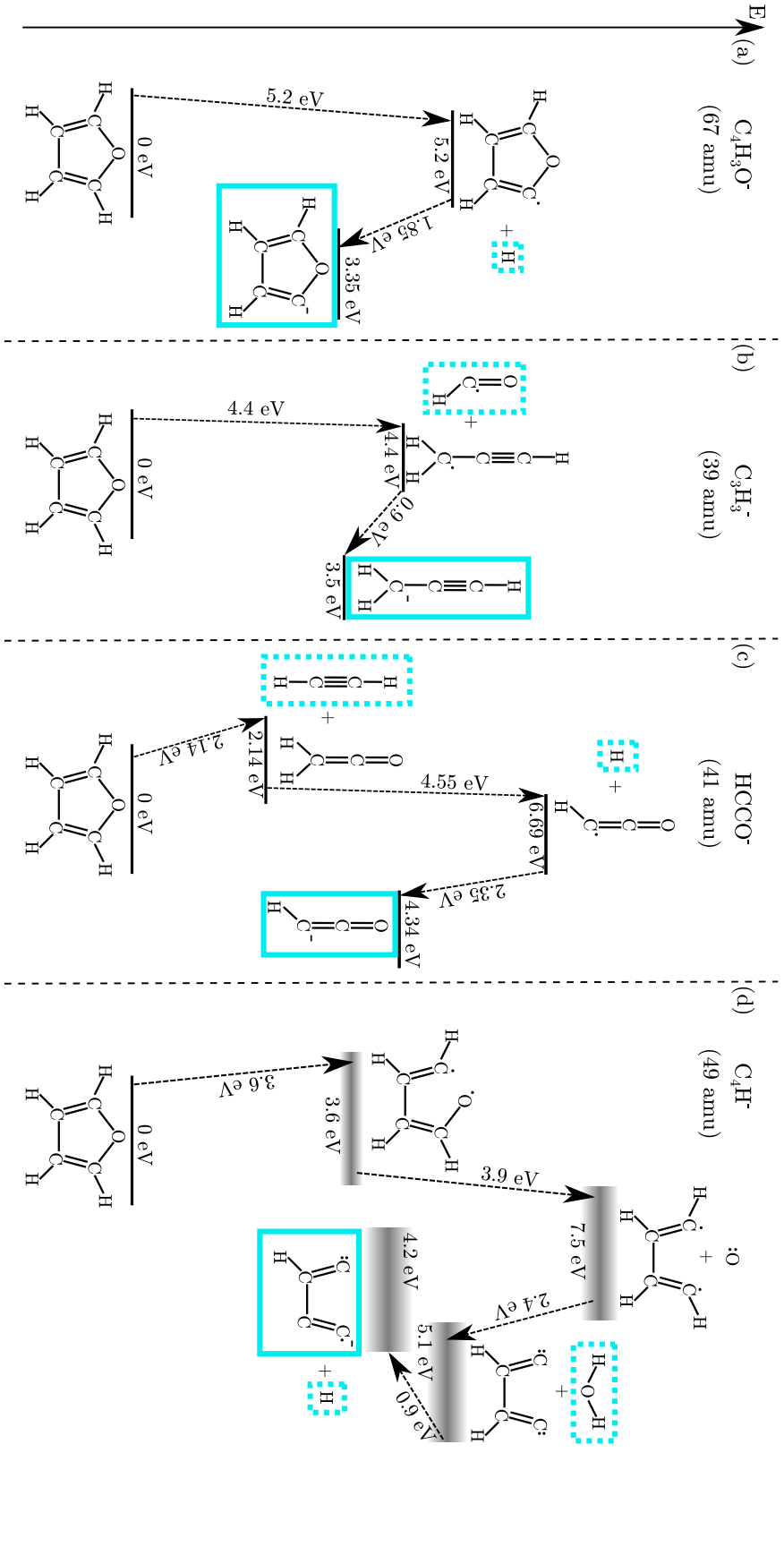

Figure 6.41: Energies of the different fragments which are used to calculate the energy of the produced anionic fragment. The steps do not show the physical dissociation process but rather the path chosen to reach the observed fragment. All values for the C_4H^- fragment are estimates. The observed anions are highlighted in the solid blue boxes and the neutral fragments which are created in the assumed process are highlighted in dotted blue boxes.

Even with the high degree of uncertainty in the bond dissociation energies, the high discrepancy between available energy and required energy without water formation clearly shows that the formation of water is a necessary step in the dissociation. This 3-body dissociation process is also energetically accessible at our electron impact energy.

Kinetic energy distributions

Figure 6.42 shows the kinetic energy distributions of all observed fragments. Since it is not possible to calculate the complete kinetic energy release for dissociation into more than two fragments, only the energy of the observed fragment is depicted. The fragment kinetic energy distributions clearly show two different regimes. For the 39 amu and 67 amu fragments, the kinetic energy distributions have clearly defined maxima at 85 meV and 12 meV, respectively. For the 41 amu and 49 amu fragments on the other hand, the kinetic energy peaks at zero. These two regimes correspond to two different processes: dissociations which are intrinsic 3-body dissociations show a low kinetic energy in the detected fragment and the most likely kinetic energy at 0 eV. For 2-body dissociations on the other hand we obtain a rather well defined maximum in the kinetic energy distributions above 0 eV.

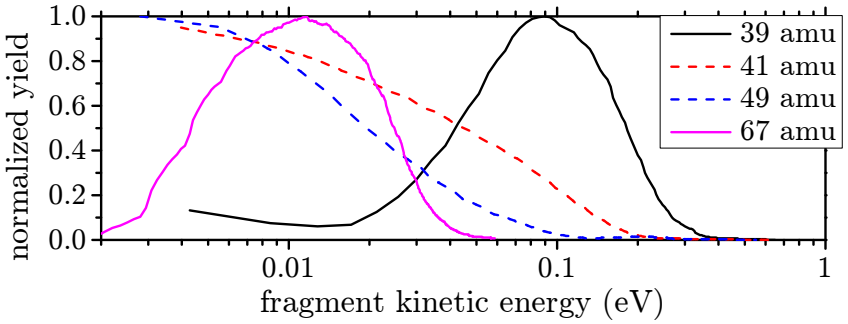

Figure 6.42: Kinetic energy of different fragments created by DEA in furan. Fragments created in 2-body dissociations (39 amu and 67 amu) show a well defined maximum in the kinetic energy distribution while fragments created in 3-body dissociations are most likely created with close to no kinetic energy.

6.5.2 Pyridine

Pyridine (mass: 79 amu) is a six membered ring consisting of five carbon atoms and one nitrogen atom. Due to its close relation to pyrimidine which is part of DNA-bases it is a molecule of high interest for understanding interactions of electrons and biological matter. We have performed measurements of DEA in this molecule both at the Heidelberg DEA apparatus and at the GASIC apparatus at the Open University with the goal to identify fragments which are produced, their ion yield curves and their momentum distributions.

Measurements in the Heidelberg apparatus

First measurements with the Heidelberg apparatus were carried out in the energy range of 2 eV to 12 eV and an additional measurement with longer accumulation time at a fixed energy of 9 eV was performed. These experiments revealed several fragments with masses of 16 amu, 26 amu, 51 amu and 78 amu, which is shown in

figure 6.43(a). An additional peak, which is visible in the figure around 40 amu is attributed to background events because no typical peak in the spatial distribution on the detector was found. Peaks in the time-of-flight distribution were clear enough to identify the fragments but generally too low to measure ion yield curves as a function of energy. Only for the most abundant fragment at 26 amu we were able to find a resonance maximum around an impact energy of 9 eV which is shown in figure 6.43(b).

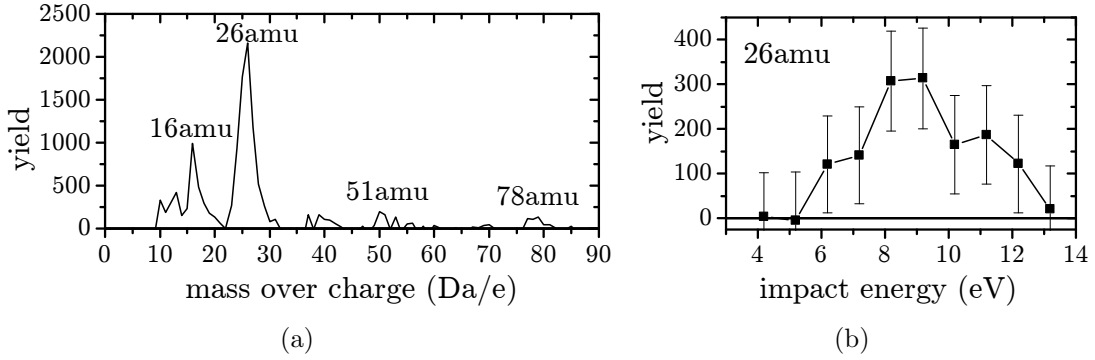

Figure 6.43: (a) Masses of the detected fragments from dissociative electron attachment in pyridine at an impact energy of 9 eV observed in the Heidelberg DEA apparatus. (b) Ion yield curve for the fragment with the mass 26 amu around the observed resonance at 9 eV. Background events have been subtracted for these graphs. Most peaks are barely distinguishable from background noise.

At 16 amu there are two possible fragments which can in principle be produced from pyridine, namely NH_2^- and CH_4^-. We can easily exclude CH_4^- as a possible fragment because methane has an electron affinity of -1.9 eV [132] and therefore the negative ion would be unstable. The NH_2 fragment on the other hand has an electron affinity of 0.78 eV [21]. The observed anion at this mass can therefore be identified as NH_2^-. The observed mass of 26 amu in a pyridine fragment can be either $C_2H_2^-$ or CN^-. However, $C_2H_2^-$ is not expected to form because its neutral form C_2H_2 has an electron affinity of -1.4 eV [132], i.e. no additional electron can be bound to the molecule in a stable state. The electron affinity of CN however is very high (3.86 eV [14]) so we can conclude that the observed fragment at 26 amu is indeed CN^-. For the fragment at 51 amu no straightforward identification is possible because there is no data about electron affinities of the two possible fragments HC_3N and C_4H_3 to decide if the corresponding anions are stable or not. However, $C_4H_3^-$ has been observed in negative ion mass spectrometry as a fragment of several parent molecules [32] showing that this negative ion is stable. HC_3N^- however was only recently observed in experiments [42] and supporting theoretical calculations showed that the stability of the bond of the additional electron depends strongly on its geometry. While it is stable in a bend geometry, in a linear geometry the electron will detach [43]. Therefore, we do not know which of the two possible fragments with a mass of 51 amu has been produced. The fragment with mass 78 amu is $(PY\text{-}H)^-$ ($C_5H_4N^-$) and is produced by hydrogen loss from the pyridine molecule.

Detailed investigations were performed using the GASIC setup. The higher target density in the effusive gas beam in the GASIC experiment enabled us to investigate dissociation channels which are almost undetectable in the Heidelberg setup.

Ion yield curve measurements in the GASIC apparatus

In the GASIC apparatus we obtained ion yield curves for all observed fragments, which are shown in figure 6.44. In addition to confirming the existence of the fragments found with the Heidelberg apparatus, we observed another fragment with a mass of 12 amu (C^-) in these experiments. We observe a strong peak at a low impact energy close to 0 eV in all fragment channels. These peaks are experimental artifacts. The electron gun produces only a very low current at projectile energies below 1.5 eV and the normalization is influenced by background events. At low electron energy, events are weighted stronger due to the low current of the electron gun. Background event which are independent of the electron current are scaled as well when they are not precisely subtracted from the raw data, thereby creating these peaks. Therefore we exclude the very low energy range from our analysis and only show the ion yield curves for impact energies above 1.5 eV.

The measurement of the ion yield curves confirms the resonance at 9 eV for the CN^- (26 amu) fragment observed in Heidelberg. This fragment also shows a typical polar dissociation yield which starts around 20 eV and reaches a plateau around 40 eV (cf. figure 6.44(b)).

Polar dissociation is a process which can produce negatively charged fragments at high electron impact energies. In this process, a molecule is excited by electron impact and subsequently dissociates into one positively charged and one negatively charged fragment. However, the electron is not captured in this process [73].

$$C_5H_5N + e^- \longrightarrow C_5H_5N^* + e^- \longrightarrow C_4H_5{}^+ + CN^- + e^- \tag{6.3}$$

Since the electron is not captured, polar dissociation is not a resonant process and it usually shows no sharp peaks in the energy dependence of the negative ion yield. Instead, polar dissociation cross sections are comparable to those of electron impact excitation, since this is the first step of polar dissociation. The cross section rises with increasing impact energy from the threshold energy until it reaches a maximum. For higher impact energy, the cross section either stays constant or it decreases slowly [73, 114].

The anion yield curves for the fragments at 51 amu (HC_3N^- or $C_4H_3^-$) and 78 amu (PY-H^-) show a resonance at 2.6 eV as well as a very broad peak reaching from 10 eV to 25 eV. Although the yield curves show anion production for all impact energies above 25 eV as well, they do not show a threshold at 20 eV, which is the polar dissociation threshold observed in the CN^- fragment (cf. figure 6.44(c) and (d)). Instead, the broad peak between 10 eV and 25 eV might be caused by polar dissociation at unusually low impact energies. The onset of this peak at 10 eV is just above the ionization threshold of pyridine (9.3 eV). Polar dissociation might already occur in this energy range.

For the 12 amu (C^-) fragment (cf. figure 6.44(a)) the ion yield curve is very similar to the 51 amu and 78 amu fragments for impact energies above 10 eV. At lower impact energy, no C^- fragments are observed. To create this fragment, all three bonds of the carbon atom have to be broken, requiring more energy than the production of all other fragments. It is to be expected that this fragment can only be obtained at high impact energies.

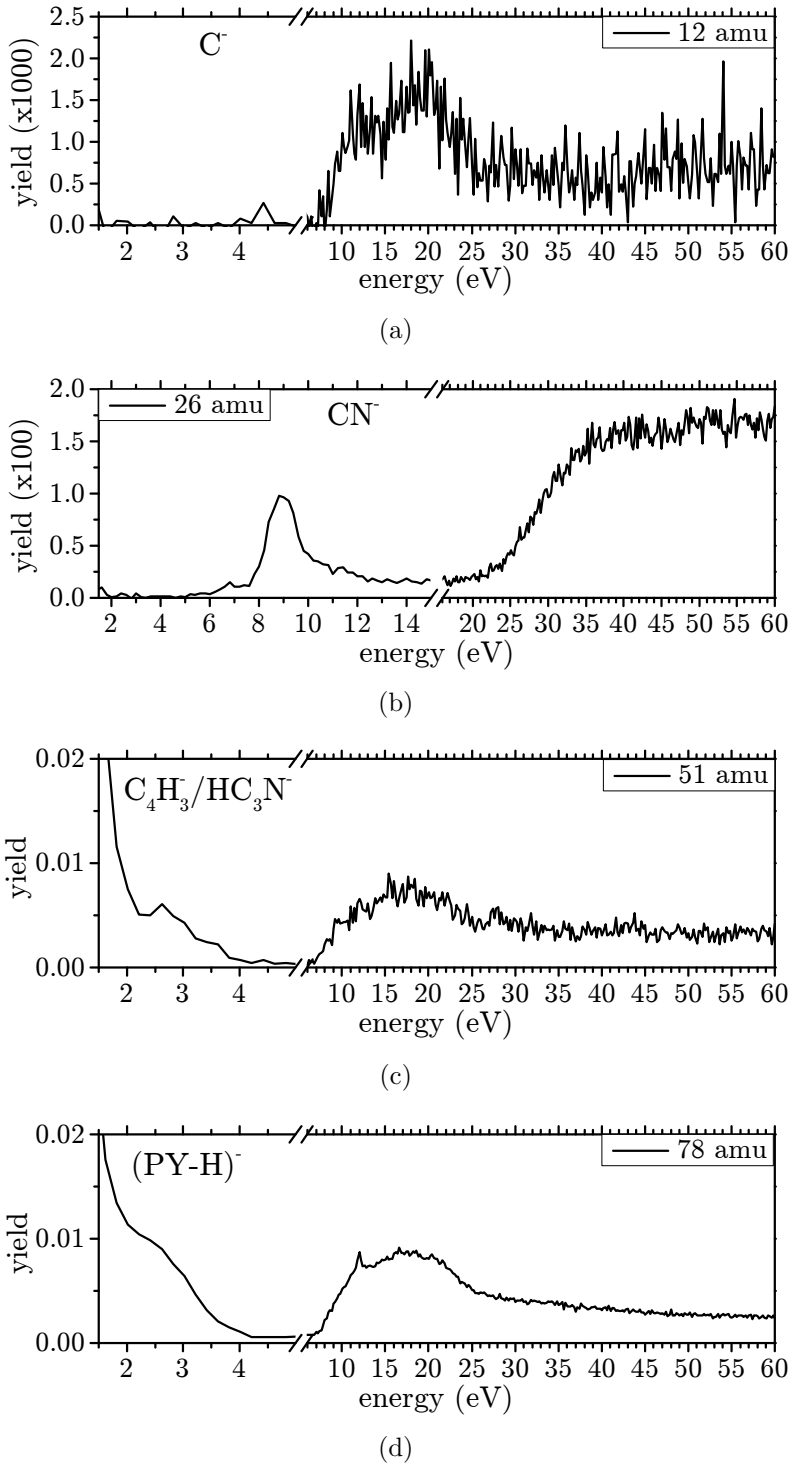

Figure 6.44: Ion yield curves for different fragments of pyridine. All curves are cross-normalized. The measurements were performed using the GASIC setup at the Open University.

The broad peaks in the anion yield of the 12 amu, 51 amu and 78 amu fragments are very similar, which is unusual for DEA and therefore an additional sign that anion production in this range is caused by polar dissociation. Furthermore, the polar dissociation yield in the 26 amu fragment has its onset at 20 eV and therefore exactly at the energy when the anion yield in the other channels starts to decrease. This can be interpreted as two competing polar dissociation channels with different threshold energies.

Momentum measurements of NH_2^- and CN^- in the GASIC apparatus

Our gas beam showed contamination by oxygen from the air, producing O^- with a mass of 16 amu. This prevented us from acquiring a normal ion yield curve for the 16 amu resonance. However, velocity slice images showed a clear distribution with lower kinetic energy than the oxygen contaminant. This momentum distribution is shown in figure 6.45(d). We used a series of momentum images at different energies to separate the contamination from the pyridine fragment and determined the ion yield for the NH_2^- fragment from those momentum images. The resulting ion yield curve is shown in figure 6.45(a). These measurements allowed us to determine the maximum of the DEA peak at 6.3 eV. The angular distribution of this fragment exhibits a broad peak around 90° and is shown in figure 6.45(c). Additionally, the kinetic energy distribution (figure 6.45(b)) has a clear maximum at 100 meV.

The kinetic energy distribution is very unusual for this kind of ring-breaking channel. To obtain this fragment it is not sufficient to break bonds within the molecule but additionally, two of the hydrogen atoms have to become bound to the nitrogen. In most cases a dissociation which involves a change in the molecular structure is slow and transfers most of the excess energy to internal degrees of freedom in the form of rotational and vibrational excitation. These processes usually only show an isotropic angular distribution and very low kinetic energy in the anionic fragment. To exclude a misidentification of the fragment, special care was taken to compare the observed distribution with that of other fragments with a mass of 16 amu. The most likely candidates for misidentification are O^- from oxygen and NH_2^- from ammonia, both of which were investigated before in the same apparatus. It is unlikely that this signal is caused by ammonia contamination since the measured kinetic energy is lower than the energy measured for NH_2^- from ammonia and the peak of the resonance is at a higher energy than the one for the ammonia resonance (cf. section 6.2). The fragment also was not seen in other measurements performed after the experiments on ammonia so we can exclude it as a contamination. O^- from oxygen was seen in the same measurement and has its resonance peak at a similar energy to that measured for this 16 amu fragment but it has a much higher kinetic energy. We also exclude a "shadow" created by O^- ions that followed some unexpected flight path as a source of this signal because it was not visible during calibration measurements with pure oxygen using the same spectrometer settings. We therefore conclude that NH_2^- is indeed produced by DEA in pyridine.

The next goal is to identify the symmetry of the resonance from which the fragment is produced. We can use our experimental results to restrict the possible symmetries for the observed resonance. However, we need to assume a symmetric dissociation. This process is shown in figure 6.46. Both hydrogen molecules attach to the nitrogen molecule simultaneously in a symmetric process and the molecule dissociates along its main axis, as shown by the red arrows.

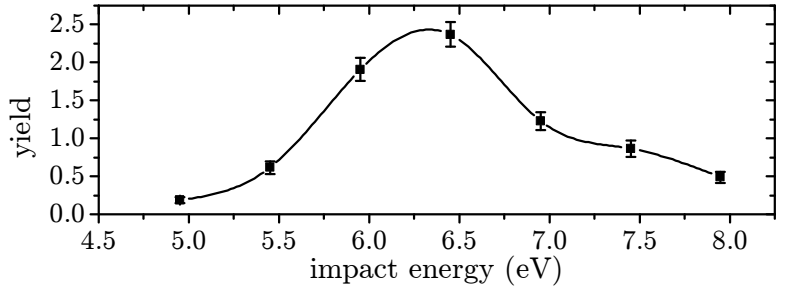

(a)

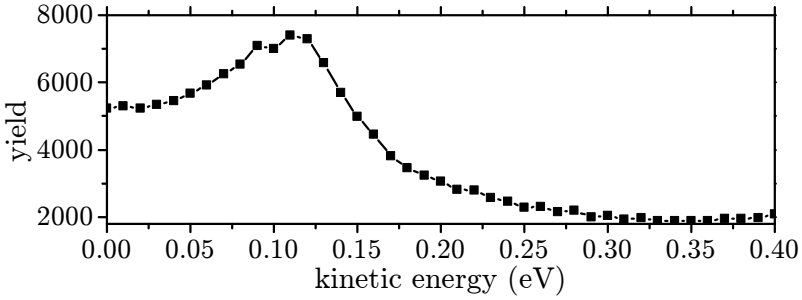

(b)

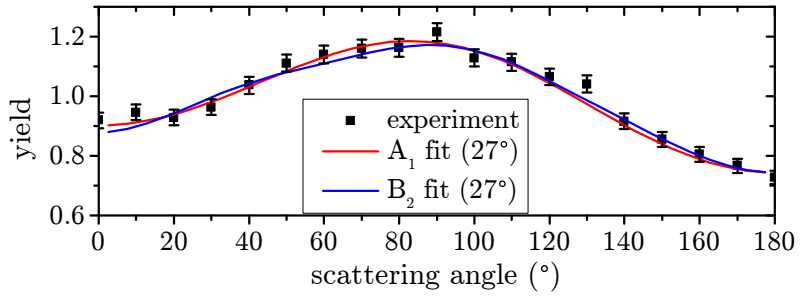

(c)

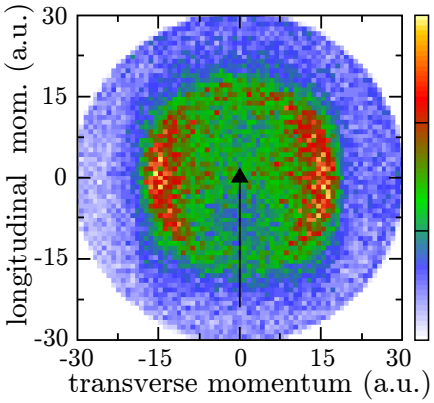

(d)

Figure 6.45: Results for production of the 16 amu fragment (NH_2^-) in pyridine. (a) ion yield curve, the line is a guide to the eye, (b) kinetic energy distribution of the fragment, (c) angular distribution in the experiment and fits assuming A_1 and B_2 symmetries as well as the angular resolution of the setup, (d) momentum image. (b)-(d) are taken at 6.5 eV impact energy.

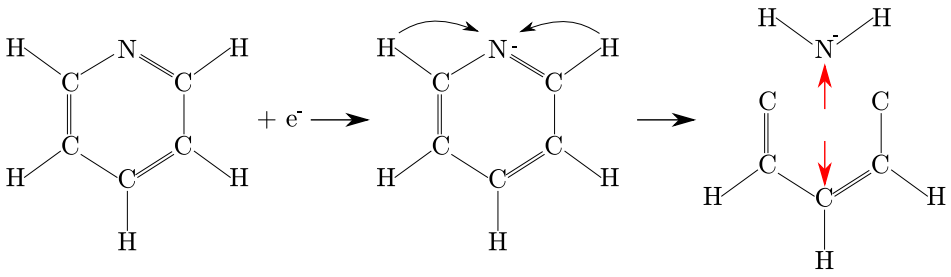

Figure 6.46: Proposed symmetric dissociation process which forms NH_2^- by dissociative electron attachment to pyridine.

The alternative to this process is a sequential dissociation, which starts with a ring-opening next to the nitrogen and ejects the NH_2^- fragment from a new geometry of the molecule. Our main argument for choosing the symmetric process is the observed kinetic energy of the fragment. The kinetic energy distribution shown in figure 6.45(b) is very sharp, when taking into account the relatively low resolution of the instrument. A sequential process is slower and transfers most of the excess energy into internal degrees of freedom. From this kind of dissociation process we would expect neither the observed kinetic energy nor the anisotropic angular distribution, seen in figure 6.45(c).

When we assume that the NH_2^- fragment is ejected along the main axis of the molecule, the only allowed symmetries for the state of the parent anion are A_1 and B_2. Figure 6.45(c) shows partial wave fits using those symmetries, including the same angular resolution function which was also used in the analysis of the water data. Assuming an A_1 symmetry in our partial wave analysis, we can reproduce the observed angular distribution with the broad maximum around 90° very well. When we use the B_2 symmetry for the parent state in the partial wave analysis, the allowed angular distributions are generally more constrained. The ion yield must vanish at a scattering angle of 0° and 180°. In the experiment however, we only expect a drop in the ion yield due to the limited angular resolution and the yield will not reach zero at those angles. A partial wave fit using the B_2 symmetry as the parent state is therefore also able to reproduce the observed angular distribution, which is shown in figure 6.45(c) as well. As a result of the limited angular resolution of the instrument, our experiment can only restrict the symmetry of the resonance to either A_1 or B_2. An additional comparison with theoretical predictions can help to find the symmetry of the parent anion.

In recent molecular R-matrix calculations, the electron scattering from pyridine was investigated by the Gorfinkiel group at the Open University [111, 112]. In their calculations they are able to observe resonances in the electron-molecule scattering, which can be precursors to DEA. These resonances are usually identified by the time delay which describes the calculated transit time of the electron through the molecule as compared to a non-resonant transit, only accounting for Coulomb interactions. A high time delay therefore implies that the electron spends more time close to the target and interacts more strongly with the molecule.

The time delay curves for electron-pyridine scattering in an impact energy range between 0 eV and 10 eV is shown in figure 6.47 for the different irreducible representations of the C_{2v} symmetry of the molecule. These representation correspond

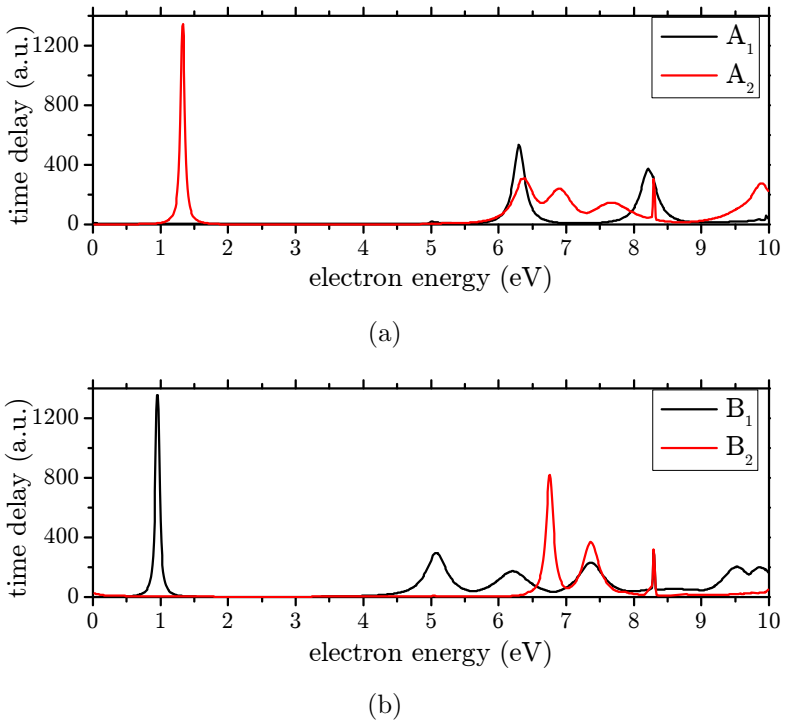

Figure 6.47: Time delay in electron-pyridine scattering obtained in R-matrix calculations for different symmetries of the resonant state in the C_{2v} molecular symmetry. (a) Time delay for the A_1 and A_2 symmetry. (b) Time delay for the B_1 and B_2 symmetry. The calculations were performed by A. Sieradzka [111].

to different symmetries of the electronic state of the combined electron-molecule system and to the state of the anion if the electron is captured. The resonances are seen as Lorentzian peaks. At an electron energy below 1.5 eV, the time delay shows peaks due to shape resonances and above 4 eV, core-excited resonances appear. The electron energy at which these core-excited resonance peaks are observed in the calculation is usually overestimated [111]. The amount by which the energy of the resonances is overestimated in the calculation can be seen by a comparison with an experiment. In the B_1 symmetry (figure 6.47(b)), the calculations find an electron scattering resonance at 5.09 eV. In electron transmission experiments, this resonance was found at 4.5 eV [77, 82]. Thus, the offset between experiment and theory is 0.6 eV at this electron impact energy and will be slightly larger at higher impact energies.

In our experiment we observed the DEA peak for the NH_2^- fragment at an electron energy of 6.3 eV and we expect to find the corresponding peak in the theoretical calculation in the electron energy range of 6.9 eV to 7.9 eV. As can be seen from figure 6.47, there are no resonances for the A_1 symmetry in this range. For the B_2 symmetry however, there is one resonance in the assumed range (at 7.37 eV) and another resonance at the edge of the range (at 6.76 eV). We therefore conclude that at an electron impact energy of 6.3 eV the parent anion prior to dissociation is in a B_2 state.

The momentum image for the CN^- fragment (26 amu) at 9 eV impact energy has been obtained using the velocity slice imaging mode of the GASIC apparatus and is shown in figure 6.48. It shows an isotropic angular distribution with the maximum

of the momentum distribution at zero. This kind of distribution is typical for a 3-body dissociation process and we will investigate the reaction path in the following part.

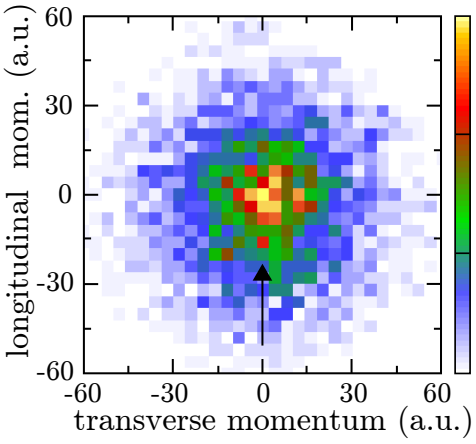

Figure 6.48: Isotropic momentum distribution obtained for the production of the 26 amu fragment (CN^-) in dissociative electron attachment to pyridine at an electron impact energy of 9 eV using the GASIC apparatus.

Reconstruction of the reaction paths

For the 26 amu fragment we can determine if the dissociation takes place in a 2-body or a 3-body dissociation, using reaction enthalpies found for neutral dissociation reaction in pyrolysis of pyridine by Mackie *et al.* [70]. We calculate the energy required for a possible dissociation path leading to two fragments. Like in the analysis of the reaction paths in furan these steps do not necessarily represent the actual dissociation path in the reaction and are only used as a path from the initial state to one possible final state and to calculate the energy difference between both states.

The first step in the dissociation is the breaking of a C-H bond. In this case, the hydrogen next to the nitrogen atom is ejected, requiring an energy of 4.6 eV [7].

$$C_5H_5N \xrightarrow{4.6\,eV} C_5H_4N + H \tag{6.4}$$

Next, a ring-opening on the other side of the nitrogen occurs, taking another 0.95 eV [70].

$$C_5H_4N \xrightarrow{0.95\,eV} {}^{\bullet}CH{=}CH{-}CH{=}CH{-}C{\equiv}N \tag{6.5}$$

In the next step, we break the C-C bond to obtain the CN radical. There is no data available for the reaction in this molecule. However, Mackie *et al.* measured the reaction enthalpy for this dissociation in a very similar radical, namely ${}^{\bullet}CHCHCN$ [70]. There, the dissociation enthalpy is 2.65 eV. When we compare this value to the dissociation enthalpy of 5.77 eV for the closed shell CH_2CHCN molecule [12], the strong destabilizing influence of the radical group is obvious. In the molecule which we consider here, the radical group is located further away from the C-C bond which is supposed to be broken and its destabilizing influence on the bond might

be less strong. Nevertheless, we can roughly estimate that the dissociation enthalpy should be between 3 eV and 4 eV.

$$^{\bullet}\mathrm{CH{=}CH{-}CH{=}CH{-}C{\equiv}N} \xrightarrow{3\text{-}4\,\mathrm{eV}} {}^{\bullet}\mathrm{CH{=}CH{-}CH{=}CH} + {}^{\bullet}\mathrm{C{\equiv}N} \tag{6.6}$$

In the last step we consider the attachment of the electron to the CN radical which has an electron affinity of 3.86 eV.

$$^{\bullet}\mathrm{C{\equiv}N} + \mathrm{e}^{-} \xrightarrow{-3.86\,\mathrm{eV}} \mathrm{CN}^{-} \tag{6.7}$$

To reach a state with only two fragments, we will assume that the free hydrogen atom which was created in the first step becomes bound to the produced radical for an estimated typical binding energy of 4.3 eV. For the observed DEA peak of the CN^- fragment at a projectile energy of 9 eV this means that the excess energy of the reaction is expected to be between 7.6 eV and 8.6 eV. Therefore, a kinetic energy between 5.1 eV and 5.7 eV would be expected for the CN^- fragment. From the momentum image in figure 6.48 it can be seen that most ions arrive with a momentum below 15 a.u. which corresponds to a kinetic energy of only 64 meV. This large discrepancy is not created by energy which is stored in vibrational excitation but rather results from the fact that the fragment is produced in a many-body dissociation. Therefore, more energy is needed when the hydrogen is not attached to the neutral radical. Additionally, more excess energy is carried by the other fragments in the form of kinetic energy, e.g. by the atomic hydrogen. This is in agreement with our observation of kinetic energy distributions in furan. They showed that dissociation into more than two fragments leads to anions with the kinetic energy distribution peaking at zero, which is also the case for this fragment. We conclude that the CN^- fragment is produced in a 3-body dissociation.

The production of the $(PY\text{-}H)^-$ anion by loss of one hydrogen atom shows a small peak at low a impact energy of 2.6 eV. This can be seen in the ion yield curve in figure 6.44(d). The bond dissociation energy of the C-H bonds is in the range of 4.5 eV to 4.8 eV, depending on the position of the bond within the molecule [7] and the C_5H_4N radical has an electron affinity of 2.4 eV [36, 37]. This sets the lower limit of electron impact energy from which the fragment is energetically accessible at 2.1 eV. Therefore, the $(PY\text{-}H)^-$ production at 2.6 eV takes place just above the energetic threshold and the ion is produced in the electronic ground state. There also is very low excess energy available, suggesting that the ion is produced in a very low vibrationally excited state or even in the vibrational ground state for the low energy end of the peak.

6.6 Negative ion formation processes in $C_2Cl_2F_2$ and $C_2Cl_2F_4$

We investigated the production of anionic fragments from the molecules 1,2-Dichloro-1,2-difluoroethylene ($C_2Cl_2F_2$, from here on referred to as F2) and 1,2-Dichlorotetrafluoroethane ($C_2Cl_2F_4$, from here on referred to as F4). The structure of the investigated molecules is shown in figure 6.49. The F2 molecule exists as a *cis*- and

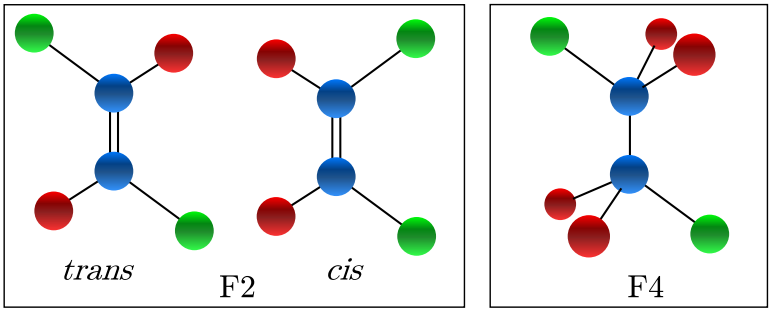

Figure 6.49: Molecular structures of $C_2Cl_2F_2$ (F2) and $C_2Cl_2F_4$ (F4). Blue balls: carbon atoms, red balls: fluorine atoms, green balls: chlorine atoms.

a *trans*-isomer, as is shown in the figure. We performed the experiments with a mixture of both isomers.

Both molecules were used as refrigerants in the past but they have been found to damage the ozone layer and have therefore been banned for industrial and domestic use in the Montreal protocol [97]. Their dissociation reactions and especially differences in the dissociation yield between those rather similar molecules can give insight into their damaging potential.

In previous studies, dissociative electron attachment in the F4 molecule was investigated in an impact energy range from 0 eV to 15 eV by two groups [66, 116] with contradicting results and in the F2 molecule only one study investigated DEA at impact energies below 10 eV [58]. Our goal is to confirm one of the contradicting observations and to expand the measurement of ion yield curves for both molecules into the range of polar dissociation. The measurement of both molecules in the same apparatus also enables us to compare dissociation yields between both molecules quantitatively. The experiments were performed in the GASIC apparatus at the Open University.

Identification of the fragments

We performed time-of-flight measurements for fragments from both molecules at an electron impact energy of 3 eV, which are shown in figure 6.50. The time-of-flight spectra of anionic fragments produced via DEA showed five peaks for the F2 molecule and a sixth peak for the F4 molecule. We identified the fragments which were present in both molecules as: F^- (19 amu), Cl^- (35 amu and 37 amu), ClF^- (54 amu), Cl_2^- (70 amu) and $CClF_2^-$ (85 amu). In the F4 compound another unidentified peak (X_1^-) was observed at a time-of-flight shorter than should be possible for any fragment of this molecule but with an ion yield curve very similar to the curves of other fragments which suggests that it was produced in dissociation of the investigated molecule.

In the previous study by Szymańska-Skolimowska, different fragments were identified. Instead of the fragment ClF^- (54 amu) she observed CF_2^- (50 amu) and instead of Cl_2^- (70 amu) she observed $CClF^-$ (66 amu). Although we performed the experiment in the same apparatus as Szymańska-Skolimowska, our identification of the fragments is consistent with the study by Langer *et al.* We conclude that the identification of the fragments by Langer *et al.* is indeed correct.

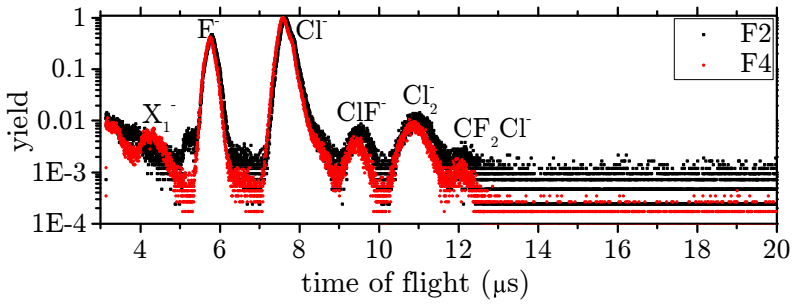

Figure 6.50: Time-of-flight spectrum for $C_2Cl_2F_2$ (F2) and $C_2Cl_2F_4$ (F4) for an electron impact energy of 3 eV. Both spectra are normalized to the Cl^- yield.

In the next step we performed ion yield curve measurements for all observed fragments in both molecules which are shown in figure 6.51. All curves in this figure were cross-normalized by monitoring the total charge delivered from the electron gun and the pressure in the experimental chamber for every measurement. As mentioned in the pyridine section, the electron gun delivers a very low current for electron energies below 1.5 eV which prohibits confident normalization. Therefore we restrict the ion yield curves to impact energies above 2 eV.

Ion yield from dissociative electron attachment

In the low impact energy region, our ion yield curves are in good agreement with the previous measurements by Langer *et al.* [66] for the F4 molecule and with the measurements by Illenberger *et al.* [58] for the F2 molecule. We observe dissociative electron attachment mainly in two impact energy regions: at 3 eV and between 6 eV and 11 eV. We can distinguish both resonance regions using thermochemical calculations. We estimate the bond dissociation energy of the C-F bond, leading to the formation of the F^- fragment from available data of similar molecules. In chlorofluoromethanes, the bond dissociation energy rises steadily with the fluorine content from 4.4 eV for $CCl_3F \longrightarrow CCl_3 + F$ to 5.7 eV for $CF_4 \longrightarrow CF_3 + F$ [74]. Thus, we estimate the bond dissociation energy to be around 5 eV in the molecules we investigated. The electron affinity of fluorine is well established at 3.4 eV [58]. Therefore, the thermochemical threshold for the production of the F^- fragment by simple C-F bond cleavage is around 1.6 eV.

For the Cl^- fragment we can calculate the thermodynamical threshold the same way. The C-Cl bond dissociation energy in the F4 molecule is 3.4 eV [74] and the electron affinity of chlorine is 3.6 eV [58]. Therefore the simple bond cleavage reaction

$$C_2Cl_2F_4 + e^- \longrightarrow C_2ClF_4 + Cl^- \tag{6.8}$$

is already accessible at an impact energy of 0 eV. McMillen *et al.* give C-Cl bond dissociation energies in different molecules which are varying only slightly. We therefore assume that in the F2 molecule the Cl^- channel is accessible at the same impact energy. The DEA peaks at 3 eV impact energy are still close to the thermochemical threshold of 0 eV and therefore they are caused by electron capture into a shape resonance while the peaks in the higher energy range are produced by electron capture into core-excited resonances.

When comparing the cross-normalized ion yield curves as a function of projectile impact energy for the same fragments from the two different molecules, a general

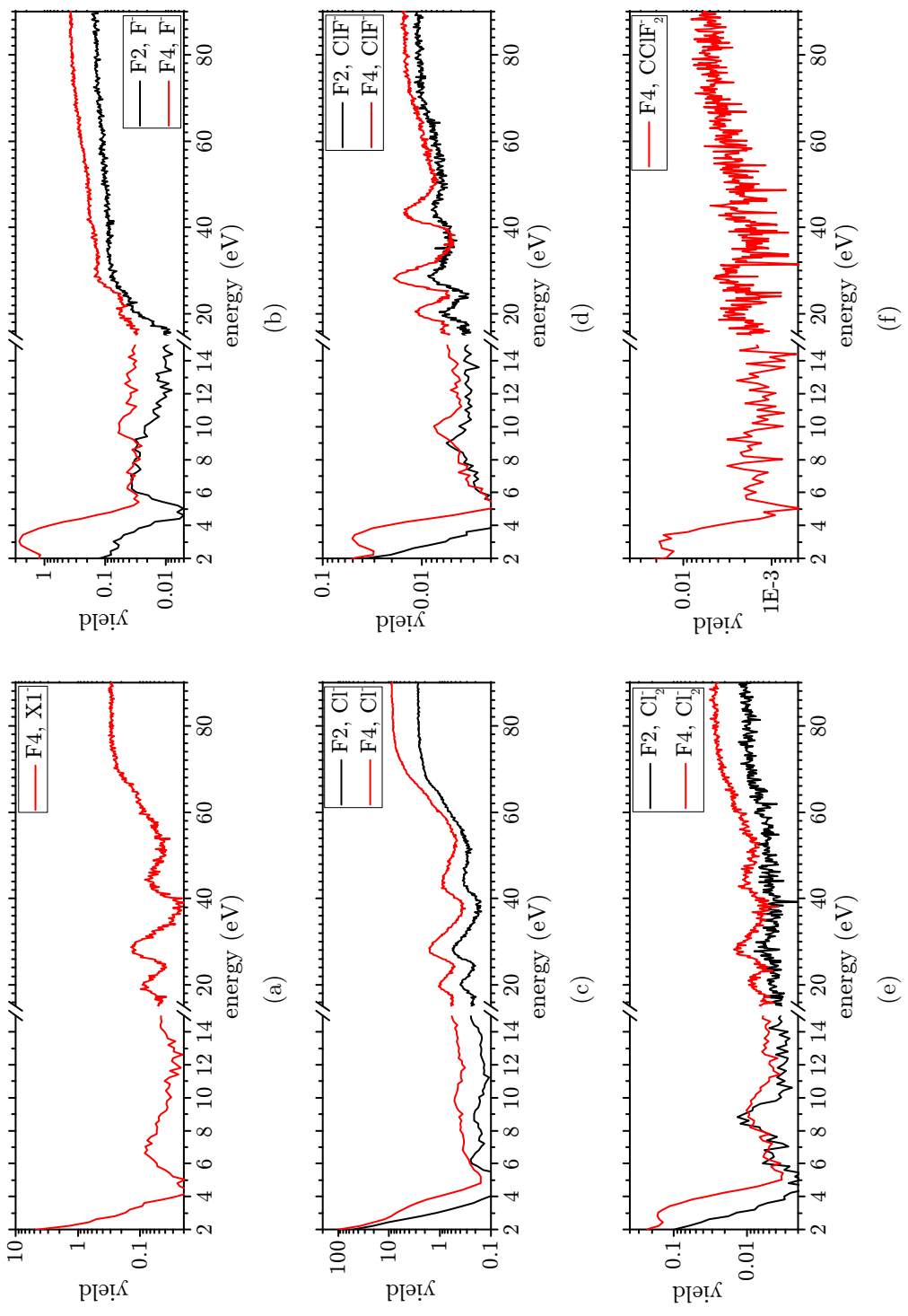

Figure 6.51: Comparison of ion yield curves for different fragments from F2 and F4. The region from 0 eV to 15 eV is shown in detail. All curves are cross-normalized. The ion yield curves for X_1^- existed only in F4 and the yield of $CClF_2^-$ was too low for analysis in the F2 molecule. The increasing yield towards very low impact energy between 2 eV and 4 eV is an experimental artifact.

trend towards higher negative ion yields in the F4 molecule can be seen (cf. figure 6.51). The differences are especially strong in the region of the shape resonance (3 eV impact energy). In the F4 molecule, all fragments are produced in this energy range, albeit with strongly varying yields. In the F2 molecule on the other hand, only the F^- fragment is produced and the yield is only 2% of the F^- yield in the F4 molecule. At this low impact energy the F2 molecule is more stable against dissociation than the F4 molecule. This observation shows that the resonance which creates the 3 eV peak is very sensitive either to the C-C single bond, or it is connected to electron capture into an orbital which is localized at the fluorine atoms and is very sensitive to the fluorine content of the molecule.

In the second range of DEA resonances between 6 eV and 11 eV electron impact energy several peaks are observed, the position of which depends on the parent molecule as well as the produced anion. This situation is typical for DEA, where the energy of resonances and dissociation pathways depend on the structure of the molecule. A further peak at an electron impact energy of 6.5 eV is observed in several fragments of the F2 molecule but not in the F4 molecule. This difference between the two molecules is a sign that the parent anion in the F2 molecule is unstable towards DEA while the corresponding anion after electron capture in the F4 molecule leads to auto-detachment of the electron. Furthermore, both molecules show a DEA peak at higher energy, at 8.9 eV for the F2 molecule and at 9.9 eV for the F4 molecule. It is likely that these DEA peaks are caused by electron capture into similar orbitals for both molecules. In the F4 molecule however the energy required for DEA is slightly higher which shows that the energy of the orbital in which the electron is captured is higher in this molecule.

Anion yield above the ionization threshold

At electron impact energies above 15 eV, dissociative electron attachment only plays a minor role in the production of negatively charged fragments and other processes like polar dissociation become important. This process has been described in the previous discussions of the pyridine measurements on page 103. The typical energy dependence of the anion yield from polar dissociation can be best seen in the Cl^- fragment: in both the F2 molecule and the F4 molecule, the anion yield rises from an impact energy of 50 eV until 70 eV and then stays almost constant over the rest of the investigated energy range. Interestingly, the F^- fragment shows the polar dissociation threshold already at an energy of 16 eV, while a minor increase in the previously mentioned range above 50 eV is visible as well. These findings show that the fluorine bonds are most vulnerable to polar dissociation, which is already accessible at relatively low projectile energies. A higher impact energy is necessary to break the other bonds in the molecules. In the energy range above 15 eV, the ion yield curves of both molecules are very similar. This measurement suggests that polar dissociation is less sensitive to the structure of the molecule.

The ion yields of all fragments also exhibit an unusual energy dependence in the intermediate energy range for both molecules, showing three broad peaks around impact energies of 20 eV, 28 eV and 43 eV. These peaks are outside the typical energy range of DEA, which is seen at energies below 15 eV. The fast change of the anion formation cross section and the peaks in the electron impact energy which are only a few eV wide are typical signs of resonant processes. The structures are

however observed at an energy above the ionization limit which is located at 12.5 eV for the F4 molecule [23]. The electronic states involved in the observed resonances must therefore be doubly-excited or core-excited states. The assumption that an inner shell electron is excited in the process can explain why the structures are observed at the same energies for both molecules. The highest occupied molecular orbitals are spread out over the molecule and form the bonds between the atoms. The energy of those orbitals depends strongly on the molecule and the bonds within the molecule. The more tightly bound inner shell electrons on the other hand are located at one of the atoms and are almost uninfluenced by the molecular structure and the atomic bonds. Experimental negative ion yield curves, which we could compare to our observations, are scarce in this energy range. Resonant structures in the negative ion yield above the ionization threshold have however been observed in chlorine by Kurepa *et al.* [64]. Besides regular DEA peaks at low energy, they observed a broad peak for Cl^- production between 11 eV and 30 eV. They attributed the peak to dissociative electron attachment following electron capture into the core-excited Cl_2^- parent anion. This process had a much higher cross section than polar dissociation where it was observed. The situation in the molecules which we studied is similar and different core-excited states of the parent anion are populated in the energy range between 20 eV and 50 eV.

In the polyatomic molecules which we investigated, the possible reactions after electron capture are more complex. In the intermediate energy range in which the resonances are observed, the internal energy of the molecule after electron attachment is high enough to start several processes. Dissociation of a negatively charged fragment is one of them as it can be observed in the experiment. The energy of the core-excited parent ion is however sufficient for further dissociation, ionization, or relaxation by emission of a photon, which remains hidden to the experiment.

In an earlier study, Jabbour *et al.* investigated electron impact dissociation of a similar molecule, namely CCl_2F_2 [59] by observing light emission from neutral many body dissociation. In their experiments, one of the fragments - either chlorine or fluorine - had to be created in an electronically excited state. Jabbour *et al.* then used the light from emission lines of chlorine and fluorine to measure the dissociation yield. These dissociation processes have threshold energies in the range from 20 eV to 30 eV and many of the corresponding light emission curves show peaks in the yield at just above the threshold energy. When those results are compared to our own negative-ion-formation measurements at similar energies, it is reasonable to assume that a similar dissociation process can be responsible for our observations. In contrast to the photoemission measurements of Jabbour *et al.*, the process observed in our experiments must additionally capture the projectile into one of the fragments. Due to the high content of chlorine and fluorine in our target, many fragments which are created have high electron affinities. Just above the threshold energy for dissociation, the projectile electron loses almost all its kinetic energy and it is very likely that the electron is captured by one of the fragments with high electron affinity. This process can create the broad resonance maxima which we observe at intermediate impact energies.

Momentum imaging

In addition to the ion yield curves, velocity slice images of the F^- and Cl^- fragments have been taken for the F2 molecule at several electron impact energies ranging

from 3 eV to 90 eV. Some examples of the obtained momentum images are shown in figure 6.52. They show no structure and a kinetic energy which peaks at 0 eV at all measured impact energies. Similar momentum distributions were found in an earlier study for the F4 molecule [116].

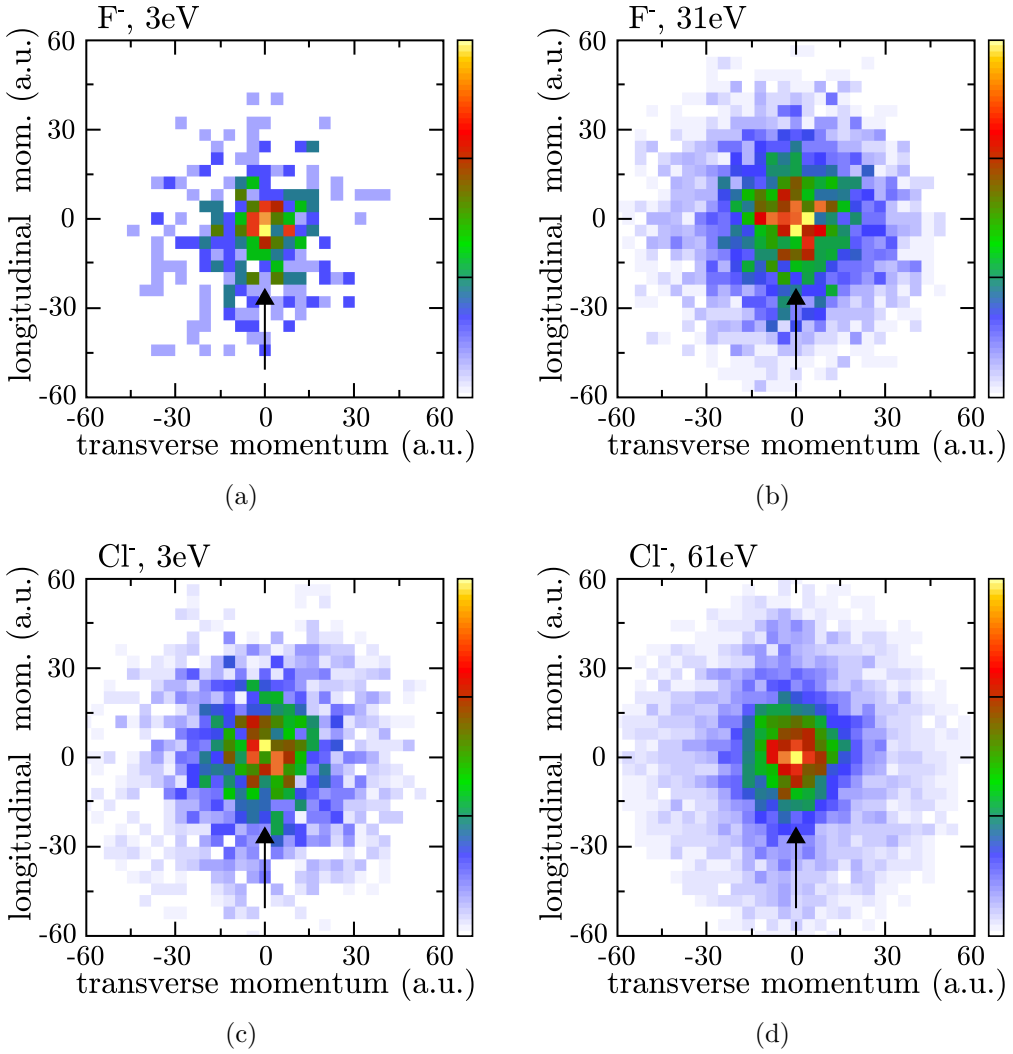

Figure 6.52: Momentum images of F^- production at 3 eV (a) and 31 eV (b) and of Cl^- production at 3 eV (c) and 61 eV (d).

The lack of structure and the low kinetic energy of the observed fragments can have several reasons. At low projectile impact energy, e.g. at the first observed DEA resonance around 3 eV, we concluded from thermochemical calculations that only a single bond cleavage produces the F^- and Cl^- fragments. In the 2-body dissociation, the excess energy is 1.4 eV for production of F^- and 3.2 eV for the production of Cl^-. The kinetic energy release of a 2-body dissociation can be calculated from the momentum images in figure 6.52(a) and (c) using the axial recoil condition. We obtain a kinetic energy release below 15 meV for production of F^- and below 50 meV for production of Cl^-. The high discrepancy between excess energy and kinetic energy release shows that vibrational excitation in the neutral fragment stores most of the excess energy in the reaction. At higher impact energies however, the kinetic energy of the fragments is almost unchanged. This can only be explained by many-body dissociation processes, which are accessible at those energies through

the population of highly excited states in the electron capture.

Conclusions

Overall, the comparison of negative ion formation in 1,2-Dichloro-1,2-difluoroethylene and 1,2-Dichlorotetrafluoroethane shows that the DEA process is very sensitive to changes in the molecular structure and the observed ion yield curves in the DEA region are very different between the two molecules. A very low kinetic energy was measured for the F^- and Cl^- fragment from which we infer the existence of strong vibrational excitation in the range of the shape resonance and many-body dissociation in the range of core-excited resonances.

Processes at higher energy however are insensitive to the differences between the two molecules. Non-resonant polar dissociation as well as the resonant structures at intermediate energy are caused by the production of a core-excited parent anion during the electron capture. Both processes are insensitive to details of the molecular structure, which only has a high influence on electrons in the valence orbitals. Therefore, core-excited dissociation processes and polar dissociation are very similar in both molecules.

7. Summary and outlook

One goal of this work was the improvement of experimental methods for studying low energy electron collisions with atoms and molecules. In the first part of this work a new method for measuring electron impact excitation of metastable states in atoms was developed. The ability of the new design to detect the momentum of atoms in excited states provides a selectivity for metastable states with long lifetimes and the time and position sensitive detection allows a reconstruction of all possible collision kinematics. Resolving the small momentum transfer to the atom proves to be the main challenge in this kind of setup but it was overcome by a combination of a very cold and narrow supersonic gas jet with a photoemission electron gun. While the supersonic gas jet provides the target with low initial momentum uncertainty, the photoemission electron gun improves the energy resolution compared to a conventional thermionic gun. The combination of both components increases the resolution far enough to enable the measurement of the momentum transfer to the atom. A state-selective study of electron impact excitation was performed in helium and neon. The angular distributions of inelastic electron scattering show excellent agreement with theoretical calculations using R-matrix calculations and convergent close-coupling calculations in the case of helium. For neon, the measured angular distributions were compared with R-matrix calculations and yielded reasonable agreement. In the setup used in this work, the momentum resolution for the detected atoms was high enough to distinguish several states but not all of them. Some states were too close in energy to be distinguishable in our apparatus. Therefore, a simulation of the experiment was written using theoretical cross sections to compare experimental momentum distributions to theoretical predictions. This step could be eliminated in future experiments if the resolution can be further improved by e.g. producing an even narrower atomic jet or by cryogenic cooling of the electron gun. While it was beyond the scope of this work, increasing the final momentum resolution by about an order of magnitude is in principle possible. This would enable the state-selective investigation for most atoms using this experimental technique, even for energetically close states.

In the second part of this work, a dissociative electron attachment experiment based on the pulsed spectrometer momentum imaging setup of Moradmand *et al.* [79] was built with the goal of investigating complex molecules with biological relevance and

molecular clusters. To increase the momentum resolution compared to other momentum imaging experiments of this kind, a supersonic gas jet and a photoemission electron gun were used in this setup as well. Additionally, the ion detection system was built with a 3-region spectrometer which allowed different acceleration schemes of the produced ions. The spectrometer is capable of switching between a 3D-momentum measurement mode with low mass resolution and a 2D-momentum measurement mode with high mass resolution. In complex molecules with several dissociation channels, this ability is necessary to perform momentum imaging on fragments with similar masses. Experiments were performed in this newly built Heidelberg DEA apparatus at the Max Planck Institute for Nuclear Physics as well as at the GASIC setup at the Open University in Milton Keynes, UK.

The production of NH_2^- by dissociative electron attachment in ammonia at electron impact energies between 4.3 eV and 7.3 eV was studied with the new Heidelberg DEA apparatus. Angular distributions and kinetic energy distributions of the fragment were compared with experimental results from different groups as well as with theoretical *ab initio* calculations. Our results showed an improved momentum resolution compared to results from other groups which were obtained in experiments using a warm effusive gas beam to deliver the target. We could show that the new setup is well suited to investigate heavy and slow fragments. The angular distribution of the NH_2^- fragment was also analyzed using a partial wave expansion by Taylor and O'Malley which we adapted to take into account changes in the geometry of the molecule prior to dissociation. Using this analysis, we could partially reconstruct the electron attachment probability in ammonia in the investigated energy range. We compared these results to *ab initio* theoretical calculations which have recently been performed by Rescigno *et al.* [101] for one energy within the resonance. We found good agreement between the calculations and our observed angular distributions if a change of the N-H bond angle of 25° after the attachment process is included in the calculations. At the high energy end of the investigated resonance we observed changes in the reconstructed electron attachment probability but there are no theoretical predictions at this energy yet.

The improved momentum resolution in our apparatus allowed the first quantitatively correct momentum imaging of O^- production by DEA in water. Theoretical studies of this process predicted molecular dynamics which leads to a change of the H-O-H bond angle before the molecule dissociates into three fragments: two hydrogen atoms and an oxygen anion. For electron attachment via the $^2B_2$ resonance at 11.5 eV, the momentum of the observed O^- fragment corresponds to a lowering of the H-O-H bond angle from the equilibrium angle of 104.5° down to 68°. The decrease of the bond angle is in agreement with the theoretical calculations although only the direction and no magnitude for the change in the bond angle was predicted.

Dissociative electron attachment in molecular clusters was studied in ammonia, water and formic acid. Our ion yield curves for fragments produced from DEA in clusters show that the projectile impact energy which leads to DEA can change in a cluster, compared to the corresponding monomer. In ammonia we could connect these changes to the vibrational degrees of freedom in the cluster. The parent anion is metastable and only dissociates when the vibrational excitation is high enough. In a cluster of ammonia molecules the vibrational energy can be transferred to the neighboring molecules and a higher impact energy is required to allow dissociation.

In formic acid dimers and trimers, DEA caused by shape resonances competes with breaking of the hydrogen bonds between the molecules. At low impact energy within the energy range of the shape resonances only one process occurs while at higher energy within the same electron capture resonance both dissociation of a bond within a molecule and evaporation of an intact molecule from the dimer or trimer can take place.

In the heterocyclic organic compounds furan and pyridine several different dissociation channels were found of which most originate from dissociation into three or more fragments. Using thermochemical data it could be shown that several of the observed dissociation products can only be formed when hydrogen atoms change their position and become bound to a different atom. This is the case e.g. for the production of C_4H^- from furan and for the production of NH_2^- from pyridine. The generally isotropic angular distributions of many fragments suggests that the substantial molecular rearrangement in the investigated molecules can take place on longer time scales than the period of molecular rotation. An anisotropic angular distribution could only be found for hydrogen loss in furan and NH_2^- formation in pyridine. Especially the NH_2^- production from pyridine shows that - even for ring-breaking dissociation channels with rearrangement of hydrogen atoms - fast dissociation is possible.

The sensitivity of processes which produce negative ions to the structure of a molecule was investigated by studying the negative ion yield curves of the two very similar molecules 1,2-Dichloro-1,2-difluoroethylene and in 1,2-Dichlorotetrafluoroethane. Dissociative electron attachment was found to be very sensitive to the molecular structure while the non-resonant polar dissociation shows no difference between the two molecules. In these molecules additional resonant processes were found in the intermediate energy region between 20 eV and 50 eV. The most likely process which is taking place at these energies is a many-body dissociation caused by electron capture in a core-excited state. Only few studies of electron impact dissociation processes at energies above the ionization threshold exist and even fewer studies observed resonant structures in this energy region. Thus it is not yet possible to describe these processes properly. Future studies on negative ion formation and dissociative electron attachment should include the whole energy range up to 100 eV to be able to identify the origin of those processes. So far, the proposed electron attachment into a core-excited state as the first step which leads to the resonance structures is only a hypothesis which can explain our observations.

Overall, in the topic of dissociative electron attachment this work presented the first ion yield curves for pyridine, the first momentum imaging for pyridine and furan, and the first study of the influence of molecular clusters on the dissociation process. In ammonia and water we could demonstrate the advantages of the supersonic gas jet in our setup for studying heavy and slow fragments compared to the commonly used effusive gas beam.

Fragmentation of large molecules by electron impact is an interesting topic for the study of radiation damage in biological tissue but it presents many challenges which already start with the identification of the fragments. In polyatomic molecules, different fragments with the same mass can be created. Several ions which were observed in DEA of furan and pyridine could only be identified when exactly one of the possible ions with the same mass was stable. In the future, performing these

experiments with deuterated molecules would be a useful tool in the identification of fragments and at the same time allow a study of possible isotope effects. Another limiting condition in the choice of target molecules is the gas delivery system. The supersonic jet performs excellent in delivering gases as monomers and as clusters but many molecules which are of biological interest are liquids or even solids under ambient conditions. Liquids can be heated to evaporate them and create a supersonic jet. This technique worked well in the current work but it was not possible to create clusters of all investigated molecules. Targets which are present in a solid state need to be heated much more and require an oven to create a gas beam. This technique however is unable to provide the high momentum resolution which could be obtained with the supersonic jet in this work. Overall, target preparation is an immense experimental challenge and will require the exploration of alternative experimental techniques in the future. Techniques like laser-induced acoustic-desorption [44] have recently shown to be able to bring complex molecules to the gas phase as a target for dissociative electron attachment [6]. This technique currently has the drawback that the achievable target density is too low for momentum imaging experiments but it is a promising technique for future developments in experimental investigations of DEA. Alternative routes for target preparation are currently explored as well, e.g. studying a solid target on a surface [116]. Additionally, to understand the effect of dissociative electron attachment on living beings, biologically relevant molecules should be investigated in the liquid environment in which they are present in an organism. Recreating this environment in a well controlled way in an experiment is another challenge. With a wider variety of target molecules in the focus of DEA, the traditional gas beam will eventually have to be replaced by specialized target delivery systems in these experiments, depending on the investigated molecule. On the other hand, theoretical descriptions of DEA in complex molecules and clusters are extremely challenging. Understanding the experimental observations on a fundamental level however requires theoretical calculations which can accurately describe and predict physical processes. Therefore, studies of dissociative electron attachment in small molecules - which represent a limited part of the complex biological molecules - will stay important in the future as experimental data is required to encourage theoretical calculations.

8. List of publications

Journal articles

M. Weyland, X. Ren, T. Pflüger, W. Y. Baek, K. Bartschat, O. Zatsarinny, D. V. Fursa, I. Bray, H. Rabus, and A. Dorn. Novel method for state selective determination of electron-impact-excitation cross sections from 0° to 180°. *EPJ Techniques and Instrumentation*, 1(1):6, 2014.

T. N. Rescigno, C. S. Trevisan, A. E. Orel, D. S. Slaughter, H. Adaniya, A. Belkacem, M. Weyland, A. Dorn, and C. W. McCurdy. Dynamics of dissociative electron attachment to ammonia. *Physical Review A*, 93(5):052704, 2016.

X. Ren, S. Amami, O. Zatsarinny, T. Pflüger, M. Weyland, A. Dorn, D. Madison, K. Bartschat. Kinematically complete study of low-energy electron-impact ionization of argon: Internormalized cross sections in three-dimensional kinematics. *Physical Review A*, 93(6):062704, 2016.

X. Ren, S. Amami, O. Zatsarinny, T. Pflüger, M. Weyland, W. Y. Baek, H. Rabus, K. Bartschat, D. Madison, A. Dorn. Kinematically complete study of low-energy electron-impact ionization of neon: Internormalized cross sections in three-dimensional kinematics. *Physical Review A*, 91(3):032707, 2015.

X. Ren, T. Pflüger, M. Weyland, W. Y. Baek, H. Rabus, J. Ullrich, A. Dorn. High-resolution (e, 2e + ion) study of electron-impact ionization and fragmentation of methane. *The Journal of Chemical Physics*, 142(17):174313, 2015.

X. Ren, T. Pflüger, M. Weyland, W. Y. Baek, H. Rabus, J. Ullrich, A. Dorn. An (e, 2e + ion) study of low-energy electron-impact ionization and fragmentation of tetrahydrofuran with high mass and energy resolutions. *The Journal of Chemical Physics*, 141(13):134314, 2014.

Conference posters

M. Weyland, X. Ren, T. Pflüger, A. Dorn, W. Y. Baek, H. Rabus. Momentum imaging of dissociative electron attachment in biologically relevant molecules. *XXIX International Conference on Photonic, Electronic and Atomic Collisions*, Toledo, July 22-28 2015.

M. Weyland, X. Ren, T. Pflüger, A. Dorn, W. Y. Baek, H. Rabus. Momentum imaging of dissociative electron attachment in biologically relevant molecules. *XIX International Symposium on Electron-Molecule Collisions and Swarms*, Lisbon, July 17-20 2015.

M. Weyland, A. Dorn, H. Rabus, X. Ren, T. Pflüger, W. Y. Baek. Dissociative electron attachment in biologically relevant molecules. *DPG Spring Meeting*, Heidelberg, March 23-27 2015.

M. Weyland, T. Pflüger, X. Ren, W. Y. Baek, H. Rabus, A. Dorn. Differential cross section measurements for metastable state excitation by low energy electron impact at all scattering angles. *International Conference on Many Particle Spectroscopy of Atoms, Molecules, Clusters and Surfaces*, Metz, July 16-18 2014.

M. Weyland, A. Dorn, H. Rabus, X. Ren, T. Pflüger, W. Y. Baek. New method of measuring metastable states for electron impact on light targets at all scattering angles. *78th Annual Meeting of the DPG and DPG Spring Meeting*, Berlin, March 17-21 2014.

Bibliography

[1] H. Adaniya, B. Rudek, T. Osipov, D. J. Haxton, T. Weber, T. N. Rescigno, C. W. McCurdy, and A. Belkacem. Imaging the Molecular Dynamics of Dissociative Electron Attachment to Water. *Physical Review Letters*, 103(23):233201, 2009.

[2] H. Adaniya, D. S. Slaughter, T. Osipov, T. Weber, and A. Belkacem. A momentum imaging microscope for dissociative electron attachment. *Review of Scientific Instruments*, 83(2):023106, 2012.

[3] M. Allan, K. Franz, H. Hotop, O. Zatsarinny, and K. Bartschat. Absolute angle-differential cross sections for electron-impact excitation of neon within the first 3.5 eV above threshold. *Journal of Physics B: Atomic, Molecular and Optical Physics*, 42(4):044009, 2009.

[4] P. W. Atkins. *Molecular Quantum Mechanics*. Oxford University Press, Oxford / New York, 2nd edition, 1983.

[5] R. Azria, Y. Le Coat, G. Lefevre, and D. Simon. Dissociative electron attachment on H_2S: energy and angular distributions of H^- ions. *Journal of Physics B: Atomic and Molecular Physics*, 12(4):679–687, 1979.

[6] I. Bald, I. Dabkowska, and E. Illenberger. Probing biomolecules by laser-induced acoustic desorption: electrons at near zero electron volts trigger sugar-phosphate cleavage. *Angewandte Chemie International Edition*, 47(44):8518–20, jan 2008.

[7] C. Barckholtz, T. A. Barckholtz, and C. M. Hadad. C-H and N-H bond dissociation energies of small aromatic hydrocarbons. *Journal of the American Chemical Society*, 121(3):491–500, 1999.

[8] K. Bartschat. Electron-impact excitation of helium from the 1^1S and 2^3S states. *Journal of Physics B: Atomic, Molecular and Optical Physics*, 31:L469–L476, 1998.

[9] K. Bartschat, O. Zatsarinny, I. Bray, D. V. Fursa, and A. T. Stelbovics. On the convergence of close-coupling results for low-energy electron scattering from magnesium. *Journal of Physics B: Atomic, Molecular and Optical Physics*, 37(13):2617–2639, 2004.

[10] D. S. Belic, M. Landau, and R. I. Hall. Energy and angular dependence of H^- (D^-) ions produced by dissociative electron attachment to H_2O (D_2O). *Journal of Physics B: Atomic, Molecular and Optical Physics*, 14:175–190, 1981.

[11] N. Bhargava Ram and E. Krishnakumar. Dissociative electron attachment resonances in ammonia: a velocity slice imaging based study. *The Journal of Chemical Physics*, 136(16):164308, 2012.

[12] S. J. Blanksby and G. B. Ellison. Bond dissociation energies of organic molecules. *Accounts of Chemical Research*, 36(4):255–263, 2003.

[13] B. Boudaïffa, P. Cloutier, D. Hunting, M. A. Huels, and L. Sanche. Resonant Formation of DNA Strand Breaks by Low-Energy (3 to 20 eV) Electrons. *Science*, 287(5458):1658–1660, 2000.

[14] S. E. Bradforth, E. H. Kim, D. W. Arnold, and D. M. Neumark. Photoelectron spectroscopy of CN^-, NCO^-, and NCS^-. *The Journal of Chemical Physics*, 98(2):800–810, 1993.

[15] L. M. Branscomb, D. S. Burch, S. J. Smith, and S. Geltman. Photodetachment Cross Section and the Electron Effinity of Atomic Oxygen. *Physical Review*, 111:504–513, 1958.

[16] I. Bray, D. V. Fursa, and I. E. McCarthy. Convergent close-coupling method for electron scattering on helium. *Journal of Physics B: Atomic, Molecular and Optical Physics*, 27(14):L421 – L425, 1994.

[17] J. N. Brunt, F. H. Read, and G. King. The realization of high energy resolution using the hemispherical electrostatic energy selector in electron impact spectrometry. *Journal of Physics E: Scientific instruments*, 10:134–9, 1977.

[18] J. N. H. Brunt, G. C. King, and F. H. Read. A study of resonance structure in neon, argon, krypton and xenon using metastable excitation by electron impact with high energy resolution. *Journal of Physics B: Atomic, Molecular and Optical Physics*, 9(13):2195–2207, 1976.

[19] J. N. H. Brunt, G. C. King, and F. H. Read. A study of resonance structure in helium using metastable excitation by electron impact with high energy resolution. *Journal of Physics B: Atomic, Molecular and Optical Physics*, 10(3):433–448, 1977.

[20] J. M. Calo. Dimer formation in supersonic water vapor molecular beams. *The Journal of Chemical Physics*, 62(12):4904–4910, 1975.

[21] R. J. Celotta, R. A. Bennett, and J. L. Hall. Laser photodetachment determination of the electron affinities of OH, NH_2, NH, SO_2, and S_2. *The Journal of Chemical Physics*, 60(5):1740–1745, 1974.

[22] P. J. Chantry and G. J. Schulz. Kinetic-Energy Distribution of Negative Ions Formed by Dissociative Attachment and the Measurement of the Electron Affinity of Oxygen. *Physical Review*, 156(1):134–141, 1967.

[23] F. T. Chau and C. A. McDowell. Photoelectron Spectra of 1,2-Dibromo-1,1-difluoroethane, 1,2-Bromochloroethane, and 1,2-Dichloro-, 1,2-Dibromo-, and 1,2-Diiodotetrafluoroethane. *The Journal of Physical Chemistry*, 80(26):2923–2928, 1976.

[24] L. G. Christophorou. Dissociative Electron Attachment to Molecules. *The Journal of Chemical Physics*, 48(5):1956, 1968.

[25] L.G. Christophorou, editor. *Electron-Molecule Interactions and their Application*, volume 1. Academic Press Inc., London, 1984.

[26] A. Chutjian. Experimental SF_6^-/SF_6 and $Cl^-/CFCl_3$ Electron-Attachment Cross Sections in the Energy Range 0-200 meV. *Physical Review Letters*, 46(23):1511–1514, 1981.

[27] R. N. Compton and L. G. Christophorou. Negative-Ion Formation in H_2O and D_2O. *Physical Review*, 154(1):110–116, 1967.

[28] D. Cubric, D. J. L. Mercer, J. M. Channing, G. C. King, and F. H. Read. A study of inelastic electron scattering in He covering the complete angular range from 0° to 180°. *Journal of Physics B: Atomic, Molecular and Optical Physics*, 32:L45–L50, 1999.

[29] M. G. Curtis and I. C. Walker. Dissociative electron attachment in water and methanol (5-14 eV). *Journal of the Chemical Society, Faraday Transactions*, 88(19):2805, 1992.

[30] B. deB. Darwent. Bond Dissociation Energies in Simple Molecules. *National Standard Reference Data Series National Bureau of Standards (U.S.)*, 31:1–58, 1970.

[31] V. Devanathan. *Angular Momentum Techniques in Quantum Mechanics*, volume 108 of *Fundamental Theories of Physics*. Kluwer Academic Publishers, New York / Boston / Dordrecht / London / Moscow, 2002.

[32] J. G. Dillard. Negative ion mass spectrometry. *Chemical Reviews*, 73(6):589–643, 1973.

[33] S. F. dos Santos, N. Douguet, A. Orel, and T. Rescigno. Dynamics of Dissociative Electron Attachment to Uracil and Furane. In *47th Annual Meeting of the APS Division of Atomic, Molecular and Optical Physics*, Providence, Rhode Island, 2016.

[34] D. H. Dunn. Anisotropies in angular distributions of molecular dissociation products. *Physical Review Letters*, 8(2):62–64, 1962.

[35] I. I. Fabrikant, H. Hotop, and M. Allan. Elastic scattering, vibrational excitation, and attachment in low-energy electron-SF_6 scattering: Experiment and effective range theory. *Physical Review A*, 71:022712, 2005.

[36] R. L. Failes, J. T. Joyce, and E. C. Watton. Experimental Determination of Electron Affinities. *Journal of the Chemical Society, Faraday Transactions 1*, 69:1487–1490, 1973.

[37] R. L. Failes, J. T. Joyce, and E. C. Watton. The behaviour of some dimethyl- and trimethyl-substituted pyridines in the magnetron. *J. Phys. D: Appl. Phys.*, 9:1543–1546, 1976.

[38] J. Fedor, P. Cicman, B. Coupier, S. Feil, M. Winkler, K. Gluch, J. Husarik, D. Jaksch, B. Farizon, N. J. Mason, P. Scheier, and T. D. Märk. Fragmentation of transient water anions following low-energy electron capture by H_2O/D_2O. *Journal of Physics B: Atomic, Molecular and Optical Physics*, 39:3935–3944, 2006.

[39] M. W. Feyereisen, D. Feller, and D. A. Dixon. Hydrogen Bond Energy of the Water Dimer. *The Journal of Physical Chemistry*, 100:2993–2997, 1996.

[40] J. Franck and G. Hertz. Über Zusammenstöße zwischen Elektronen und Molekülen des Quecksilberdampfes und die Ionisierungsenergie desselben. *Verhandlungen der Deutschen Physikalischen Gesellschaft*, 16:457–467, 1914.

[41] D. Fursa and I. Bray. Calculation of electron-helium scattering. *Physical Review A*, 52(2):1279–1297, 1995.

[42] D. J. Goebbert, D. Khuseynov, and A. Sanov. Laboratory observation of the valence anion of cyanoacetylene, a possible precursor for negative ions in space. *Journal of Chemical Physics*, 131(16):161102, 2009.

[43] D. J. Goebbert, D. Khuseynov, and A. Sanov. Photoelectron imaging of cyanovinylidene and cyanoacetylene anions. *Journal of Physical Chemistry A*, 114(6):2259–2265, 2010.

[44] V. V. Golovlev, S. L. Allman, W. R. Garrett, N. I. Taranenko, and C. H. Chen. Laser-induced acoustic desorption. *International Journal of Mass Spectrometry and Ion Processes*, 169/170:69–78, 1997.

[45] J. D. Gorfinkiel, L. A. Morgan, and J. Tennyson. Electron impact dissociative excitation of water within the adiabatic nuclei approximation. *Journal of Physics B: Atomic, Molecular and Optical Physics*, 35(3):543–555, 2002.

[46] J. H. S. Green. Thermodynamic properties of organic oxygen compounds. *Quarterly Reviews, Chemical Society*, 15(2):125–152, 1961.

[47] H. Haberland, U. Buck, and M. Tolle. Velocity distribution of supersonic nozzle beams. *Review of Scientific Instruments*, 56(9):1712, 1985.

[48] O. F. Hagena and W. Obert. Cluster Formation in Expanding Supersonic Jets: Effect of Pressure, Temperature, Nozzle Size, and Test Gas. *The Journal of Chemical Physics*, 56(5):1793–1802, 1972.

[49] R. I. Hall, G. Joyez, J. Mazeau, J. Reinhart, and C. Schermann. Electron impact differential and integral cross sections for excitation of the n=2 states of helium at 29.2 eV, 39.2 eV and 48.2 eV. *Journal de Physique*, 34:827–843, 1973.

[50] N. C. Handy, S. Carter, and S. M. Colwell. The vibrational energy levels of ammonia. *Molecular Physics*, 96(4):477–491, 1999.

[51] E. E. Hanson. A Study of Kinetic energies of Atomic Ions Formed by Electron Impact in Nitric Oxide and Hydrogen Chloride. *Physical Review*, 51(2):86–94, 1937.

[52] D. J. Haxton, H. Adaniya, D. S. Slaughter, B. Rudek, T. Osipov, T. Weber, T. N. Rescigno, C. W. McCurdy, and A. Belkacem. Observation of the dynamics leading to a conical intersection in dissociative electron attachment to water. *Physical Review A*, 84(3):030701, 2011.

[53] D. J. Haxton, C. W. McCurdy, and T. N. Rescigno. Angular dependence of dissociative electron attachment to polyatomic molecules: Application to the $^2B_1$ metastable state of the H_2O and H_2S anions. *Physical Review A*, 73(6):062724, 2006.

[54] D. J. Haxton, C. W. McCurdy, and T. N. Rescigno. Dissociative electron attachment to the H_2O molecule I. Complex-valued potential-energy surfaces for the $^2B_1$, $^2A_1$, and $^2B_2$ metastable states of the water anion. *Physical Review A*, 75(1):012710, 2007.

[55] D. J. Haxton, T. N. Rescigno, and C. W. McCurdy. Dissociative electron attachment to the H_2O molecule. II. Nuclear dynamics on coupled electronic surfaces within the local complex potential model. *Physical Review A*, 75(1):012711, 2007.

[56] D. J. Haxton, T. N. Rescigno, and C. W. McCurdy. Three-body breakup in dissociative electron attachment to the water molecule. *Physical Review A*, 78(4):1–4, 2008.

[57] A. Herrera-Gómez, G. Vergara, and W. E. Spicer. Physics of high-intensity nanosecond electron source: Charge limit phenomenon in GaAs photocathodes. *Journal of Applied Physics*, 79(9):7318, 1996.

[58] E. Illenberger and H. Baumgärtel. Electron-attachment spectroscopy: formation and dissociation of negative ions in the fluorochloroethylenes. *Journal of Electron Spectroscopy and Related Phenomena*, 33:123–139, 1984.

[59] Z. J. Jabbour and K. Becker. Analysis of optical emissions produced by dissociative electron impact on CCl_2F_2. *The Journal of Chemical Physics*, 90:4819–4825, 1989.

[60] R. Kalescky, E. Kraka, and D. Cremer. Accurate determination of the binding energy of the formic acid dimer: The importance of geometry relaxation. *Journal of Chemical Physics*, 140:084315, 2014.

[61] C. Killer. Abel inversion algorithm (`http://de.mathworks.com/matlabcentral/fileexchange/43639-abel-inversion-algorithm`). MATLAB Central File Exchange. Published September 26, 2013. Retrieved January 17, 2014.

[62] C. E. Klots and R. N. Compton. Electron attachment to van der Waals polymers of water. *The Journal of Chemical Physics*, 69(4):1644, 1978.

[63] P. H. Krupenie. Spectrum of molecular oxygen. *Journal of Physical and Chemical Reference Data*, 1(2):423–534, 1972.

[64] M. V. Kurepa and D. S. Belić. Electron-chlorine molecule total ionisation and electron attachment cross sections. *J. Phys. B: At. Mol. Phys.*, 11(21):3719–3729, 1978.

[65] M. Lange, J. Matsumoto, J. Lower, S. Buckman, O. Zatsarinny, K. Bartschat, I. Bray, and D. Fursa. Benchmark experiment and theory for near-threshold excitation of helium by electron impact. *Journal of Physics B: Atomic, Molecular and Optical Physics*, 39(20):4179–4190, 2006.

[66] J. Langer, M. Stano, S. Gohlke, A. Rosa, W. Barszczewska, S. Matejcik, and E. Illenberger. Low energy (0–15 eV) electron stimulated reactions in single 1,2-$C_2F_4Cl_2$ molecules and clusters. *International Journal of Mass Spectrometry*, 223-224:193–204, 2003.

[67] J. E. Lennard-Jones. The electronic structure of some diatomic molecules. *Transactions of the Faraday Society*, 25:668–686, 1929.

[68] W. W. Lozier. Negative Ions in Hydrogen and Water Vapor. *Physical Review*, 36(8):1417–1418, 1930.

[69] D. M. Lubman, C. T. Rettner, and R. N. Zare. How isolated are molecules in a molecular beam? *The Journal of Physical Chemistry*, 86(7):1129–1135, 1982.

[70] J. C. Mackie, M. B. Colket III, and P. F. Nelson. Shock tube pyrolysis of pyridine. *The Journal of Physical Chemistry*, 94(10):4099–4106, 1990.

[71] H. Maier-Leibnitz. Ausbeutemessungen beim Stoß langsamer Elektronen mit Edelgasatomen. *Zeitschrift für Physik*, 95(7-8):499–523, 1935.

[72] I. Martin, T. Skalicky, J. Langer, H. Abdoul-Carime, G. Karwasz, E. Illenberger, Mi. Stano, and S. Matejcik. Low energy electron driven reactions in single formic acid molecules (HCOOH) and their homogeneous clusters. *Physical Chemistry Chemical Physics*, 7(10):2212–2216, 2005.

[73] Harrie Massey. *Negative ions*. Cambrigde University Press, Cambridge, 3rd edition, 1976.

[74] D. F. McMillen and D. M. Golden. Hydrocarbon Bond Dissociation Energies. *Annual Review of Physical Chemistry*, 33:493–532, 1982.

[75] C. E. Melton. Cross Sections and Interpretation od Dissociative Attachment Reactions Producing OH^-, O^- and H^- in H_2O. *The Journal of Chemical Physics*, 57(10):4218 – 4225, 1972.

[76] D.R. Miller. Free Jet Sources. In G. Scoles, editor, *Atomic and Molecular Beam Methods*, volume 1. Oxford University Press, New York / Oxford, 1988.

[77] A. Modelli and P. D. Burrow. Electron-transmission study of the temporary anion states of substituted pyridines. *Journal of Electron Spectroscopy and Related Phenomena*, 32(3):263–276, 1983.

[78] H. W. Moos and J. R. Woodworth. Observation of the Forbidden $2\,^3S_1 \rightarrow 1\,^1S_0$ Spontaneous Emission Line from Helium and Measurement of the Transition Rate. *Physical Review Letters*, 30(17):775 – 778, 1973.

[79] A. Moradmand, J. B. Williams, A. L. Landers, and M. Fogle. Momentum-imaging apparatus for the study of dissociative electron attachment dynamics. *Review of Scientific Instruments*, 84(3):033104, 2013.

[80] D. Nandi, V. S. Prabhudesai, and E. Krishnakumar. Velocity map imaging for low-energy electron-molecule collisions. *Radiation Physics and Chemistry*, 75(12):2151–2158, 2006.

[81] D. Nandi, V. S. Prabhudesai, E. Krishnakumar, and A. Chatterjee. Velocity slice imaging for dissociative electron attachment. *Review of Scientific Instruments*, 76(2005), 2005.

[82] I. Nenner and G. J. Schulz. Temporary negative ions and electron affinities of benzene and N-heterocyclic molecules: pyridine, pyridazine, pyrimidine, pyrazine, and s-triazine. *The Journal of Chemical Physics*, 62(5):1747, 1975.

[83] J. M. Oakes and G. B. Ellison. Photoelectron Spectroscopy of the Allenyl Ion CH_2=C=CH^-. *Journal of the American Chemical Society*, 105:2969–2975, 1983.

[84] J. M. Oakes, M. E. Jones, V. M. Bierbaum, and G. B. Ellison. Photoelectron Spectroscopy of CCO^- and $HCCO^-$. *Journal of Physical Chemistry*, 87:4810–4815, 1983.

[85] L. Olejko, P. J. Cywinski, and I. Bald. Ion-selective formation of a guanine quadruplex on DNA origami structures. *Angewandte Chemie - International Edition*, 54(2):673–677, 2015.

[86] T. F. O'Malley. Theory of Dissociative Attachment. *Physical Review*, 150(1):14–29, 1966.

[87] T. F. O'Malley and H. S. Taylor. Angular Dependence of Scattering Products in Electron-Molecule Resonant Excitation and in Dissociative Attachment. *Phys. Rev.*, 176(1):207–221, 1968.

[88] D. A. Orlov, M. Hoppe, U. Weigel, D. Schwalm, A. S. Terekhov, and A. Wolf. Energy distributions of electrons emitted from GaAs(Cs, O). *Applied Physics Letters*, 78(18):2721, 2001.

[89] D. A. Orlov, U. Weigel, D. Schwalm, A. S. Terekhov, and A. Wolf. Ultracold electron source with a GaAs-photocathode. *Nuclear Instruments and Methods in Physics Research Section A: Accelerators, Spectrometers, Detectors and Associated Equipment*, 532(1-2):418–421, 2004.

[90] S. Pastuszka, M. Hoppe, D. Kratzmann, D. Schwalm, A. Wolf, A. S. Jaroshevich, S. N. Kosolobov, D. A. Orlov, and A. S. Terekhov. Preparation and performance of transmission-mode GaAs photocathodes as sources for cold dc electron beams. *Journal of Applied Physics*, 88(11):6788, 2000.

[91] S. Pastuszka, D. Kratzmann, D. Schwalm, A. Wolf, and A. S. Terekhov. Transverse energy spread of photoelectrons emitted from GaAs photocathodes with negative electron affinity. *Applied Physics Letters*, 71(20):2967, 1997.

[92] A. Pelc, W. Sailer, P. Scheier, N. J. Mason, and T. D. Märk. Low energy electron attachment to formic acid. *European Physics Journal D*, 20:441–444, 2002.

[93] A. Pelc, W. Sailer, P. Scheier, M. Probst, N. J. Mason, E. Illenberger, and T. D. Märk. Dissociative electron attachment to formic acid (HCOOH). *Chemical Physics Letters*, 361:277–284, 2002.

[94] F. Pichou, A. Huetz, G. Joyez, M. Landau, and J. Mazeau. Electron impact excitation of helium : absolute differential cross sections of the n=2 and 3^3S states from threshold to 3-6 eV above. *Journal of Physics B: Atomic, Molecular and Optical Physics*, 9(6):933–944, 1976.

[95] V. S. Prabhudesai, D. Nandi, A. H. Kelkar, R. Parajuli, and E. Krishnakumar. Dissociative electron attachment to formic acid. *Chemical Physics Letters*, 405(1-3):172–176, 2005.

[96] G. Pretzler. A New Method for Numerical Abel-Inversion. *Zeitschrift für Naturforschung*, 46a:639–641, 1991.

[97] Ozone Secretariat United Nations Environment Programme. *Handbook for the Montreal Protocol on Substances that Deplete the Ozone Layer*. Secretariat for The Vienna Convention for the Protection of the Ozone Layer & The Montreal Protocol on Substances that Deplete the Ozone Layer, Nairobi, 10th edition, 2016.

[98] D. Rapp and D. D. Briglia. Total Cross Sections for Ionization and Attachment in Gases by Electron Impact. II. Negative-Ion Formation. *The Journal of Chemical Physics*, 43(5):1480–1489, 1965.

[99] P. Rawat, V. S. Prabhudesai, G. Aravind, M. A. Rahman, and E. Krishnakumar. Absolute cross sections for dissociative electron attachment to H_2O and D_2O. *Journal of Physics B: Atomic, Molecular and Optical Physics*, 40(24):4625–4636, 2007.

[100] F. H. Read and J. M. Channing. Production and optical properties of an unscreened but localized magnetic field. *Review of Scientific Instruments*, 67(6):2372, 1996.

[101] T. N. Rescigno, C. S. Trevisan, A. E. Orel, D. S. Slaughter, H. Adaniya, A. Belkacem, M. Weyland, A. Dorn, and C. W. McCurdy. Dynamics of dissociative electron attachment to ammonia. *Physical Review A*, 93(5):052704, 2016.

[102] S. Richard, F. Aniel, and G. Fishman. Energy-band structure of Ge, Si, and GaAs: A thirty-band k·p method. *Physical Review B*, 70:235204, 2004.

[103] Benedikt Rudek. Dissociative Electron Attachment to Water. diplomathesis, Institut für Kerphysik, Goethe Universität, Frankfurt am Main, 2009.

[104] G. Sanna and G. Tomassetti. *Introduction to Molecular Beams Gas Dynamics*. Imperial College Press, London, 2005.

[105] J. E. Sansonetti and W. C. Martin. Handbook of basic atomic spectroscopic data. `http://physics.nist.gov/PhysRefData/Handbook/Tables/heliumtable5.htm`, 2005.

[106] C. D. Schröter, A. Rudenko, A. Dorn, R. Moshammer, and J. Ullrich. Status of the pulsed photoelectron source for atomic and molecular collision experiments. *Nuclear Instruments and Methods in Physics Research Section A: Accelerators, Spectrometers, Detectors and Associated Equipment*, 536(3):312–318, 2005.

[107] G. J. Schulz and R. E. Fox. Excitation of Metastable Levels in Helium near Threshold. *Phys. Rev.*, 106:1179–1181, 1957.

[108] K. Sendt, G. B. Bacskay, and J. C. Mackie. Pyrolysis of Furan : Ab Initio Quantum Chemical and Kinetic Modeling Studies. *Journal of Physical Chemistry A*, 104:1861–1875, 2000.

[109] H. Shelton. Thermionic emission from a planar tantalum crystal. *Physical Review*, 107(6):1553–1557, 1957.

[110] O. B. Shpenik, A. N. Zavilopulo, A. V. Snegursky, and I. I. Fabrikant. Excitation of metastable levels of noble-gas atoms in crossed electron and gas dynamical atomic beams. *Journal of Physics B: Atomic, Molecular and Optical Physics*, 17:887–904, 1984.

[111] A. Sieradzka. Private communication, to be published in PhD thesis. May 5, 2016.

[112] A. Sieradzka, F. Blanco, M. C. Fuss, Z. Mašín, J. D. Gorfinkiel, and G. García. Electron scattering from pyridine. *The Journal of Physical Chemistry A*, 118(33):6657–63, 2014.

[113] H. D. Smyth. Products and Processes of Ionization be Low Speed Electrons. *Review of Modern Physics*, 3(3):347–392, 1931.

[114] S. K. Srivastava and O. J. Orient. Polar dissociation as a source of negative ions. *AIP Conference Proceedings*, 111:56–66, 1984.

[115] P. Sulzer, S. Ptasinska, F. Zappa, B. Mielewska, A. R. Milosavljevic, P. Scheier, T. D. Märk, I. Bald, S. Gohlke, M. A. Huels, and E. Illenberger. Dissociative electron attachment to furan, tetrahydrofuran, and fructose. *The Journal of Chemical Physics*, 125(4):44304, 2006.

[116] Ewelina Szymańska - Skolimowska. *Dissociative electron attachment and dipolar dissociation processes in organic molecules found in the interstellar medium*. PhD thesis, The Open University, 2014.

[117] J. T. Tate and P. T. Smith. The efficiencies of ionization and ionization potentials of various gases under electron impact. *Physical Review*, 39(2):270–277, 1932.

[118] J. T. Tate, P. T. Smith, and A. L. Vaughan. A Mass Spectrum Analysis of the Products of Ionization by Electron Impact in Nitrogen, Acetylene, Nitric Oxide, Cyanogen and Carbon Monoxide. *Physical Review*, 48(6):525–531, 1935.

[119] J. Tennyson. Electron-molecule collision calculations using the R-matrix method. *Physics Reports*, 491(2-3):29–76, 2010.

[120] J. P. Toennies and K. Winkelmann. Theoretical studies of highly expanded free jets: Influence of quantum effects and a realistic intermolecular potential. *The Journal of Chemical Physics*, 66(9):3965, 1977.

[121] M. Tronc, R. Azria, and M. B. Arfa. Differential cross section for H^- and NH_2^- ions in NH_3. *Journal of Physics B: Atomic, Molecular and Optical Physics*, 21:2497–2506, 1988.

[122] J. Ullrich, R. Moshammer, A. Dorn, R. Dörner, L. Ph. H. Schmidt, and H. Schmidt-Böcking. Recoil-ion and electron momentum spectroscopy: reaction-microscopes. *Reports on Progress in Physics*, 66(9):1463–1545, 2003.

[123] R. J. Van Brunt and L. J. Kieffer. Angular Distribution of O^- from Dissociative Electron Attachment to O_2. *Physical Review A*, 2(5):1899–1905, 1970.

[124] R. S. Van Dyck Jr., C. E. Johnson, and H. A. Shugart. Radiative Lifetime of the Metastable $2\,^1S_0$ State of Helium. *Physical Review Letters*, 25(20):1403–1405, 1970.

[125] G. Vergara, J. Capmany, and M. T. Montojo. Influence of the dopant concentration on the photoemission in NEA GaAs photocathodes. *Vacuum*, 48(2):155–160, 1997.

[126] K. M. Vogelhuber, S. W. Wren, L. Sheps, and W. C. Lineberger. The C-H bond dissociation energy of furan: Photoelectron spectroscopy of the furanide anion. *Journal of Chemical Physics*, 134(6):064302, 2011.

[127] M. Weyland, X. Ren, T. Pflüger, W. Baek, K. Bartschat, O. Zatsarinny, D. V. Fursa, I. Bray, H. Rabus, and A. Dorn. Novel method for state selective determination of electron-impact-excitation cross sections from 0° to 180°. *EPJ Techniques and Instrumentation*, 1(1):6, 2014.

[128] E. Wigner. *Gruppentheorie und ihre Anwendung auf die Quantenmechanik der Atomspektren*. Springer Fachmedien GmbH, Wiesbaden, 1977.

[129] W. C. Wiley and I. H. McLaren. Time-of-Flight Mass Spectrometer with Improved Resolution. *Review of Scientific Instruments*, 26(12):1150, 1955.

[130] B. Wu, L. Xia, H. K. Li, X. J. Zeng, and S. Xi Tian. Positive/negative ion velocity mapping apparatus for electron-molecule reactions. *Review of Scientific Instruments*, 83, 2012.

[131] O. Zatsarinny. BSR: B-spline atomic R-matrix codes. *Computer Physics Communications*, 174(4):273–356, 2006.

[132] C. G. Zhan, J. A. Nichols, and D. A. Dixon. Ionization potential, electron affinity, electronegativity, hardness, and electron excitation energy: Molecular properties from density functional theory orbital energies. *Journal of Physical Chemistry A*, 107(20):4184–4195, 2003.

[133] J. Zhou, E. Garand, and D. M. Neumark. Slow electron velocity-map imaging spectroscopy of the C_4H^- and C_4D^- anions. *Journal of Chemical Physics*, 127:154320, 2007.

Danksagung

An dieser Stelle möchte ich mich bei all denjenigen bedanken, ohne die diese Arbeit nicht möglich gewesen wäre. Mein Dank geht an meinen Betreuer Alexander Dorn, für die vielen lehrreichen Gespräche genauso wie für die tatkräftige Unterstützung im Labor. Außerdem hat die gesamte Gruppe zu einem sehr angenehmen Arbeitsklima beigetragen. Vielen Dank für die schöne Zeit!

I also want to thank Nigel Mason for giving me the opportunity to perform my experiments at the Open University and for always making me feel welcome there.

A very special thanks goes out to my lovely Aguś! Thank you for all your support, for listening to me talking about my boring experimental problems and for making the time since I know you an unforgettable adventure. Dziękuję za wszystko!

Ein großer Dank geht an meine ganze Familie und ganz besonders an meine Mama! Vielen Dank für deine Unterstützung und deinen Rat in allen Lebenslagen, und natürlich für die vielen Care-Pakete mit Leckereien! :-)